Combining rotating-coil measurements of large-aperture accelerator magnets

Kombination von Magnetfeldmessungen mit der Rotierenden Spule
Zur Erlangung des akademischen Grades Doktor-Ingenieur (Dr.-Ing.)
genehmigte Dissertation von Oliver Köster, Dipl.-Ing. aus Berlin
Tag der Einreichung: 05.07.2016, Tag der Prüfung: 23.09.2016
Darmstadt (2016) — D 17

1. Gutachten: Prof. Dr.-Ing. Oliver Boine-Frankenheim
2. Gutachten: Dr.-Ing. habil. Stephan Russenschuck

TECHNISCHE
UNIVERSITÄT
DARMSTADT

Fachbereich Elektrotechnik
und Informationstechnik
Institut für Theorie
Elektromagnetischer Felder

Combining rotating-coil measurements of large-aperture accelerator magnets
Kombination von Magnetfeldmessungen mit der Rotierenden Spule

Genehmigte Dissertation von Oliver Köster, Dipl.-Ing. aus Berlin

1. Gutachten: Prof. Dr.-Ing. Oliver Boine-Frankenheim
2. Gutachten: Dr.-Ing. habil. Stephan Russenschuck

Tag der Einreichung: 05.07.2016
Tag der Prüfung: 23.09.2016

Darmstadt (2016) — D 17

Kurzfassung

Die Rotierende Spule ist ein Werkzeug zum Messen von magnetischen Feldern von Beschleunigermagneten. Durch die Länge der Spule, die das gesamte longitudinale Feld erfasst, geben die Messdaten zweidimensionale, integrierte Größen an. Dies führt zu einer Darstellung des Feldes durch harmonische Funktionen in Zylinderkoordinaten oder einer analytischen Funktion in komplexen, kartesischen Koordinaten. Die Koeffizienten dieser Fourierreihe werden Multipole genannt und ergeben sich direkt aus der Messung mit der Rotierenden Spule.

Mechanische Ungenauigkeiten und Messfehler führen zu unterschiedlichen Störungen auf den Multipolen: Während das Hauptfeld den kompletten Abweichungen unterliegt, werden die höheren Multipole durch ein Differenzsignal berechnet und sind damit um ca. zwei Größenordnungen genauer bestimmbar. Diese Präzision bei der Bestimmung der Feldfehler macht die Rotierende Spule anderen Messmethoden überlegen und ein sehr weit verbreitetes Messwerkzeug für Beschleunigermagnete.

Durch die unveränderlichen Abmessungen ist eine Spule ausschließlich für Magnete mit passender Apertur einsetzbar, da die präzise Felddarstellung auf die radiale Abmessung der Spule begrenzt ist. Dies verhindert die sinnvolle Anwendung des Werkzeugs in Magneten mit Aperturen, die entweder deutlich größer sind als die Spulenabmessungen oder rechteckig mit stark unterschiedlichem Länge-Breite-Verhältnis.

Eine Kombination von mehreren Spulenmessungen ist Grundlage dieser Arbeit. Die Fehlerverteilung auf den Multipolen und deren Fortpflanzung ist dabei von besonderer Bedeutung. Insbesondere ist eine Kombination mittels des magnetischen Feldes naheliegend, aber von geringer Genauigkeit, da die Fehler des Hauptfeldes dominieren. Deswegen muss eine Kombination, die die hohe Präzision der Multipole erhalten soll, über die Verbindung dieser Multipole funktionieren. Eine solche Methode wird in dieser Arbeit vorgestellt und an verschiedenen Beispielen veranschaulicht. Dabei wird stark auf die Fehlerfortpflanzung eingegangen, die Messfehler, aber auch Positionierungsfehler

beinhaltet. Neben Simulationen werden die Ergebnisse einer Feldmessung im Labor gezeigt. Die dabei aufkommenden Schwierigkeiten werden beschrieben und Problemlösungen werden aufgezeigt.

Die vorgestellte Kombination hat die Möglichkeit, unpräzise gemessene Multipole auszuschließen. Damit werden Messfehler gefiltert und die höchste Genauigkeit der Einzelmessung übernommen. Zwingendermaßen unterliegt die Messmethode der Qualität der Einzelmessung. Das wird offensichtlich bei systematischen Fehlern, die bei der Spulenkalibration aufkommen können.

Abschließend wird ein Spulendesign präsentiert, das auf die Eigenschaften der Methode, aber auch auf die Sensitivität des Spulentyps angepasst ist. Simulationen und eine Fehleranalyse werden dargestellt mit anschließendem Ausblick auf die zu entwickelnde Messbank.

Abstract

The rotating coil is a widely used tool to measure the magnetic field and the field errors in accelerator magnets. The coil has a length that exceeds the entire magnetic field along the longitudinal dimension of the magnet and gives therefore a two-dimensional representation of the integrated field. Having a very good precision ($\approx 10^{-6}$ relative to the main field), the rotating coil lacks in versatility. The fixed dimensions make it impractical and inapplicable in situations, when the radial coil dimension is much smaller than the aperture or when the aperture is only little covered by the coil. That being the case for rectangular apertures with large aspect ratio, where a basic measurement by the rotating coil describes the field only in a small area of the magnet.

A combination of several measurements at different positions is the topic of this work. Very important for a combination is the error distribution on the measured field harmonics. To preserve the good precision of the higher-order harmonics, the combination must not rely on the main field component that is measured with less precision. Considering that, a method is derived that computes the field harmonics at the central position by measurement data at displaced positions.

The error propagation of the measurement error and the uncertainty of the position is studied for different cases. This is done for simulated fields but also for an actual measurement in the laboratory. It is shown that the precision of the computed field harmonics, in particular the higher-order ones, is improved with respect to a single measurement at one position.

Finally, a coil design is presented that is adapted to the method and the measurement errors. Acquiring the used field harmonics with the highest sensitivity, improves the results of the computations.

This work presents a method that improves the versatility of the rotating coil by combining measurements at several positions.

Contents

1 Introduction

In the research of fundamental physics, particle accelerators play an important role. They accelerate particles to a high energy and let them collide with each other or aim them towards other matter. Research experiments encourage an understanding of the standard model of particle physics, for example with the discovery [1, 2] of the Higgs boson [3] in 2012 at the Large Hadron Collider [4] at the European Organization for Nuclear Research (CERN). Particle accelerators have also been used in medical application for cancer therapy [5], where heavy ions are directed towards cancer cells of a patient. Other fields of application are seen in material science as well as in industrial processing [6].

Essential parts for accelerators are strong and accurate magnets [7]. Their main field of application is to direct particles to the design trajectory and to focus them to stay together as a compact beam [8, 9]. For the purpose of particle colliders especially [10], the magnetic field produced by the magnets must be very accurate and known with the utmost precision [11]. Therefore, an accurate and precise magnetic field measurement for each magnet is required before the installation to characterize the field errors. Magnetic field measurements are required to validate the magnet design, to guarantee the magnet-to-magnet reproducibility in series productions and to study hysteresis effects and eddy currents [12].

In the field of magnetic field measurements, there are different ways to obtain field information from different tools [13]. The most widely used Hall sensor [14] acquires the magnetic flux through a small surface. It is versatile and useful in many situations, but limited in precision cause of non-linearities and temperature-dependence [15]. This is the advantage of the rotating coil [16, 17]. Acquiring two-dimensional integrated fields, the rotating coil is a long wire loop that is rotated in a static magnetic field. In Faraday's law of induction [18], a voltage is measurable at the end of the wire, which can, with a correct calibration, be related to the magnetic field integrated along the longitudinal direction. Such a field measurement is strictly two-dimensional and is suitable to the *hard-edge model* [19], where the magnetic field is assumed to be constant over the magnetic length and zero otherwise. The rotating coil, highly adapted for accelerator magnets with cylindrical bore, measures most precisely, but also rapidly and with relatively low effort [20]. The acquired data is the magnetic flux along a circular trajectory, which can be related to a magnetic field component. When considering the Laplace equation, this component computes the multipole coefficients of a harmonic function that describes the field inside the covered domain. These multipole coefficients give a closed-form

formula for the magnetic field, which is useful for beam dynamic studies. The overall multipoles of all magnets in a circular accelerator hold information for the beam stability and dynamics [21].

The reason behind the high precision of the rotating coil is due to the compensation/*bucking* [22] of vibrations and noise. The errors coming from an imperfect mechanical movement of the shaft can be reduced by about two orders of magnitude [23]. For the analytic function, this high precision can be incorporated for the higher-order multipole coefficient, but not the main field component. Therefore the field representation is very precise on the field errors, but not on the harmonic coefficient that describes the main field.

The drawback of a rotating coil is its inflexibility, as it is constructed on a shaft with fixed dimensions. The building procedure and the calibration of the coils is expensive and also time consuming [24]. For this reason, a magnetic measurement laboratory usually has a set of rotating coils to work with, if there is not a large series of magnets to measure with a suitable device built for that series. In addition to the lack of versatility, the resulting field description is very error-prone outside the measurement domain, so that the coil with the largest diameter for the magnet aperture must be used. A workaround is needed for situations, when a suitable rotating coil is not available or the aperture is only slightly covered by the circular domain, where the field is measured. Especially rectangular apertures with large aspect ratios create situations, where a common measurement is not sufficient.

The difficulty to measure magnets with rectangular aperture has been known for decades, a first publication in 1987 [25] shows a purely mathematical approach. For the SIS 100 [26] main dipoles for the FAIR project at GSI (Gesellschaft für Schwerionenforschung), a practical solution is needed that considers measurement noise and uncertainties. The state of the art solution for that problem is the representation in elliptical coordinates [27] to express the field in the largest possible domain. The elliptical multipoles [28, 29] are defined by a Fourier transformation of the magnetic field on the elliptic boundary. Using the magnetic field from a rotating-coil measurement, introduces the high uncertainty of the main field component and leads to a low precision of the results.

This work presents a new method, which links field information from measurements at different positions. It is a technique to combine several measurements by considering the uncertainty of the data acquisition. In a certain configuration, it is a fitting of the field variation by sampling small parts of the domain of interest. The measurements from different positions can therefore be combined into one result, which produces precise coefficients for the entire domain

covered by measurements. It also increases the precision of the measurement by filtering noise. This is due to the possibility to work exclusively with precise field information. The combination of measurements holds a robust representation for the field against the errors in measurement and positioning. It therefore improves a measurement, but also increases the versatility of the rotating coil and with it, the ability of the entire magnetic measurement laboratory.

Motivation

A precise combination of rotating-coil measurements gives new possibilities to the magnetic measurement laboratory. A rotating-coil probe is no longer suitable only for magnets with specific dimensions, but can be used also for magnets with a larger aperture. As a result, a rotating coil is seen as more versatile and practical. On the other hand, this means that less coils have to be built and that a measurement laboratory can limit the number of available devices.

The inability to precisely measure magnets with rectangular apertures, has tasked the magnetic measurement community for decades. A combination of several measurements is therefore of high interest to various measurement laboratories, as long as the precision of the compensated measurement data is preserved. The difficulty of the irregular error distribution on the measured multipole coefficients, affects the results of former approaches. A detailed error analysis is therefore inevitable, when trying to combine multipole coefficients.

Overview

This work starts with the essentials in magnetic field measurements. It introduces the rotating coil, the principle of compensation and the sensitivity factors. Unavoidable measurement errors are detailed and the influence on the multipoles is discussed. The measured field harmonics are explained in complex notation, whereas mathematical concepts of the analytic function are detailed. In particular, the principle of analytic continuation for the field expression is derived.

After presenting similar solutions using other mathematical concepts, the method for combining rotating-coil measurements is explained. The link, the resulting matrix, is shown with its inner characteristics, which depend on different parameters. Furthermore is the error coming from inaccurate positioning analyzed and quantified.

This method is then applied to different configurations, where the error-propagation is analyzed based on simulated data. A dipole with rectangular aperture is studied as well as a quadrupole with quadratic aperture.

To comprehend the method in measurement practice, the results of an actual measurement are presented. The difficulties and setbacks that have occurred in the laboratory are shown.

Finally, a coil design is given, which has been adapted to the sensitivity of a single measurement and the error-propagation of the method. It is evaluated by a simulation of the former measurement.

The work concludes with a summary and an outlook how the adapted design can be used for a future measurement bench in the CERN laboratories or in every other magnetic measurement facility.

2 Magnetic field measurements

Magnetic field measurements are required in any accelerator project. To know the strength and the errors of the magnets is one of the most important aspects for the beam stability in an accelerator facility [30]. The magnetic field errors are usually expressed as integrated circular harmonics, which describe the field as a Fourier series in polar coordinates or as an analytic function in Cartesian coordinates. These harmonic coefficients come from a measurement at the boundary of a circular domain and uniquely determine the field representation.

A proven measurement method for accelerator magnets relies on the rotating coil [31], which is basically a number of wire loops mounted on a shaft that is rotated in the magnet bore. By rotation, the intercepted flux of the static field, changes in time and creates a voltage at the end of the wire. This voltage is acquired by a digital integrator [32], which allows to relate the signal back to the flux and the field. As the wire loop moves along a circular trajectory, the acquired field information link directly to the multipole coefficients of the analytic function.

All the field values are seen as integrated quantities along the longitudinal direction that goes through the magnet. That makes this field representation completely two-dimensional. Practically, the wire loop has a length that exceeds the magnetic length of the magnet, such that the complete field in longitudinal direction is included.

2.1 Magnets in accelerator physics

Magnets play a fundamental role in particle accelerators. Their main task is to deflect the particle beam to follow its defined trajectory and to focus the particles to stay together. For these tasks, dipole and quadrupole magnets are installed at many positions around the beam pipe where the particle beam travels through. The number and strength of the magnets depend on the type and goal of the accelerator facility. A linear accelerator usually needs less dipoles than a circular collider such as the LHC with 1232 bending dipoles [33]. Other fields of application are at the injection part and the corrector magnets including sextupoles, octupoles and decapoles.

The magnetic field $\vec{B}$ of the magnets acts according to the Lorentz force $\vec{F}_{\mathrm{L}}$ on moving particles with a charge q and a velocity $\vec{v}$:

$$\vec{F}_{\mathrm{L}} = q(\vec{v} \times \vec{B}) + q\vec{E} \ . \tag{1}$$

A particle traveling through a magnetic field is accelerated in the direction perpendicular to the field direction. Fig. (1) shows a dipole magnet with coils on top and bottom, which creates a vertical field in the center. A particle in the magnetic center is therefore deflected in the horizontal direction. This acceleration forces the particle into a curved parabolic trajectory following the designed track.

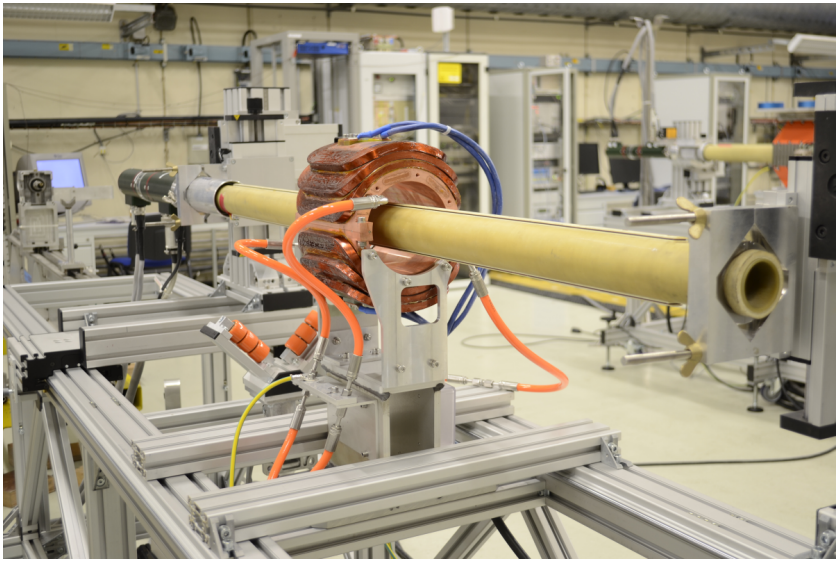

Figure 1: Rotating-coil system mounted on the bench to measure a dipole corrector magnet for the Elena project [34].

Apart from the dipoles and their constant field in first approximation, there are quadrupoles, sextupoles and other magnet types of higher orders. Quadrupoles have a field that grows linearly with distance to the center, while the polarity changes every 90°. The force on the traveling particles does the same: It points towards the center in one plane and away from it in the other plane. That causes the focusing and defocusing of the particle beam depending on its position.

To know the exact effect on the particles, the magnetic field has to be known to a high degree. Furthermore, the particle beam is not perfectly in the center so that the magnetic field has to be known in a large area inside the magnet. With a good knowledge of the field errors of the used magnets, the effects can

be corrected by corrector magnets. It is also possible to install the magnets in the right order [35] to cancel out perturbing effects on the particle beam.

The computations and simulations from the model give an estimate about the field, but magnetic measurements are in most cases inevitable. That is because of the uncertainties of the used materials, mechanical tolerances and the dynamic effects in the iron that are difficult to model.

2.2 Measurement techniques

In accelerator physics, the main aspect of magnetic field measurements is to characterize the magnetic field produced by the accelerator magnet. There are various tools to measure the magnetic field, which base on different physical laws. The rotating-coil probe and the single stretched wire [36] are based on Faraday's law of induction:

$$U_\mathrm{i} = -\frac{\mathrm{d}\Phi_\mathrm{m}}{\mathrm{d}t} = -\frac{\mathrm{d}}{\mathrm{d}t}\int_{\mathscr{A}} \vec{B}\cdot\mathrm{d}\vec{A}\,. \tag{2}$$

Caused by a change of the position of a wire loop, the intercepted magnetic field changes and induces a measurable voltage signal. Details of the rotating coil will be explained in Paragraph (2.4).

Other systems work under the Lorentz force on a current-carrying wire of the length ℓ:

$$\vec{F} = I\vec{\ell}\times\vec{B}\,. \tag{3}$$

The current I in a wire in combination with an external magnetic field $\vec{B}$ causes a force and an acceleration of the wire. This movement can be detected by an optical sensor and related to the external magnetic field [37]. In addition, there is the Hall sensor based on the Hall effect, the NMR probe and other very specific devices [38].

The different measurement devices acquire different field information: The Hall sensor, for example, acquires the flux through a small area, which is useful to create a field map, a three-dimensional grid of the field vectors. The rotating coil, however, measures the flux over an integrated area, which yields a purely two-dimensional field representation. In this work, the field information come from the rotating coil only, such that a detailed explanation is given for this device only.

The various tools acquire different field information and come with other uncertainties. There is no device that can measure the magnetic field perfectly.

There is always an uncertainty, there are necessarily error bars around the measured value. Even though, the quality of a measurement strongly depends on the performing laboratory, the compensated signal acquired by a rotating coil is usually the most precise information for the field errors. For this device, sources of errors and their characteristics are discussed in Paragraph (2.5.1). For the absolute value of a constant field, the NMR probe yields comparable precision [39].

2.3 Two-dimensional field errors

Real accelerator magnets are not ideal nor infinitely large. Their magnetic field is defined by the geometry of the coil windings and the iron. The field errors describe the derivation to the ideal field and are usually given in a two-dimensional analytic function. The longitudinal dependency along the reference path of the particles is thereby integrated, as shown in the following.

The characterization of the magnetic field of accelerator magnets depends on their use and their field of application. For large accelerators as the LHC, the deflection of the particles in the magnet is small: With 1232 bending magnets at a circumference of 27 km, the bending angle [40] in one single dipole is $2\pi/1232 \approx 0.005$ rad $\approx 0.29°$. Therefore, an approximation is common: The magnetic field over the longitudinal length is approximated by one value multiplied by the magnetic length [41, 42]. That means, that the field in longitudinal direction is assumed to be constant within the magnetic length and zero otherwise:

$$\int_{-\infty}^{\infty} B \, \mathrm{d}s \approx B\ell_{\mathrm{m}} \, . \tag{4}$$

s is the longitudinal coordinate that follows the ideal particle through the magnet [43]. The magnetic length ℓ_{m} holds the length, where the magnetic field has its constant value. Around that the field is assumed to be zero. This approximation is called *hard-edge model* and the longitudinal field profile is shown in Fig. (2). The blue shape shows the longitudinal profile of the y-component of the magnetic field, whereas the green line is an approximation with the hard-edge model.

The approximation is common for magnets, where the deflection of the particle is small. This is usually the case for large colliders and storage rings with particles of high energy. Furthermore does simulation software for beam simulations, as *sixtrack* [44] and *mad* [45], use these approximation.

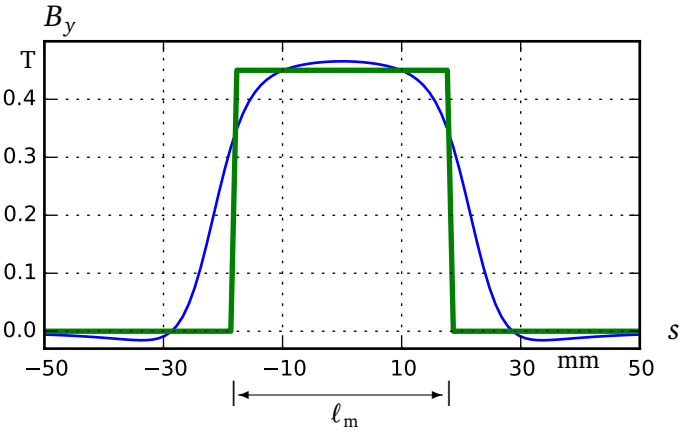

Figure 2: Approximation of the longitudinal field profile in blue by the hard-edge model in green.

A more sophisticated approach separates the magnet in three parts: The two fringe fields at the magnet extremities and the central part. The field is in this case integrated over the three corresponding parts such that Eq. (4) yields $B_1\ell_1 + B_2\ell_2 + B_3\ell_3$. The resulting field representation is more accurate and describes the longitudinal change.

A measurement procedure that is optimized to measure integrated quantities is therefore of major importance. Regardless of whether the field is measured in three sections or in one, the rotating coil acquires exactly the desired information.

Field representation on a circular domain

The representation of the magnetic field on a two-dimensional circular domain is given as an analytic function in the complex domain:

$$B_c(z) := B_y + \mathrm{i}B_x = \sum_{n=1}^{\infty} C_n \left(\frac{z}{r_0}\right)^{n-1} . \tag{5}$$

r_0 is the reference radius, on which the multipoles are defined, $z = x + \mathrm{i}\,y$ is the position in the complex domain and $C_n = B_n + \mathrm{i}A_n$ the multipole coefficients or field harmonics. These *multipoles* C_n can be computed from boundary values on the circular domain. Derivations and further analytic computations are shown in Paragraph (2.6).

2.4 Rotating-coil system

The rotating coil is a measurement device for accelerator magnets with cylindrical bore. It is designed to measure the integrated field components over a straight section to obtain the two-dimensional quantities described in Paragraph (2.3). The underlying physical principle is Faraday's law of induction (2). If correctly applied [46], a voltage signal is generated by moving a wire loop in a static magnetic field [47]. Similar configurations with a static coil and a changing magnetic field in time are not discussed here.

The rotating coil consists of a number of wire loops on a long cylinder, called shaft, with a motor-drive unit at its end. The length of the shaft is long enough to cover the entire magnetic field in longitudinal direction through the magnet. The motor rotates the shaft in a static magnetic field such that the intercepted flux changes. That results in an induced voltage signal at the end of the wire loop. The wire loop is connected to an integrator, that integrates the acquired voltage over time. As a result, the flux change over the integration time is obtained.

Rigidly attached to the shaft is an angular encoder that measures the relative angle to the starting position. In order to convert the time-dependence into an angular dependence, the angular encoder triggers the integrator at predefined angular positions. That causes the integrator to write out the flux change between two subsequent angles. The resulting outcome is the flux as a function of the angular position.

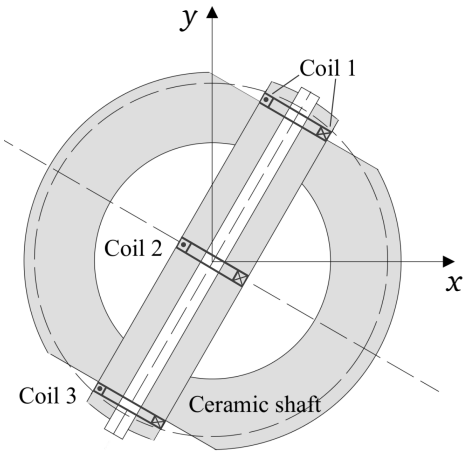

Figure 3: Cross section of a rotating coil with three tangential coils.

As the encoder triggers very often (512-1024 times for a typical measurement at the CERN laboratory [48]) per revolution, the angular increments are very small. That allows to approximate a magnetic field component from the flux through the area A that is spanned by the wire loop.

This approximation depends strongly on a good knowledge of the coil radius r_c and the opening angle δ. Since the wire position is subject to mechanical tolerances, the real area differs from the designed area. To prevent mechanical imperfections to alter the results, a good calibration is needed. Therefore, the coil is placed in a calibration magnet, which generates a magnetic field that is known to a high degree. This knowledge allows to estimate the surface A.

Fig. (1) shows a coil located on top of the yellow/beige shaft in a dipole magnet, which covers the entire magnetic field in longitudinal direction. At the far end the signal is guided to the electronics and the motor (green) is attached to make the shaft rotate. The cross section in Fig. (3) points out that there could be more than one single coil mounted on one shaft, which is in fact the more useful application. The additional coils allow to compensate the acquired signal for vibration and noise. Depending on the compensation scheme, there is a arbitrary number of coils installed. The principle of compensation is discussed and detailed in Paragraph (2.4.3).

2.4.1 Flux linkage

In this paragraph, the link between the flux and the complex field is derived. Starting in vector space, the magnetic flux Φ_m is defined as the integral of the magnetic field over the area $\mathscr{A}$ that is spanned by the wire loop:

$$\Phi_m = \int_{\mathscr{A}} \vec{B} \cdot \mathrm{d}\vec{A} = \int_0^L \int_{P_1}^{P_2} \vec{B} \cdot \mathrm{d}\vec{n}\, \mathrm{d}\ell \ . \tag{6}$$

The points P_1 and P_2 define the straight line in the transverse plane of the magnet, as shown in Fig. (4). The resolution in longitudinal direction stays untouched and is described by the variable L that stands for the longitudinal dimension of the wire loop on the shaft. In two-dimensional Cartesian coordinates, the scalar product reads as:

$$\vec{B} \cdot \mathrm{d}\vec{n} = B_x \mathrm{d}n_x + B_y \mathrm{d}n_y \ . \tag{7}$$

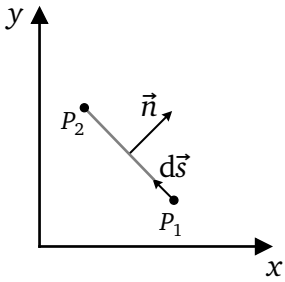

Figure 4: Coordinate system with the coil wires at P_1 and P_2.

The vector $\vec{n}$ points in normal direction out of the spanned area. In order to obtain a complex expression of the equation, the vector $d\vec{s}$ is defined, that points from P_1 to P_2. It is orthogonal to $\vec{n}$ and rotated by $\pi/2$:

$$d\vec{s} = \begin{pmatrix} dx \\ dy \end{pmatrix} = \begin{pmatrix} -dn_y \\ dn_x \end{pmatrix} . \tag{8}$$

Replacing $d\vec{n}$ in Eq. (7) with $d\vec{s}$, leads to:

$$\vec{B} \cdot d\vec{n} = B_x dy - B_y dx \ . \tag{9}$$

The right hand side holds the link to the complex notation, as it is the real part of the product $-B_c(z)(dx + i\,dy)$. With $B_c = B_y + i B_x$, their product reads as:

$$-B_c(z)(dx + i\,dy) = B_x dy - B_y dx - i\left(B_y dy + B_x dx\right) \ . \tag{10}$$

The value $dz = dx + i\,dy$ is defined as the complex equivalent of the vector $d\vec{s}$. The real part of the product $-B_c dz$ equals the scalar product $\vec{B} \cdot d\vec{n}$ in Eq. (9): $\mathrm{Re}\{B_c dz\} = -\vec{B} \cdot d\vec{n}$. That allows to transform the vectorial Eq. (6) into the complex domain:

$$\Phi_m = -\int_0^L \mathrm{Re}\left\{ \int_{z_1}^{z_2} B_c(z)\, dz \right\} d\ell \ . \tag{11}$$

z_1 and z_2 give the points P_1 and P_2 in the complex plane. The order of the integrals can be changed and the real part can be computed thereafter:

$$\Phi_\mathrm{m} = -\mathrm{Re}\left\{\int_{z_1}^{z_2}\int_0^L B_\mathrm{c}(z)\,\mathrm{d}\ell\,\mathrm{d}z\right\} . \tag{12}$$

As the rotating coil gives a strictly two-dimensional representation of the magnetic field, there is no longitudinal resolution. Therefore is the integral $\int B_\mathrm{c}\mathrm{d}\ell$ the fundamental quantity that describes the field characteristics. The integrated field is measured along the length L of the coil. Averaging the field over that length, $B_\mathrm{c}L$ is the value that describes the integrated quantity. This leads to the final equation, whereas a factor for multiple turns N_t is added:

$$\Phi_\mathrm{m} = -N_\mathrm{t}L\,\mathrm{Re}\left\{\int_{z_1}^{z_2} B(z)\,\mathrm{d}z\right\} . \tag{13}$$

The flux is often defined without the minus sign [22], and with an integration in the negative longitudinal direction: $\int_0^{-L} B_\mathrm{c}\mathrm{d}\ell$. This assumption looks rather counter-intuitive, so that here a minus sign with a positive integration path is defined. Expressing $B(z)$ with the multipole series from (5), allows the analytic integration of the integral:

$$\Phi_\mathrm{m} = -N_\mathrm{t}L\,\mathrm{Re}\left\{\sum_{n=1}^{\infty}\frac{C_n}{n\,r_0^{n-1}}\left(z_2^n - z_1^n\right)\right\} . \tag{14}$$

The measured flux is linked to the multipole errors of the field and the positions of the coil. Depending on the coil design, which defines the positions, the multipoles yield different values for the flux. This is explained by the sensitivity of a coil and described in the following paragraph.

2.4.2 Sensitivity factors

The sensitivity factors K_n characterize the coil geometry and yield a measure for the capability to acquire a certain multipole of n-th order [24]. They come from Eq. (14) and are a substitution of the geometry depending variables:

$$K_n := \frac{N_\mathrm{t}L}{n}\left(z_2^n - z_1^n\right)\mathrm{e}^{-\mathrm{i}n\theta} , \tag{15}$$

where θ is the starting angle of the coil. A rotation by this angle fixes the positions $z_1 e^{-i\theta}$ and $z_2 e^{-i\theta}$ around the positive x-axis. The sensitivity factors are therefore independent of this starting angle.

By the replacement of the sensitivity factors, Eq. (14) is noted as:

$$\Phi_m = -\mathrm{Re}\left\{\sum_{n=1}^{\infty} \frac{C_n}{r_0^{n-1}} K_n e^{in\theta}\right\} . \tag{16}$$

There are many different coil designs with different arrangement of the positions z_1 and z_2. The two standard designs of a tangential and radial coil, are detailed in the following paragraphs.

Tangential coil

The tangential coil has the wire wound on the outside of the shaft. The cross section of such a coil is shown in Fig. (3), a sketch of the angles and positions in Fig. (5). The positions z_1 and z_2 have the same radius and different angles:

$$z_1 = r_c e^{-i\delta/2} e^{i\theta} , \tag{17}$$

$$z_2 = r_c e^{i\delta/2} e^{i\theta} . \tag{18}$$

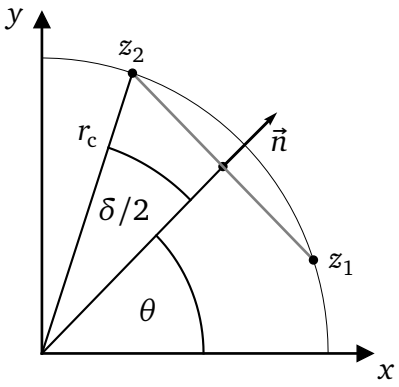

Figure 5: The angle θ, the position z_1 and z_2 and the opening angle δ for the tangential coil.

The opening angle of the coil is called δ and r_c is the coil radius. For this case, Eq. (15) gives the K_n as:

$$K_n^{\tan} = \frac{N_t L}{n} r_c^n \left(e^{i n\delta/2} - e^{-i n\delta/2}\right) \tag{19}$$

$$= 2\frac{N_t L}{n} r_c^n \sinh(i\frac{n\delta}{2}) \tag{20}$$

$$= \frac{2i N_t L}{n} r_c^n \sin\frac{n\delta}{2} \,. \tag{21}$$

With these sensitivity factors, the flux from Eq. (16) reads:

$$\Phi_m = -\mathrm{Re}\left\{2i N_t L r_0 \sum_{n=1}^{\infty} \frac{C_n}{n}\left(\frac{r_c}{r_0}\right)^n \sin\frac{n\delta}{2}\, e^{i n\theta}\right\} \,. \tag{22}$$

In order to get high sensitivity factors, the coil radius r_c must be large. Furthermore depends the sensitivity on the opening angle δ. The term $\sin(n\delta/2)$ is shown for different δ in Fig. (6).

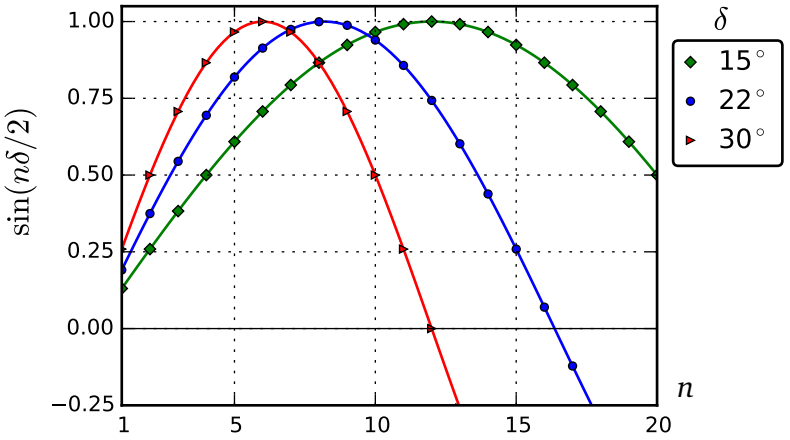

Figure 6: The term $\sin(n\delta/2)$ computed over the multipole order n: For different opening angles δ, the period of the sine term changes and gives better sensitivity to certain multipoles.

Depending on the opening angle δ, the sensitivity on the multipoles changes. For a large opening angle, for example 30°, the sensitivity is highest for the multipole order $n = 6$, but falls off very fast. At multipole order $n = 12$, it has zero sensitivity, called the *blind eye* in the magnetic measurement community. The multipole of this order can not be measured with a coil of that opening angle. The lower orders, however, are measured with a high sensitivity.

Coils with small opening angles shift the blind eye to a higher multipole order. For the case of $\delta = 15°$, the blind eye is at $n = 24$, a multipole order, whose multipole is in most of the cases very small. That comes with the trade-off of less sensitivity on the lower-order multipoles $n < 10$.

Advantageous of the design scheme of the tangential coil, is most of all the easy building procedure and the convincing design of the coils stacked on each other. That allows compact and robust mechanics, that are stable against vibrations and alignment errors. On the other hand, it lacks sensitivity and precision on the higher-order multipoles around its blind eye and even before. An opening angle of $\delta = 28.8°$ was used for the LHC measurement procedure for example [49]. That choice was considered as a good compromise for the sensitivity on the expected multipoles.

Radial coil

The wires of the radial coil are on two different radii at the same angle. The cross section of such a coil is shown in Fig. (8), whereas the angles and positions are marked in Fig. (7).

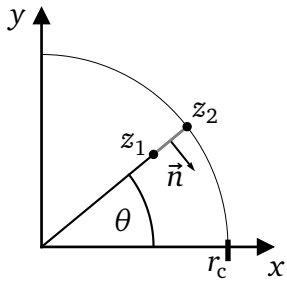

Figure 7: The angle θ and the positions z_1, z_2 for the radial coil.

The positions z_1 and z_2 have the same angle θ and are at:

$$z_1 = r_\mathrm{i}\,\mathrm{e}^{\mathrm{i}\,\theta}\ , \tag{23}$$

$$z_2 = r_\mathrm{c}\,\mathrm{e}^{\mathrm{i}\,\theta}\ . \tag{24}$$

These values characterize the inner radius r_i and outer radius r_c. That yields a

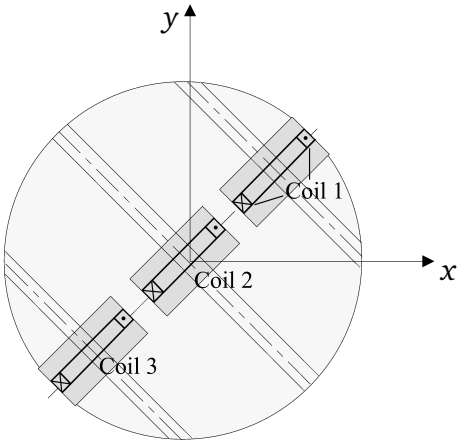

Figure 8: Cross section of a rotating coil with three radial coils.

sensitivity factors of:

$$K_n^\mathrm{rad} = \frac{N_\mathrm{t} L}{n}\left(r_\mathrm{c}^n - r_\mathrm{i}^n\right)\ . \tag{25}$$

The flux is consequently:

$$\Phi_\mathrm{m} = -\mathrm{Re}\left\{N_\mathrm{t} L \sum_{n=1}^{\infty} \frac{C_n}{n r_0^{n-1}}\left(r_\mathrm{c}^n - r_\mathrm{i}^n\right)\mathrm{e}^{\mathrm{i}n\theta}\right\}\ . \tag{26}$$

To express the multipoles at the outer coil radius r_c, the reference radius r_0 is set to r_c. Applying this transformation, it holds:

$$\Phi_m = -\mathrm{Re}\left\{ N_t L \sum_{n=1}^{\infty} \frac{r_c C_n}{n} \left[1 - \left(\frac{r_i}{r_c} \right)^n \right] e^{i n \theta} \right\} . \tag{27}$$

The inner term

$$\left[1 - \left(\frac{r_i}{r_c} \right)^n \right] \tag{28}$$

yields the dependency on the multipole order n. The inner radius divided by the coil radius is a value between 1 and 0, even though the ratio is usually larger than 0.5 to leave space for a central coil.

Fig. (9) shows the term for different ratios over the multipole order. The sensitivity for that coil is monotonically increasing for a growing multipole order n and has no trade-off in an analytic sense. The lower the ratio r_i/r_c, the larger the coil width and the better the sensitivity.

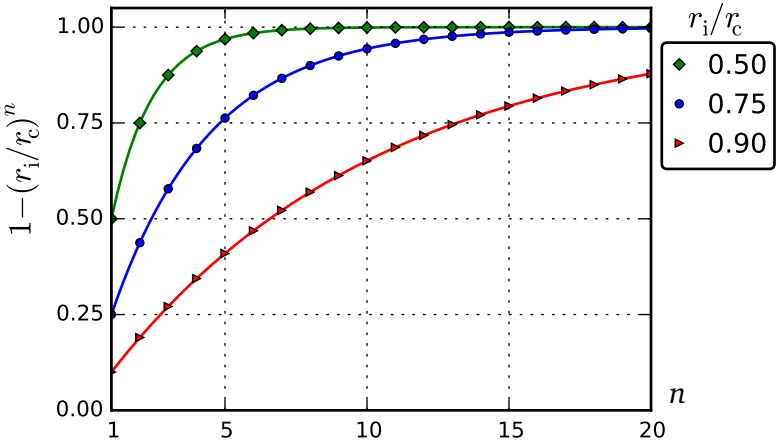

Figure 9: The term $1-(r_i/r_c)^n$ over the multipole order n: The lower the ratio r_i/r_c, the higher the sensitivity especially on the lower-order multipoles.

Recent advances with printed circuit boards (PCB) make this design applicable in the CERN laboratories, even though the manufacturing process is dif-

ficult for larger coils [50], as industrial production is usually limited to small boards (< 1 m). Moreover is the detection of fabrication errors cumbersome and specialized tools are not developed yet. Short coils (< 300 mm of length), however, can be designed to follow industrial standards [51] and are used to measure short magnets.

Dipole coil

The so-called dipole coil is a coil that is located at the center of the shaft. It rotates around its central point and has therefore special properties. The sensitivity factors and the intercepted flux can be derived from the tangential and the radial coil. Fig. (10) shows the positions and the angle $\tilde{\theta}$, which equals

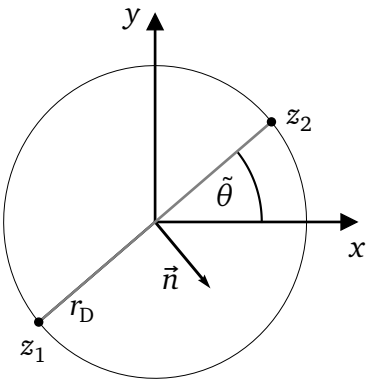

Figure 10: The angle $\tilde{\theta}$ and the positions z_1, z_2 for the dipole coil.

the initial angle of the radial coil. For the tangential coil, however, the angle is different: The initial angle θ defines the direction of the vector $\vec{n}$. Therefore, the angle $\tilde{\theta} - \pi/2$ yields the initial angle of the dipole coil, if it is seen as a tangential coil.

In order to be consistent with the former derivations, the vector $\vec{n}$ is set to have z_1 on the right and z_2 on the left in positive direction. The radial dimension of the dipole coil is defined by the radius r_D.

Considering the rotated starting angle, the sensitivity factors coming from the tangential coil are according to Eq. (21):

$$K_n^{\tan} = \frac{2\mathrm{i}N_t L}{n} r_D^n \sin\frac{n\pi}{2} \mathrm{e}^{-\mathrm{i}n\pi/2} \ . \tag{29}$$

For integer n, the term $\sin(n\pi/2)$ is zero for even n and alternates ± 1 for odd n. In addition with the rotation $\mathrm{e}^{-\mathrm{i}n\pi/2} = \cos(n\pi/2) - \mathrm{i}\sin(n\pi/2)$, the equation transforms to:

$$K_n^{\tan} = \frac{2N_t L}{n} r_D^n \sin^2\frac{n\pi}{2} \tag{30}$$

$$= \frac{2N_t L}{n} r_D^n \ , \qquad \text{for} \quad n \in \{1,3,5,7\ldots\} \ . \tag{31}$$

The derivations from the radial coil from Eq. (25) lead to the same result:

$$K_n^{\mathrm{rad}} = \frac{N_t L}{n}\left(r_D^n - (-r_D)^n\right) \tag{32}$$

$$= \frac{N_t L}{n} r_D^n \left(1 - (-1)^n\right) \ . \tag{33}$$

These sensitivity factors give a flux that depends on the odd multipoles only:

$$\Phi_m = -\mathrm{Re}\left\{2N_t L r_0 \sum_{n=1,3,5}^{\infty} \frac{C_n}{n}\left(\frac{r_D}{r_0}\right)^n \mathrm{e}^{\mathrm{i}n\tilde{\theta}}\right\} \ . \tag{34}$$

In a dipole coil, the even multipoles are, cause of the symmetry, not measurable. Consequently, the coil measures only the components of the dipole, sextupole and so forth. This is the property that allows the compensation of the dipole component, which is explained in the following.

2.4.3 Compensation of the main field component

The compensation for vibrations and measurement noise of any kind is one of the benefits of the rotating coil against other devices. The basic principle is that the acquired signal is not coming from one coil only, but the differential signal of several coils is used. These coils are all rigidly attached to the same shaft, so that vibrations and other mechanical errors affect them in the same way. Then, the differential signal is free of that kind of perturbation, and the signal is much more precise. Furthermore have the electronics a finite resolution such that

only a limited number of bits have to represent the voltage signal. The number of significant digits is therefore higher, if both, the direct and the differential signal, are acquired separately.

The compensation of the main field component, also called *bucking*, yields a much better signal-to-noise ratio for the higher-order multipoles than the main field component. This gain in precision is quantified as the *bucking ratio* [52], which is often between 100 and 1000.

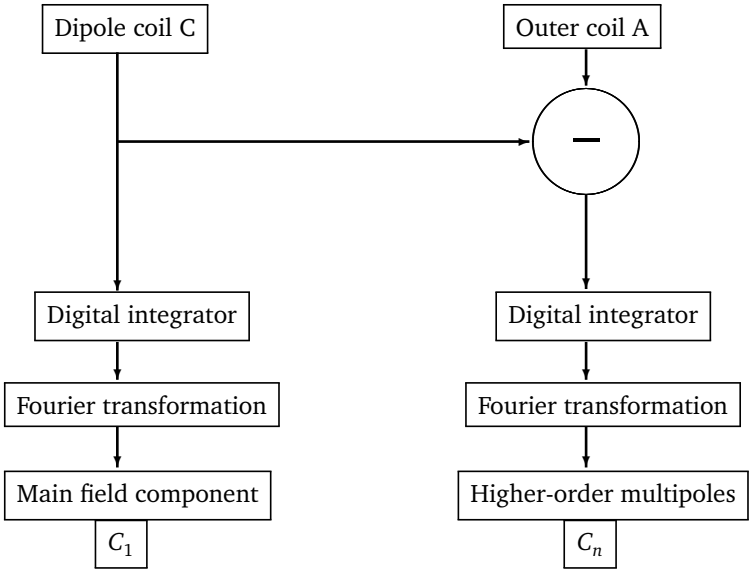

Figure 11: Analog compensation scheme: The voltage signals of the different coils are connected to separate the main field component of the higher-order multipoles.

The full field representation is the superposition of the different portions of the field. The differential signal describes the higher-order multipoles, the main field component is still coming from the direct, the absolute signal. Fig. (11) shows the principle of the data acquisition of the analog compensation by the example of a dipole. The terminals of the coils are mechanically connected in a way, that the resulting voltage is the differential signal.

There is also digital compensation [22], where the signals are first acquired and then digitally subtracted. That needs very good electronics and a very precise acquisition system and is not used in the CERN laboratory [53]. The following paragraphs explain the different compensation schemes.

Dipole compensation scheme

Fig. (12) shows the cross section of a shaft with a tangential coil and a dipole coil, Coil A and Coil C, respectively. The width of the coils equals and is $2r_\mathrm{D}$ and the number of wire loops N_t is also the same. Furthermore are the coils orientated in the same direction such that a constant dipole field causes the same flux through the coils. Assumption for the following calculations are perfect geometries and no mechanical imperfections.

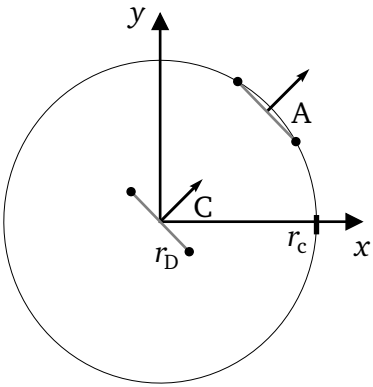

Figure 12: The two positions of the Coils A and C for the dipole compensation. The width of the coils is given by $2r_\mathrm{D}$.

The central Coil C, the dipole coil, is sensitive to all the odd multipoles. The reference radius r_0, where the multipoles are presented, is set to the outer coil radius r_c. From Eq. (34), the flux through the central Coil C equals:

$$\Phi_\mathrm{m}^{(\mathrm{C})} = -\mathrm{Re}\left\{ 2\mathrm{i} N_\mathrm{t} L r_\mathrm{c} \sum_{n=1,3,5}^{\infty} \frac{C_n}{n} \left(\frac{r_\mathrm{D}}{r_\mathrm{c}}\right)^n \sin\frac{n\pi}{2}\, \mathrm{e}^{\mathrm{i}n\theta} \right\} . \tag{35}$$

With the same reference radius, the flux through the tangential Coil A simplifies. The term r_c/r_0 becomes one, so that Eq. (22) reads:

$$\Phi_\mathrm{m}^{(\mathrm{A})} = -\mathrm{Re}\left\{ 2\mathrm{i} N_\mathrm{t} L r_\mathrm{c} \sum_{n=1}^{\infty} \frac{C_n}{n} \sin\frac{n\delta}{2}\, \mathrm{e}^{\mathrm{i}n\theta} \right\} . \tag{36}$$

The wires of Coil A and Coil C are connected with opposing polarity such that the induced voltages subtract each other. The flux through the connected wires equals the difference of the flux of the two coils:

$$\Phi_{\mathrm{m}}^{(\mathrm{A-C})} = \Phi_{\mathrm{m}}^{(\mathrm{A})} - \Phi_{\mathrm{m}}^{(\mathrm{C})} \,. \tag{37}$$

The compensated flux $\Phi_{\mathrm{m}}^{(\mathrm{A-C})}$ can be quantified further:

$$\Phi_{\mathrm{m}}^{(\mathrm{A-C})} = -\mathrm{Re}\left\{ 2\mathrm{i} N_{\mathrm{t}} L r_{\mathrm{c}} \, \mathrm{e}^{\mathrm{i}n\theta} \left[\sum_{n=1}^{\infty} \frac{C_n}{n} \sin\frac{n\delta}{2} - \sum_{n=1,3,5}^{\infty} \frac{C_n}{n} \left(\frac{r_{\mathrm{D}}}{r_{\mathrm{c}}}\right)^n \sin\frac{n\pi}{2} \right] \right\} \,. \tag{38}$$

With the factor r_{c} inside, the term in the square brackets is analyzed separately:

$$\left[\sum_{n=1}^{\infty} \frac{C_n}{n} r_{\mathrm{c}} \sin\frac{n\delta}{2} - \sum_{n=1,3,5}^{\infty} \frac{C_n}{n} r_{\mathrm{c}} \left(\frac{r_{\mathrm{D}}}{r_{\mathrm{c}}}\right)^n \sin\frac{n\pi}{2} \right] . \tag{39}$$

From Fig. (5) follows $r_{\mathrm{c}} \sin\delta/2 = r_{\mathrm{D}}$ so that for $n = 1$ the entries are equal:

$$\left[C_1 r_{\mathrm{c}} \sin\frac{\delta}{2} - C_1 r_{\mathrm{c}} \frac{r_{\mathrm{D}}}{r_{\mathrm{c}}} \sin\frac{\pi}{2} \right] \tag{40}$$

$$= [C_1 r_{\mathrm{D}} - C_1 r_{\mathrm{D}}] = 0 \,. \tag{41}$$

The flux from the dipole component is constant in space and therefore equal in both coils. The entries for the sextupole component with $n = 3$ are:

$$\left[\frac{C_3}{3} r_{\mathrm{c}} \sin\frac{3\delta}{2} - \frac{C_3}{3} r_{\mathrm{c}} \left(\frac{r_{\mathrm{D}}}{r_{\mathrm{c}}}\right)^3 \sin\frac{3\pi}{2} \right] \tag{42}$$

$$= \frac{C_3}{3} r_{\mathrm{c}} \left[\sin\frac{3\delta}{2} + \left(\frac{r_{\mathrm{D}}}{r_{\mathrm{c}}}\right)^3 \right] \tag{43}$$

$$= \frac{C_3}{3} r_{\mathrm{c}} \left[\sin\frac{3\delta}{2} + \sin^3\frac{\delta}{2} \right] . \tag{44}$$

The sine terms are smaller than one, so that exponent of three makes the term $\sin^3(\delta/2)$ a small value. The influence of the sextupole term of the central coil is small, as shown in Fig. (13). It is in the range of 1 % of the sextupole component measured by the outer coil for opening angles of about 20°. Usually, the measurement accuracy on the multipoles is lower than that, so that

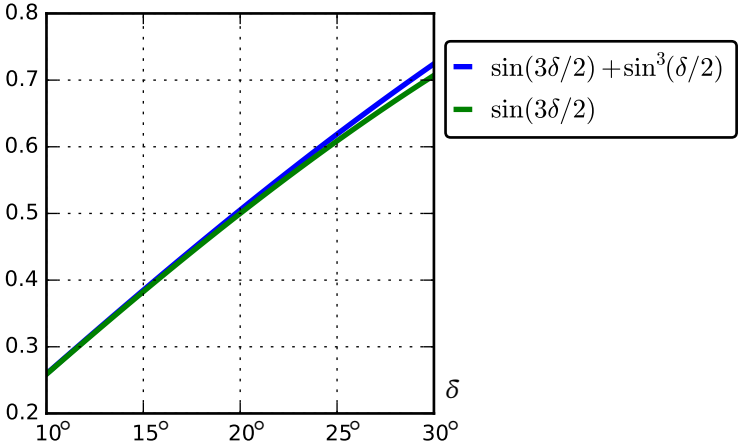

Figure 13: Green: The sextupole term $\sin(3\delta/2)$ measured by the outer Coil A only. Blue (upper): The sextupole measured by both coils. The effect of the central coil is small, in particular for small opening angles δ.

an approximation can be made. Otherwise, the sextupole measurement can be corrected after the measurement, with the given equations. For the higher orders $n \in \{5,7,9...\}$, the term $(r_D/r_c)^n$ becomes much smaller, such that the effect is even lower.

Under the assumption, that the central coil adds only the dipole field, the Eq. (38) can be simplified to:

$$\Phi_m^{(A-C)} \approx -\mathrm{Re}\left\{ 2i N_t L r_c \, e^{in\theta} \sum_{n=2}^{\infty} \frac{C_n}{n} \sin\frac{n\delta}{2} \right\} . \tag{45}$$

The flux is free of the constant dipole field, as the sum starts from two. Therefore, the acquired signal is much smaller and the complete resolution of the acquisition system can be used for the higher-order multipoles.

Quadrupole compensation

The quadrupole compensation scheme is more sophisticated, as the quadrupolar field component is not constant but grows linearly in space. That is why, two additional coils are needed to intercept the flux at two supplementary positions. There are many different schemes possible that position the coils on

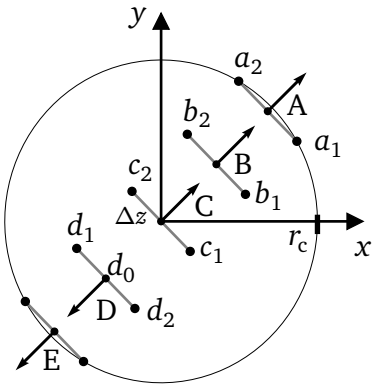

Figure 14: The positions a_1, a_2, ... d_1, d_2 for the quadrupole compensation. The four Coils A-D at four different positions are used.

well-defined positions. In the following, a design with five coils stacked on each other is presented.

Fig. (14) shows five tangential coils with the same width and regular distances. The complex numbers a_1, a_2, ..., d_1, d_2 define the coil positions, and a_0, b_0, c_0, d_0 give the central points of the corresponding coils. For visibility only d_0 is marked in the figure. Coil E is not used in the presented compensation scheme, but stabilizes the rotation of the shaft.

To filter the dipole component, the flux of the central coil is subtracted from the outer Coil A. Using the derivations in Paragraph (2.4.3), the flux of Coil A minus the flux of Coil C gives the dipole-free flux. To suppress the quadrupole component, the flux of Coil B plus the flux of Coil D is also subtracted, whereas the direction of the flux is defined in positive radial direction. The calculations are clearer in the complex plane, avoiding the sensitivity factors.

For a quadrupole compensation in this scheme, every coil has the same number of turns N_t. The central points of the Coils A, B and D have a defined relation:

$$a_0 = 2b_0 = -2d_0 \ . \tag{46}$$

Furthermore, the geometry is defined by:

$$b_1 = -d_1 \ , \tag{47}$$

$$b_2 = -d_2 \ . \tag{48}$$

Because of the constant width, the distance from the coil center to the coils is:

$$\Delta z = a_2 - a_0 = b_2 - b_0 = c_2 = d_1 - d_0 \ . \tag{49}$$

Starting with the Eq. (14), the sum of the flux of Coil B and Coil D, reads as:

$$\Phi_{\mathrm{m}}^{(\mathrm{B+D})} = -N_{\mathrm{t}} L \,\mathrm{Re}\left\{ \sum_{n=1}^{\infty} \frac{C_n}{n\, r_0^{n-1}} \left[\left(b_2^n - b_1^n \right) + \left(d_2^n - d_1^n \right) \right] \right\} \ . \tag{50}$$

The position depending term transforms with Equations (47) and (48) to:

$$\left[b_2^n - b_1^n + (-b_2)^n - (-b_1)^n \right] \tag{51}$$

$$= \left(b_2^n - b_1^n \right) \left(1 + (-1)^n \right) . \tag{52}$$

For odd n, the expression and the flux becomes zero, and for even n, the flux becomes:

$$\Phi_{\mathrm{m}}^{(\mathrm{B+D})} = -N_{\mathrm{t}} L \,\mathrm{Re}\left\{ \sum_{n=2,4,6\ldots}^{\infty} \frac{2C_n}{n\, r_0^{n-1}} \left[b_2^n - b_1^n \right] \right\} \ . \tag{53}$$

The addition of the flux of Coil D to Coil B doubles the values of the even multipoles and makes the odd multipoles vanish. Thus, the dipole, sextupole, and so forth are not measured.

Now, the flux of Coil B and D gets subtracted from the flux of Coil A minus Coil C. As shown before, the flux $\Phi_m^{(\mathrm{A-C})}$ is free of the dipole component. Without the substitution of the sensitivity factors K_n, this flux reads as:

$$\Phi_{\mathrm{m}}^{(\mathrm{A-C})} = -N_{\mathrm{t}} L \,\mathrm{Re}\left\{ \sum_{n=2}^{\infty} \frac{C_n}{n\, r_0^{n-1}} \left[a_2^n - a_1^n \right] \right\} \ . \tag{54}$$

The sum start from $n = 2$ with the quadrupole component. Subtraction of the flux $\Phi_m^{(B+D)}$ gives:

$$\Phi_{\mathrm{m}}^{(\mathrm{A-C-B-D})} = \Phi_{\mathrm{m}}^{(\mathrm{A-C})} - \Phi_{\mathrm{m}}^{(\mathrm{B+D})} \tag{55}$$

$$= -N_{\mathrm{t}} L \,\mathrm{Re}\left\{ \sum_{n=2}^{\infty} \frac{C_n}{n\, r_0^{n-1}} \left[a_2^n - a_1^n\right] - \sum_{n=2,4,6\ldots}^{\infty} 2\frac{C_n}{n\, r_0^{n-1}} \left[b_2^n - b_1^n\right] \right\} .$$

For the even n, the geometrical factors are combined by means of Eq. (46) and (49):

$$\left[a_2^n - a_1^n\right] - 2\left[b_2^n - b_1^n\right] \tag{56}$$

$$= \left[(a_0 + \Delta z)^n - (a_0 - \Delta z)^n\right] - 2\left[(b_0 + \Delta z)^n - (b_0 - \Delta z)^n\right] \tag{57}$$

$$= \left[(2b_0 + \Delta z)^n - (2b_0 - \Delta z)^n\right] - 2\left[(b_0 + \Delta z)^n - (b_0 - \Delta z)^n\right] . \tag{58}$$

The effect on the quadrupole component for $n = 2$ is:

$$(2b_0 + \Delta z)^2 - (2b_0 - \Delta z)^2 - 2(b_0 + \Delta z)^2 + 2(b_0 - \Delta z)^2 \tag{59}$$

$$= ((2b_0)^2 + 4b_0\Delta z + \Delta z^2) - ((2b_0)^2 - 4b_0\Delta z + \Delta z^2)$$
$$- 2(b_0^2 + 2b_0\Delta z + \Delta z^2) + 2(b_0^2 - 2b_0\Delta z + \Delta z^2) . \tag{60}$$

The quadratic terms single out and the rest simplifies to:

$$4b_0\Delta z + 4b_0\Delta z - 4b_0\Delta z - 4b_0\Delta z = 0 . \tag{61}$$

The quadrupole term vanishes. Thus, the overall flux can be written as:

$$\Phi_{\mathrm{m}}^{(\mathrm{A-C-B-D})} = -N_{\mathrm{t}} L \,\mathrm{Re}\left\{ \sum_{n=3}^{\infty} \frac{C_n}{n\, r_0^{n-1}} \left[a_2^n - a_1^n\right] - \sum_{n=4,6\ldots}^{\infty} 2\frac{C_n}{n\, r_0^{n-1}} \left[b_2^n - b_1^n\right] \right\} . \tag{62}$$

The effect of the term from the flux $\Phi_{\mathrm{m}}^{(\mathrm{B+D})}$ decreases with the multipole order. The quadrupole term is the identical, the octupole (C_4) 28 % and the C_6 8 % of the flux $\Phi_{\mathrm{m}}^{(\mathrm{A-C})}$. A quadrupole compensation in this design deletes the quadrupole, but also changes the other even multipoles. These terms are relatively large and must be considered in the results. Fig. (15) shows the effect of the quadrupole compensation on the multipoles to measure.

The quadrupole compensation is inevitable for a precise measurement of a quadrupole or sextupole. The presented building procedure is straightforward and allow to keep the mechanical uncertainties low. However, there are many other coil configurations to compensate the quadrupole, which are not detailed in this work.

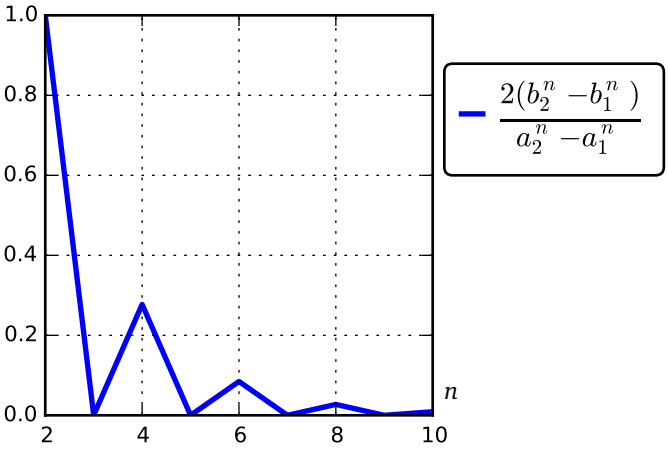

Figure 15: The relative effect of the flux $\Phi_m^{(B+D)}$ on the multipoles coming from the flux $\Phi_m^{(A-C)}$ over the multipole order n. The quadrupole term ($n = 2$) is the same and therefore compensated. The multipoles C_4 and C_6 have relative large values (28 % and 8 %) and influence the measurement.

2.5 Error sources

Every measurement is affected by uncertainties, every measured value comes with error bars. For a measurement with a rotating coil, there are many different reasons why the acquired data is not perfect. For example, the shaft does not rotate perfectly around its axis, nor are the coil windings perfectly manufactured. These kind of errors are analyzed in Paragraph (2.5.1).

The combination of measurements comes necessarily with another source of error: The uncertainty of the positioning. Whenever several measurements are combined, the relative position of the measurement must be known. The effect of the positioning error is detailed in Paragraph (2.5.2).

Both error sources affect the multipoles and the field representation, but the underlying principle of the added noise is different. The multipoles are altered in different ways. The corresponding discussion is found in Paragraph (2.5.3).

2.5.1 Measurement uncertainty

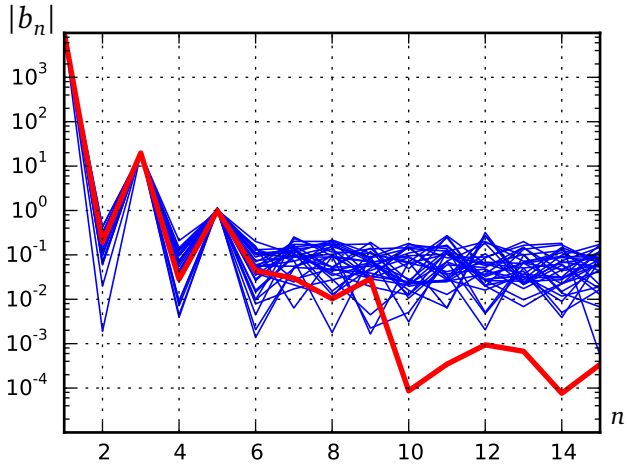

Figure 16: The absolute value of the normalized multipoles of Table (4) without noise in red (thick). 30 runs of random noise of a computed normal distribution with $\sigma_m = 0.1$ on the same multipoles in blue.

A single magnetic measurement by the rotating coil is affected by several sources of errors, such as mechanical vibrations, coil-calibration errors, noise in the readout electronics and mechanical imperfections of the coil itself [54]. Due to the compensation, these errors can be reduced for the higher-order multipoles, as vibrations of the shaft affect both coils in the same way. For the main field component the absolute/uncompensated signal is used, which is about two orders of magnitude less precise than the higher-order multipoles [22].

There are many different sources of errors, which propagate to the multipoles. Studies of repeated measurements show that the noise distribution is approximately uniform on the multipoles for orders lower than the blind eye [48], see Fig. (18). Therefore, the noise level can be expressed by one value, that gives the noise level on each multipole. Nevertheless, the single noise values can be very different, as they are assumed to be random. In the simu-

lations in this work, the measurement error is given by a normal distribution around zero. The value σ_m yields the standard deviation and the noise on each multipole is computed separately by means of random numbers.

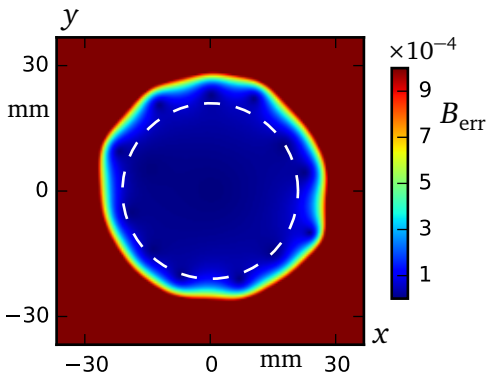

Figure 17: The difference of the noisy field B and the original field B_o, related to the central field value: $B_\mathrm{err} = |B - B_\mathrm{o}|/|B_\mathrm{o}(0)|$. The white dashed circle symbolizes the path along the coil radius: $r_\mathrm{c} e^{i\varphi}$, with $\varphi \in [0, 2\pi]$. The computed noise level on the multipoles is defined by $\sigma_\mathrm{m} = 0.1$.

As the multipoles usually fall off with the multipole order, the noise becomes more dominant for the higher orders. There, the effect is relatively higher and the perturbation stands out. Fig. (16) shows a typical measurement of a dipole with its simulated multipoles in red and 20 measured, noisy multipoles in blue with a noise level of $\sigma_\mathrm{m} = 0.1$ on the normalized multipoles. In the logarithmic scale of the graph, the noise is marginally visible on multipoles with large values, as $|b_3|$ and $|b_5|$. On the other hand, the measured higher-order multipoles are indistinguishable from the noise floor for a multipole order larger than 9.

The noise floor affects the field description inside and outside of the coil radius in different ways: A noise value of 0.1 on the normalized c_{13} for example, is multiplied by $(z/r_0)^{12}$, as stated in Eq. (5). With a coil radius (white line in Fig. (17)) of the reference radius $r_\mathrm{c} = r_0$, the factor is very large outside the coil radius ($z > r_\mathrm{c}$) and very small inside ($z < r_\mathrm{c}$). Depending on the position, the error on the field is therefore dominated by different multipoles. Moreover is the field representation outside the coil radius very error-prone, as seen in Fig. (17).

Under the assumption of a constant noise level on the multipoles, the relative field error grows rapidly outside the coil radius. To avoid this extrapolation of

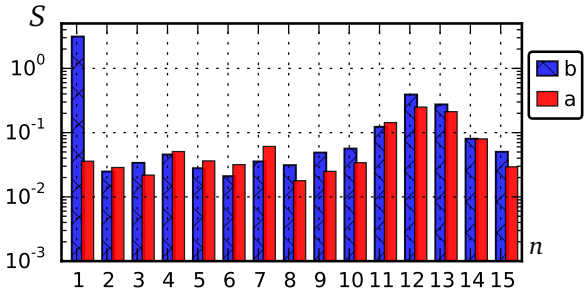

Figure 18: Sample standard deviation for ten measurements of the dipole in Paragraph (5.1) in logarithmic scale, normalized to the mean of the main field component B_1 and multiplied by 10^4.

the measurement data, measurements are usually performed with the shaft with the largest coil radius for the magnet aperture.

The sample standard deviation of the multipoles for ten measurements is shown in Fig. (18). It shows the relatively low precision on the main field component and on the multipoles around the blind eye. The multipoles of order 2 to 10, however, have the best precision and similar values.

2.5.2 Positioning uncertainties

Besides the common measurement error, a combination of measurements introduces a positioning error. The position of the shaft and its coil is only known to a certain extent. Depending on the positioning system and the environment, systematic and random errors are introduced.

The positioning and alignment of the magnet and the shaft is usually precise (20 - 100 μm) for measurements at room temperature. In this case the position can be controlled mechanically with precision stages or optically with a laser tracker. However, larger positioning errors are expected when the shaft is not easily accessible. This may be the case if the magnet is measured in a cryostat for example. Additional flanges and cold-warm transitions do not allow the tracking of the coil motion by means of optical systems. Thus, the positioning errors extend from some micrometers to the range of millimeters.

Effect on the multipoles

The feed-down formula computes the multipoles in a reference frame, which is displaced by a positioning error Δz. For this problem, the formula holds the error on the measurement and reads as:

$$\tilde{C}_n = \sum_{k=n}^{\infty} C_k \binom{k-1}{k-n} \left(\frac{\Delta z}{r_\mathrm{c}}\right)^{k-n} . \tag{63}$$

The $\tilde{C}_n$ are the displaced multipoles coming from the original C_k. The first entry of the sum ($k = n$) holds the multipole of the left side. It is not changed, because the binomial factor as well as the last term are one. Regarding only the change of the original value, the equation can be rewritten as:

$$\Delta C_n = \tilde{C}_n - C_n = \sum_{k=n+1}^{\infty} C_k \binom{k-1}{k-n} \left(\frac{\Delta z}{r_\mathrm{c}}\right)^{k-n} . \tag{64}$$

Equation (64) holds the change on the multipole of order n, if the measurement position is changed by Δz. Important for this analysis is the change in position and the resulting influence on the multipole.

Estimation of the positioning error

To apply Eq. (64), the ratio $\lambda := \Delta z / r_\mathrm{c}$ has to be estimated. As stated before, the term is usually small, but can be large for difficult environments. For a positioning system with a precision of 20 μm and a coil radius of 20 mm, λ is smaller than 10^{-3}. In a less controlled environment, as in a cryostat, the uncertainty of the positioning could be much higher, for example 2 mm. With the same coil radius, λ can grow up to 0.1. The two cases $\lambda_\mathrm{h} = 10^{-3}$ and $\lambda_\ell = 10^{-1}$ are analyzed as a ratio for a high-precision positioning and for low precision, respectively. This range will cover most of the possible build-ups.

Error propagation

The terms of Eq. (64) are difficult to combine and are analyzed separately. The quotient $\lambda = \Delta z / r_\mathrm{c}$ has the exponent $k - n$ and falls off exponentially ($r_\mathrm{c} \gg \Delta z$). The binomial coefficient is more difficult to understand. Fig. (19) shows the Pascal's triangle, which is a graphical representation of the binomial coefficients. The marked paths show the quantity for a fixed n and a growing k of the term $\binom{k-1}{k-n}$. The green (upper) path is marked for $n = 5$ and equals the series $v_k = \binom{k-1}{k-5} = 5, 15, 35, 70, \ldots$ for $k \in \mathbb{N}$, $k > n$. The red path is marked for $n = 11$ and its series reads as $w_k = 11, 66, 286, 1001, \ldots$ These series are

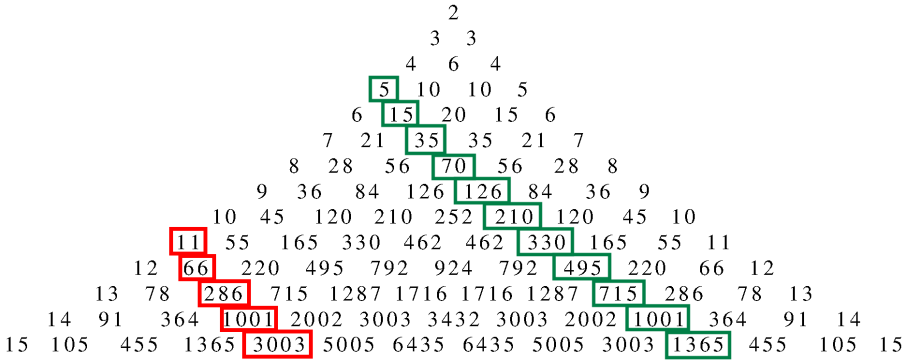

Figure 19: Pascal's triangle showing the binomial coefficients.

multiplied by the corresponding multipole and by the quotient λ^{k-n}. For the latter one the high-precision value $\lambda_\mathrm{h} = 10^{-3}$ is chosen at first:

$$n = 5: \qquad v_k^{(\mathrm{h})} = \lambda_\mathrm{h}^{k-n} v_k = 0.005,\ 1.5 \cdot 10^{-6},\ 3.5 \cdot 10^{-8}, \ldots \tag{65}$$

$$n = 11: \qquad w_k^{(\mathrm{h})} = \lambda_\mathrm{h}^{k-n} w_k = 0.011,\ 6.6 \cdot 10^{-5},\ 2.8 \cdot 10^{-7}, \ldots\ . \tag{66}$$

These values are very small such that the influence on the products $C_k w_k^{(\mathrm{h})}$ and $C_k v_k^{(\mathrm{h})}$ can be estimated as much smaller than the measurement noise. On the other side, the λ_ℓ for an imprecise knowledge of the position gives different results:

$$n = 5: \qquad v_k^{(\ell)} = \lambda_\ell^{k-n} v_k = 0.5,\ 0.15,\ 0.035,\ 0.007, \ldots \tag{67}$$

$$n = 11: \qquad w_k^{(\ell)} = \lambda_\ell^{k-n} w_k = 1.1,\ 0.66,\ 0.286, 0.11, \ldots\ . \tag{68}$$

Even for the lower-order multipole $n = 5$, the series has relatively high values. Consulting Eq. (64), the effect has to be considered: The multipole $\tilde{C}_5$ is raised by 50 % of C_6, 15 % of C_7, 3.5 % of C_8 and so on. In the other example of the high multipole order $n = 11$, the perturbation is even larger: C_{12} is added by 110 % and C_{13} by 66 %. Thus, the large uncertainty on the positioning can only be accepted for the higher-order multipoles, if they decrease fast enough to compensate the effect.

Table 1: The binomial coefficient $\binom{k-1}{k-n}$ for $n \in [2,15]$ and $k \in [n+1, n+8]$.

n \ $k \longrightarrow$	$n+1$	$n+2$	$n+3$	$n+4$	$n+5$	$n+6$	$n+7$	$n+8$
2	2	3	4	5	6	7	8	9
3	3	6	10	15	21	28	36	45
4	4	10	20	35	56	84	120	165
5	5	15	35	70	126	210	330	495
6	6	21	56	126	252	462	792	1287
7	7	28	84	210	462	924	1716	3003
8	8	36	120	330	792	1716	3432	6435
9	9	45	165	495	1287	3003	6435	12870
10	10	55	220	715	2002	5005	11440	24310
11	11	66	286	1001	3003	8008	19448	43758
12	12	78	364	1365	4368	12376	31824	75582
13	13	91	455	1820	6188	18564	50388	125970

Multiplication factor

For a better understanding of the product $\binom{k-1}{k-n}\lambda^{k-n}$, Pascal's triangle is modified. The original one for the binomial coefficient is in rectangular form in Tab. (1), where the binomial coefficient $\binom{k-1}{k-n}$ is shown. The same entries as before are marked for $n = 5$ (green) and $n = 11$ (red). In the next step the table is multiplied once by λ_h and once by λ_ℓ to cover the complete product. Since λ falls off fast, only a few terms in k are shown.

The Table (2) shows the coefficients of the higher multipoles. It completes the Equations (65) to (68) for other values of n. As stated before, the effect on the multipoles for the high-precision positioning is very low, whereas the low-precision positioning shows larger effects. The table shows the dependency on n and the linear increase for $k = n+1$ and a larger growth for $k > n+1$. The effect on the multipoles grows with the multipole order, whereby the lower orders are less affected.

With an approximate knowledge of the multipoles, the table allows to estimate the effect of the positioning error.

Table 2: The term $\binom{k-1}{k-n}\lambda^{k-n}$ for positioning with high precision (λ_h) and low precision (λ_ℓ), with $k \geq n+1$.

	$\lambda_\mathrm{h} = 0.001$		
n	$k \longrightarrow$		
2	0.002	3e-6	4e-9
3	0.003	6e-6	1e-8
4	0.004	1e-5	2e-8
5	0.005	2e-6	4e-8
6	0.006	2e-5	5e-8
7	0.007	3e-5	8e-8
8	0.008	4e-5	1e-7
9	0.009	5e-5	2e-7
10	0.010	6e-5	2e-7
11	0.011	7e-5	3e-7
12	0.012	8e-5	4e-7
13	0.013	9e-5	5e-7
14	0.014	1e-4	6e-7
15	0.015	1e-4	7e-7

	$\lambda_\ell = 0.1$			
n	$k \longrightarrow$			
2	0.2	0.03	0.01	0.001
3	0.3	0.06	0.01	0.002
4	0.4	0.10	0.02	0.003
5	0.5	0.15	0.04	0.007
6	0.6	0.21	0.06	0.01
7	0.7	0.28	0.08	0.02
8	0.8	0.36	0.12	0.03
9	0.9	0.45	0.17	0.05
10	1.0	0.55	0.22	0.07
11	1.1	0.66	0.29	0.11
12	1.2	0.78	0.36	0.14
13	1.3	0.91	0.46	0.18
14	1.4	1.05	0.56	0.24
15	1.5	1.24	0.68	0.31

2.5.3 Comparison of error sources

Comparing both errors sources, the positioning errors and measurement noise, reveals the underlying principle of the error propagation: The noise on the measurement manifest itself as an additive term on the multipoles while the positioning error is characterized by the feed-down formula, which depends on the strength of the multipole field errors themselves. Thus, the measurement error describes an independent field that is added as a perturbation to the original one. The positioning error, in contrast, is defined by the original field itself.

As an example, the positioning error has no effect in a perfect dipolar field, as the field is constant and does not change in position. Furthermore, in a pure quadrupole field, the error increases linearly with the displacement and the strength of the quadrupole. Hence, the positioning error depends on the multipoles and is crucial in magnets with high field errors.

To analyzed the effect on the multipoles, the two cases are studied: A multipole $\tilde{C}_n^{(\mathrm{p})}$ is affected by a positioning error and $\tilde{C}_n^{(\mathrm{m})}$ by a measurement error. The original multipole C_n is change by a positioning error of Δz to:

$$\tilde{C}_n^{(\mathrm{p})} = \sum_{k=n} C_k \binom{k-1}{k-n} \left(\frac{\Delta z}{r_0}\right)^{k-n} . \tag{69}$$

Computed by the feed-down formula, as stated above, the perturbation depends on the multipoles C_k and therefore on the field errors themselves.

The alternation cause by the measurement error ΔC_n is described by:

$$\tilde{C}_n^{(\mathrm{m})} = C_n + \Delta C_n . \tag{70}$$

Here, the magnetic field of Eq. (5) can be noted as:

$$\tilde{B}_{\mathrm{c}}^{(\mathrm{m})}(z) = \sum_{n=1}^{\infty} \tilde{C}_n \left(\frac{z}{r_0}\right)^{n-1} \tag{71}$$

$$= \sum_{n=1}^{\infty} (C_n + \Delta C_n) \left(\frac{z}{r_0}\right)^{n-1} \tag{72}$$

$$= \sum_{n=1}^{\infty} C_n \left(\frac{z}{r_0}\right)^{n-1} + \sum_{n=1}^{\infty} \Delta C_n \left(\frac{z}{r_0}\right)^{n-1} \tag{73}$$

$$\Leftrightarrow \quad \tilde{B}_{\mathrm{c}}^{(\mathrm{m})}(z) = B_{\mathrm{c}}(z) + \Delta B_{\mathrm{c}}(z) . \tag{74}$$

The measurement error describes an additional field that is completely separable from the original field.

2.6 Multipole representation

As stated in Paragraph (2.3), the field description used in this work is an analytic function in the complex domain [55, 56]. It is widely used and in accordance with the calculations for the dynamic aperture for the beam dynamics [57]. The analytic function reads as:

$$B_c(z) = B_y + \mathrm{i}B_x = \sum_{n=1}^{\infty} C_n \left(\frac{z}{r_0}\right)^{n-1} . \tag{75}$$

r_0 is the reference radius, $z = x + \mathrm{i}y$, and $C_n = B_n + \mathrm{i}A_n$. As an analytic function, the field representation is valid in a source-free domain and, by means of the boundary values, uniquely defined.

The graphical representation of the formula is shown in Fig. (20). The magnetic field $B_c(z)$ is expressed for one term of the sum. As the multipoles are defined on a reference radius r_0, the vector fields are plotted on a circular domain. An ideal, normal dipole has a B_1 component and all the other components are zero. This example is shown in the top left corner in the figure. The field has $2n$ poles on a complete circle for a multipole C_n.

The complex coefficients $C_n = B_n + \mathrm{i}A_n$ can be determined by field data on a circular closed boundary. Having the radial field component $B_r(r_0, \varphi)$ on the reference radius from measurements or computations, allows to find a solution for the boundary value problem. The link between the circular coordinates and the Cartesian ones, is done via a rotation of the components. Using the definition of the complex field B_c, the radial field component is:

$$B_r = B_x \cos\varphi + B_y \sin\varphi \tag{76}$$

$$\Leftrightarrow \quad B_r = \mathrm{Im}\{B_c\}\cos\varphi + \mathrm{Re}\{B_c\}\sin\varphi \ . \tag{77}$$

In order to express this equation at the reference radius, the complex field is expressed first at $z = r_0 \mathrm{e}^{\mathrm{i}\varphi}$:

$$B_c(r_0\mathrm{e}^{\mathrm{i}\varphi}) = \sum_{n=1}^{\infty} C_n \left(\frac{r_0\mathrm{e}^{\mathrm{i}\varphi}}{r_0}\right)^{n-1} = \sum_{n=1}^{\infty} C_n \mathrm{e}^{\mathrm{i}(n-1)\varphi} . \tag{78}$$

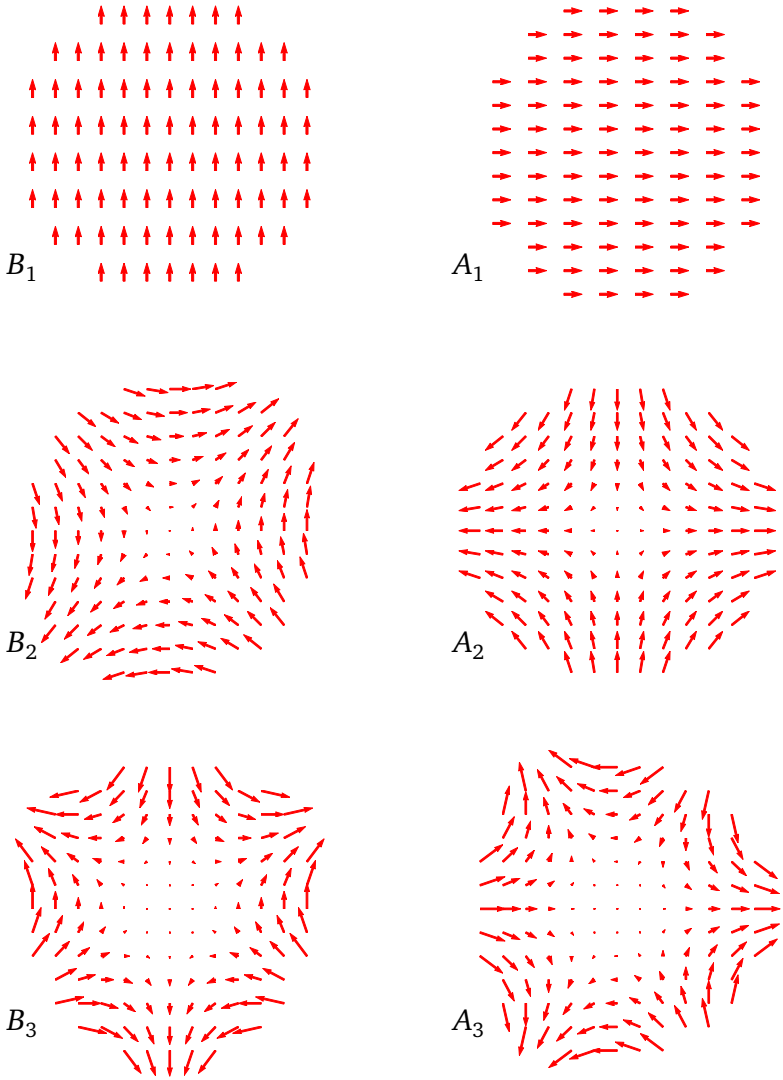

Figure 20: The computed vector fields of the first three multipoles from top to bottom: dipole, quadrupole and sextupole. The real (normal) components $B_{1,2,3}$ left, the imaginary (skew) components $A_{1,2,3}$ right.

Applying the Euler formula ($e^{ix} = \cos x + i \sin x$) and the separation of the real and imaginary part, transforms the equation to:

$$B_c(r_0 e^{i\varphi}) = \sum_{n=1}^{\infty} C_n \big(\cos(n-1)\varphi + i \sin(n-1)\varphi \big) \tag{79}$$

$$= \sum_{n=1}^{\infty} \big(B_n + iA_n \big) \big(\cos(n-1)\varphi + i \sin(n-1)\varphi \big) \tag{80}$$

$$= \sum_{n=1}^{\infty} \Big[B_n \cos(n-1)\varphi - A_n \sin(n-1)\varphi + \\ + i \big(B_n \sin(n-1)\varphi + A_n \cos(n-1)\varphi \big) \Big] . \tag{81}$$

Here, the B_x- and the B_y-components can be identified by real and imaginary part of B_c:

$$B_x = \sum_{n=1}^{\infty} \Big[B_n \sin(n-1)\varphi + A_n \cos(n-1)\varphi \Big] , \tag{82}$$

$$B_y = \sum_{n=1}^{\infty} \Big[B_n \cos(n-1)\varphi - A_n \sin(n-1)\varphi \Big] . \tag{83}$$

Continuing now with Eq. (77), the radial component of the field is:

$$B_r(r_0, \varphi) = \sum_{n=1}^{\infty} \Big[B_n \sin(n-1)\varphi + A_n \cos(n-1)\varphi \Big] \cos\varphi + \tag{84}$$

$$+ \sum_{n=1}^{\infty} \Big[B_n \cos(n-1)\varphi - A_n \sin(n-1)\varphi \Big] \sin\varphi$$

$$= \sum_{n=1}^{\infty} \Big[B_n \big(\sin(n-1)\varphi \cos\varphi + \cos(n-1)\varphi \sin\varphi \big) + \\ + A_n \big(\cos(n-1)\varphi \cos\varphi - \sin(n-1)\varphi \sin\varphi \big) \Big] . \tag{85}$$

The addition theorem of trigonometric functions hold for the arguments $(n-1)\varphi$ and φ:

$$\sin n\varphi = \sin\big((n-1)\varphi + \varphi\big) = \sin(n-1)\varphi\cos\varphi + \cos(n-1)\varphi\sin\varphi \ , \tag{86}$$

$$\cos n\varphi = \cos\big((n-1)\varphi + \varphi\big) = \cos(n-1)\varphi\cos\varphi - \sin(n-1)\varphi\sin\varphi \ . \tag{87}$$

The right-hand side of Eq. (86) and (87) can be identified in Eq. (85), where the corresponding terms can be substituted:

$$B_r(r_0,\varphi) = \sum_{n=1}^{\infty}\Big(B_n\sin n\varphi + A_n\cos n\varphi\Big) \ . \tag{88}$$

The coefficients A_n and B_n can now be identified as the Fourier coefficients of the known $B_r(r_0)$ over a complete period from 0 to 2π in φ. With the definition of the Fourier series or a development in the orthogonal functions sine and cosine, the coefficients are determined. Either way, the Fourier coefficients are computed by:

$$A_n = \frac{1}{\pi}\int_0^{2\pi} B_r(r_0,\varphi)\cos n\varphi \,\mathrm{d}\varphi \ , \tag{89}$$

$$B_n = \frac{1}{\pi}\int_0^{2\pi} B_r(r_0,\varphi)\sin n\varphi \,\mathrm{d}\varphi \ . \tag{90}$$

The magnetic field is represented in its complex form, as noted in Eq. (5). The coefficients $C_n = B_n + \mathrm{i}A_n$ are determined by the Fourier series of the radial field component at the reference radius r_0.

In the magnet design community, the real parts B_n are called the *normal* components, the imaginary parts A_n define the *skew* components.

2.6.1 Reference radius and scaling law

The multipoles are defined on an associated reference radius and are explicitly written as $C_n(r_1)$. Changing the reference radius in Eq. (5), results in a direct change of the multipoles. As a general example, the multipoles at a reference radius r_1 are changed to another radius r_2. The magnetic field remains the same, so that it holds:

$$\sum_{n=1}^{\infty} C_n(r_1)\left(\frac{z}{r_1}\right)^{n-1} = B_c(z) = \sum_{n=1}^{\infty} C_n(r_2)\left(\frac{z}{r_2}\right)^{n-1} . \tag{91}$$

Comparing the coefficients of the series, yields

$$\frac{C_n(r_1)}{r_1^{n-1}} = \frac{C_n(r_2)}{r_2^{n-1}} , \tag{92}$$

from which follows

$$C_n(r_2) = \left(\frac{r_2}{r_1}\right)^{n-1} C_n(r_1) . \tag{93}$$

To change the reference radius from one value to another, the multipoles are multiplied with a scaling factor that grows exponentially with the multipole order n.

2.6.2 Analytic continuation of the field representation

With the analytic continuation of analytic functions [58], it is possible to represent the multipole errors in a displaced reference frame. The displaced positions are called z_i, as it is meaningful for the combination in the next section. The transformation reads as: $z \to z'$, $z' := z - z_i$. As this displacement stays within the bore of the magnet, free of magnetic material and current sources, the path between z and z' remains zero-homotopic as required by the method of analytic continuation. For the magnetic flux being invariant with respect to the frame change, it holds

$$\sum_{n=1}^{\infty} C_n(z_0)\left(\frac{z}{r_0}\right)^{n-1} = B_c(z) = \sum_{n=1}^{\infty} C'_n(z_i)\left(\frac{z'}{r_0}\right)^{n-1} , \tag{94}$$

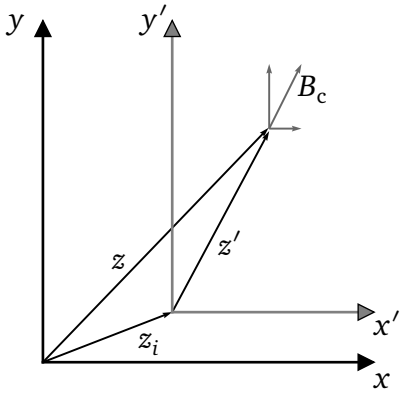

Figure 21: The complex magnetic field B_c in the original and displaced reference frame.

where z_i are the position of the displaced measurements. Using the binomial series expansion for the term $(z' + z_i)^{n-1}$, the left-hand side of Equation (94) can be transformed as follows:

$$\sum_{n=1}^{\infty} C_n(z_0)\left(\frac{z}{r_0}\right)^{n-1} = \sum_{n=1}^{\infty} C_n(z_0)\left(\frac{z'+z_i}{r_0}\right)^{n-1}$$
$$= \sum_{n=1}^{\infty}\sum_{k=1}^{n} C_n(z_0)\binom{n-1}{k-1}\left(\frac{z'}{r_0}\right)^{k-1}\left(\frac{z_i}{r_0}\right)^{n-k} . \qquad (95)$$

Rearranging the double sum [23] according to $\sum_{n=1}^{\infty}\sum_{k=1}^{n} a_{nk} = \sum_{k=1}^{\infty}\sum_{n=k}^{\infty} a_{nk} = \sum_{n=1}^{\infty}\sum_{k=n}^{\infty} a_{kn}$. with followed comparison to the right hand side of Eq. (94):

$$\sum_{n=1}^{\infty}\sum_{k=n}^{\infty} C_k(z_0)\binom{k-1}{n-1}\left(\frac{z'}{r_0}\right)^{n-1}\left(\frac{z_i}{r_0}\right)^{k-n} = \sum_{n=1}^{\infty} C_n'(z_i)\left(\frac{z'}{r_0}\right)^{n-1} . \qquad (96)$$

Comparing the coefficients and using the identity $\binom{a}{b} = \binom{a}{a-b}$ finally results in:

$$C_n'(z_i) = \sum_{k=n}^{\infty} C_k(z_0)\binom{k-1}{k-n}\left(\frac{z_i}{r_0}\right)^{k-n} . \qquad (97)$$

For practical tasks, the series is truncated at an index K and makes it an approximation:

$$C_n'(z_i) \approx \sum_{k=n}^{K} C_k(z_0) \binom{k-1}{k-n} \left(\frac{z_i}{r_0}\right)^{k-n} . \tag{98}$$

Every multipole measured with the displaced coil is coupled to every higher-order multipole in the reference frame. This effect is know as feed-down in the magnet-design community [59].

2.6.3 Normalization and rotation

The quality and the field homogeneity of accelerator magnets are usually well optimized by design, such that the higher-order field harmonics are less than one unit in 10^{-4}. Thus, the multipoles are normalized to the main field component and multiplied by 10^4. The resulting values are dimensionless and called *units*. Moreover, they are written in lower-case characters, such that the normalized multipoles are $c_n = b_n + \mathrm{i}\, a_n$.

The normalization by a main field component B_M is given by:

$$c_n := \frac{10^4}{B_M} C_n . \tag{99}$$

The number M is the order of the main field component. It holds $M = 1$ for a dipole and $M = 2$ for a quadrupole and so forth. As a result, the main component is $B_M = 10^4$ and the other components are relative to that value.

A common practice is to rotate the multipoles to have a main field component that is free of a skew term: $A_M = 0$. For the example of a dipole as the main field, the multipole C_1 is shown in the complex domain in Fig. (22). The angle τ is defined by the equation:

$$\tan\tau = \frac{A_1}{B_1} . \tag{100}$$

Changing C_1 such that A_1 is zero, the complex number has to be rotated by τ in mathematically negative sense. Thus, the rotated multipole reads as:

$$\tilde{C}_1 = C_1\, \mathrm{e}^{-\mathrm{i}\,\tau} . \tag{101}$$

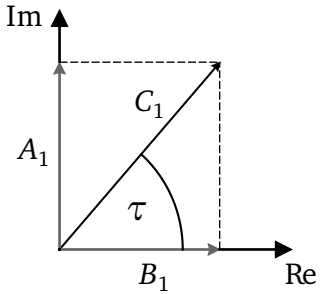

Figure 22: The complex number $C_1 = B_1 + \mathrm{i}A_1$ in the complex domain. τ is the argument or phase of C_1 and the angle of rotation.

Rotating higher-order multipoles

The other multipoles also have to be rotated in order to keep the field consistent. This transformation equals a rotation of the reference frame, which has different effects on the multipoles. Applying a rotation by the angle $-\tau$, changes the multipole C_n to:

$$\tilde{C}_n = C_n \, \mathrm{e}^{-\mathrm{i}n\tau} \ . \tag{102}$$

The larger the multipole order n, the larger the angle of rotation.

2.6.4 Allowed multipoles

A magnetic field of one pure multipole is impossible, since every real magnet has finite dimensions and the material is subject to saturation effects and eddy-currents. Due to symmetries in the magnet design, every magnet type has multipoles that occur naturally for that specific type. These harmonics are called *allowed* multipoles [60].

For a dipole, the allowed multipoles are of order $m = 2n + 1 = \{3,5,7,\ldots\}$ with $n \in \mathbb{N}^+$. In a quadrupole, the multipoles of order $m = 4n + 2 = \{6,10,14,\ldots\}$ are the allowed ones. A general formula for a main field component of order M, reads as $m = M(2n + 1)$.

A magnet has also unallowed harmonics coming from mechanical defects and tolerances in the production process. The allowed multipoles usually dominate the field errors.

2.7 Combining magnetic field measurements

In the magnetic measurement community there are different approaches to combine magnetic field measurements. The common goal is to obtain the multipole coefficients by using a different technique than a simple rotating-coil measurement. This is important for situations, when no adequate rotating coil shaft is available or when the magnet has an aperture that is not suitable for a measurement on a circular trajectory.

A Hall sensor can be used to map the three-dimensional field with subsequent integration along the longitudinal direction. Expressing these integrated quantities on a circular domain allows to compute the multipoles. This procedure is time-consuming and additionally not very accurate. Limited by the accuracy of the Hall sensor, this approach is usually disadvantageous [61].

The single stretched wire acquires the magnetic field integrated over the longitudinal dimension. With the acquired data at arbitrary positions, the multipole coefficients can be computed by means of a least square fit and matrix algebra [62]. The accuracy, which mostly depends on the positioning stages, comes from the stretched wire system and is in the range of 10^{-4}. The computations in the used matrix formalism are also noted for measurement data from a rotating-coil system [63]. The calculations use the magnetic field including the imprecise main field component. The results of these calculations are consequently less precise than the compensated data.

A different approach uses data from rotating coil-measurements and computes elliptic multipoles [28]. The measurement positions are fixed to cover an area describable by an ellipse. The computation of theses elliptical coefficients depends on the magnetic field along the elliptic boundary. The field information are again less precise than the compensated multipoles. Furthermore is this approach applicable only for elliptical domains and it does not allow to handle large symmetric apertures (quadrupoles for example) with a small shaft. It is, however, useful for magnets with rectangular aperture. Within its accuracy this procedure combines the field information to have a representation on the larger domain. An approach to correct the inaccuracies [64] can improve the results.

Elliptical multipoles yield a valid field representation on the elliptical domain. The important information for the particle motion, however, are usually expressed in circular multipoles. Therefore, the circular harmonics have to be computed from the elliptical multipoles in a subsequent step.

A combination that uses the compensated multipoles of a rotating-coil measurement by avoiding the main field component is presented in the following. There, the high precision is preserved throughout the computations.

3 Combining rotating-coil measurements

In this chapter the combination of rotating-coil measurements is presented [65]. First, the feed-down formula is noted for several measurements at different positions. Secondly, an equation system is given, that links the different multipoles. This equation system can be presented in matrix form, which gives further possibilities. This matrix is analyzed for different measurement positions and parameters in order to find the optimal configuration. Finally, the method of least squares is introduced and applied to give the final results.

The derivations in the following are first generic but then with the focus on dipole measurements. In a later paragraph the changes to a quadrupole measurement are explained.

3.1 General configuration

The presented method is useful for magnets with an aperture that is larger in at least one dimension than the diameter of the used measurement coil. In this case, additional measurements help to increase the quality of the field representation. The description of the method is made very general with variables holding the critical parameters so that the method stays applicable for many different situations.

Using the method, the number of measurement positions I must be chosen. The positions can lie on a circle, in the mid-plane or unstructured spread in the aperture - as long as the positions are known, the method does not set any restrictions. Then, the number of multipoles N that the coil has to acquire must be set. This value strongly depends on the coil characteristics and its sensitivity depending on the multipole order. The other parameters have a minor effect and are discussed in detail in the Paragraph (3.4).

3.2 Theory of field reconstruction

The combination relies on the link between measured multipoles at a displaced position and the global multipoles in the reference frame. The link works via the feed-down formula and the scaling law. The multipoles measured with a coil of radius r_c at a position z_i are called $C'_n(r_c, z_i)$, whereas the reconstructed, global multipoles are called $C_k(r_0, z_0)$.

The measurements from the small coil are first scaled according to

$$C'_n(r_0, z_i) = C'_n(r_c, z_i)\left(\frac{r_0}{r_c}\right)^{n-1} \tag{103}$$

and then expressed in the displaced reference frame using the feed-down formula from Eq. (98):

$$C'_n(r_0, z_i) = \sum_{k=n}^{K} C_k(r_0, z_0) \binom{k-1}{k-n} \left(\frac{z_i}{r_0}\right)^{k-n} . \tag{104}$$

The left sides of Eq. (103) and (104) are the same and can be compared:

$$C'_n(r_c, z_i) \left(\frac{r_0}{r_c}\right)^{n-1} = \sum_{k=n}^{K} C_k(r_0, z_0) \binom{k-1}{k-n} \left(\frac{z_i}{r_0}\right)^{k-n} \tag{105}$$

$$\Rightarrow \quad \boxed{C'_n(r_c, z_i) = \sum_{k=n}^{K} C_k(r_0, z_0) \binom{k-1}{k-n} \left(\frac{z_i}{r_0}\right)^{k-n} \left(\frac{r_c}{r_0}\right)^{n-1}} . \tag{106}$$

The Eq. (106) links the multipoles from the measurements to the multipoles to be reconstructed in the reference frame. The multipoles $C'_n(r_c, z_i)$ are measured at the position z_i with a rotating coil of radius r_c and the multipoles $C_k(r_0, z_0)$ are at the origin z_0 with a reference radius r_0. The multipoles C_k are unknown for all $k \in [2, K]$ and need at least $K-1$ equations to determine them. Independent of the measurement position, the reconstructed multipoles stay always the same. Thus, the Eq. (106) can be noted for different measured multipoles C'_n and for different positions z_i to get enough equations to find a solution for the unknowns.

3.2.1 The linear equation system

Eq. (106) holds the link from one measured multipole C'_n at one position z_i to all the central multipoles to reconstruct. For several multipoles at different positions, the equation is applied for different variables. First, for better readability, Eq. (106) can be written as

$$C'_n(r_c, z_i) = \sum_{k=n}^{K} w^{(i)}_{n,k} \, C_k(r_0, z_0) \, , \tag{107}$$

$$\text{with} \qquad w^{(i)}_{n,k} = \binom{k-1}{k-n} \left(\frac{z_i}{r_0}\right)^{k-n} \left(\frac{r_c}{r_0}\right)^{n-1} . \tag{108}$$

Then, the sum can be noted explicitly for different multipole orders n and different measurement positions z_i:

$$\begin{aligned}
C_2'(r_c,z_1) = \quad & w_{2,2}^{(1)}\,C_2(r_0,z_0) + w_{2,3}^{(1)}\,C_3(r_0,z_0) + w_{2,4}^{(1)}\,C_4(r_0,z_0) + \ldots + w_{2,K}^{(1)}\,C_K(r_0,z_0) \\
C_3'(r_c,z_1) = \quad & w_{3,3}^{(1)}\,C_3(r_0,z_0) + w_{3,4}^{(1)}\,C_4(r_0,z_0) + \ldots + w_{3,K}^{(1)}\,C_K(r_0,z_0) \\
\vdots \quad & \qquad\qquad (109) \\
C_2'(r_c,z_2) = \quad & w_{2,2}^{(2)}\,C_2(r_0,z_0) + w_{2,3}^{(2)}\,C_3(r_0,z_0) + w_{2,4}^{(2)}\,C_4(r_0,z_0) + \ldots + w_{2,K}^{(2)}\,C_K(r_0,z_0) \\
C_3'(r_c,z_2) = \quad & w_{3,3}^{(2)}\,C_3(r_0,z_0) + w_{3,4}^{(2)}\,C_4(r_0,z_0) + \ldots + w_{3,K}^{(2)}\,C_K(r_0,z_0) \\
\vdots \quad &
\end{aligned}$$

The vertical dots stand for more equation up to multipole order N, the limit of the used measured multipoles. Starting from the quadrupole component C_2', the number of equations is $N-1$. For every position i, these $N-1$ equations are noted so that in total $I\,(N-1)$ information are known to compute the $K-1$ unknowns.

3.2.2 Matrix formalism

The equation system (109) can be written in matrix notation as

$$\{C'\} = [M]\{C\}\,, \tag{110}$$

where the elements in the matrix $[M] \in \mathbb{C}^{(N-1)I\times(K-1)}$ are functions of the radii, the measurement positions and the binomial coefficients of the series representation. The vector $\{C'\} \in \mathbb{C}^{(N-1)I}$ is complex-valued and contains the measured field harmonics, $\{C\} \in \mathbb{C}^{K-1}$ contains the multipoles in the reference frame. Both start from the quadrupole component to avoid the main component in a dipole. As stated in Paragraph (2.5.1), the main field component is less accurate than the other multipoles. The column vectors are

$$\{C'\} = \Big(C_2'(z_1),\ C_3'(z_1), \cdots, C_N'(z_1),\ C_2'(z_2), \cdots, C_N'(z_2), \cdots\Big)^{\mathrm{T}}\,, \tag{111}$$

$$\{C\} = \Big(C_2,\ C_3, \ldots, C_{\mathrm{K}}\Big)^{\mathrm{T}}\,. \tag{112}$$

The block matrix $[M]$ is composed of I inner matrices $[W_i]$, one for every measurement position:

$$[M] = \begin{pmatrix} [W_1] \\ \vdots \\ [W_i] \\ \vdots \\ [W_I] \end{pmatrix} . \tag{113}$$

The inner matrices are upper trapezoidal matrices of the type

$$[W_i] = \begin{pmatrix} w_{2,2}^{(i)} & \cdot & \cdot & \cdot & \cdot & \cdots & w_{2,K}^{(i)} \\ 0 & \cdot & \cdot & \cdot & \cdot & \cdot & \cdots \\ 0 & 0 & \cdot & \cdot & w_{n,k}^{(i)} & \cdot & \cdots \\ \vdots & \vdots & \ddots & \cdot & \cdot & \cdots & \\ 0 & 0 & \cdots & 0 & \cdot & w_{N,K-1}^{(i)} & w_{N,K}^{(i)} \end{pmatrix} . \tag{114}$$

The matrix elements $w_{n,k}^{(i)}$ of $[W_i]$ depend on all variables n, k, and i and are, as noted in Eq. (108):

$$w_{n,k}^{(i)} = \binom{k-1}{k-n} \left(\frac{z_i}{r_0}\right)^{k-n} \left(\frac{r_c}{r_0}\right)^{n-1} . \tag{115}$$

The equation system described by the matrix [M] must be over-determined, because of the noisy measurement data as input. A well-determined system would be too affected by measurement errors. Therefore, $(N-1)I$ is larger than $K-1$.

Fig. (23) shows the matrix $[M]$ for an exemplary case of three positions. The first and last position have the same distance to the origin $|z_i|$ so that the modulus of the entries is equal. The second measurement position, however, is moved 10 % closer to the origin, causing the entries to be lower, because of the lower ratio (z_i/r_0). Every further position creates another inner matrix and is added at the bottom.

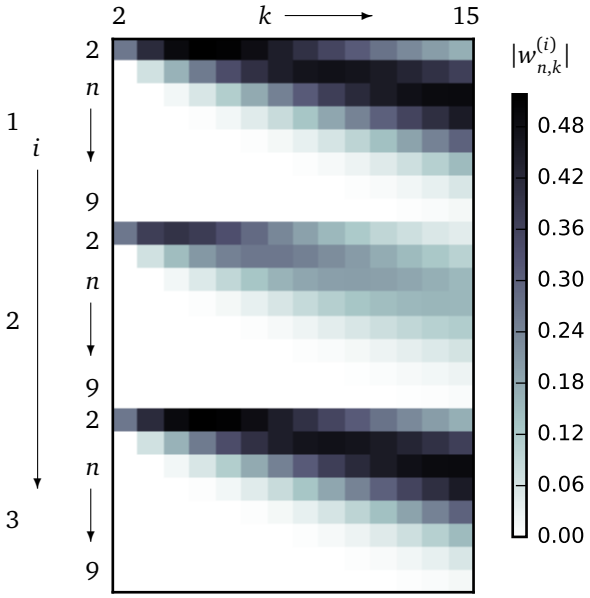

Figure 23: The absolute values of the computed entries $w^{(i)}_{n,k}$ of the matrix $[M]$, that consists of three inner matrices.

3.3 Method of least squares

An over-determined system of equations has an infinite number of solutions. The standard procedure for these problems is the method of least squares, which minimizes the error of the best fit to the equation system. The matrix equation (110) is first multiplied by the transpose of $[M]$ and then multiplied by the inverse of the square matrix $[M][M]^T$:

$$\begin{aligned} [M]^T\{C'\} &= [M]^T[M]\{C\} \\ \Leftrightarrow \quad \left([M]^T[M]\right)^{-1}[M]^T\{C'\} &= \{C\}\,. \end{aligned} \tag{116}$$

Computing these equations for the measurement positions and the measured multipoles, yields the reconstructed multipoles at the reference radius. These computations were made by library packages that are available as free software, nominally the Linear Algebra Package (Lapack) [66] with the QR-factorization

was used in a Fortran program. A later version used SciPy [67] and NumPy [68] in the computer language Python.

The computations are accurate within machine precision and very fast (< 1 sec) on a usual desktop computer.

3.4 Configuration parameters

The above analysis works under the assumption, that the field is described by a finite number of coefficients. In this work, this limit K is set to 15, whereas multipoles of higher order are not part of the solution. K must to be high enough so that the excluded multipoles are small and with a minor influence on the field description.

Table 3: The used variables and subscripts.

N	Highest multipole order acquired by the small coil	
K	Number of reconstructed multipoles on the ref. radius r_0	
I	Number of measurement positions	
n	Multipole order of measurement with small coil	$n \in [2,N]$
k	Multipole order of field reconstruction on the ref. radius	$k \in [2,K]$
i	Enumerator for the measurement position	$i \in [1,I]$
r_0	Reference radius	
r_c	Measurement radius of the small coil	
z_0	Origin of the reference system in the complex plane	
z_i	Positions of the measurements in the complex plane	
C'_n	Measured multipoles on the small shaft	
C_k	Reconstructed multipoles on the reference radius	

The highest multipole order used from the measurements, is called N. It holds the number of multipoles computed from the signal acquired by the coil. These parameters are not fixed by the method itself, but must be set in advance by the operator. The right choice depends on factors like the coil sensitivity and the measurement environment. These and the other used symbols are summarized in Table (3). In order to understand the influence of each parameter, the condition number is analyzed as an indicator for the error propagation.

3.5 Condition number

The condition number κ yields a measure of the error amplification of a matrix inversion and the robustness of that procedure [69]. Moreover, it indicates, how much an aberration of the matrix entries distort the result of the inversion. The

number is defined by the ratio of the largest to the lowest singular value of the matrix. These values are easily computable by the singular value decomposition and describe the inner characteristics of a matrix.

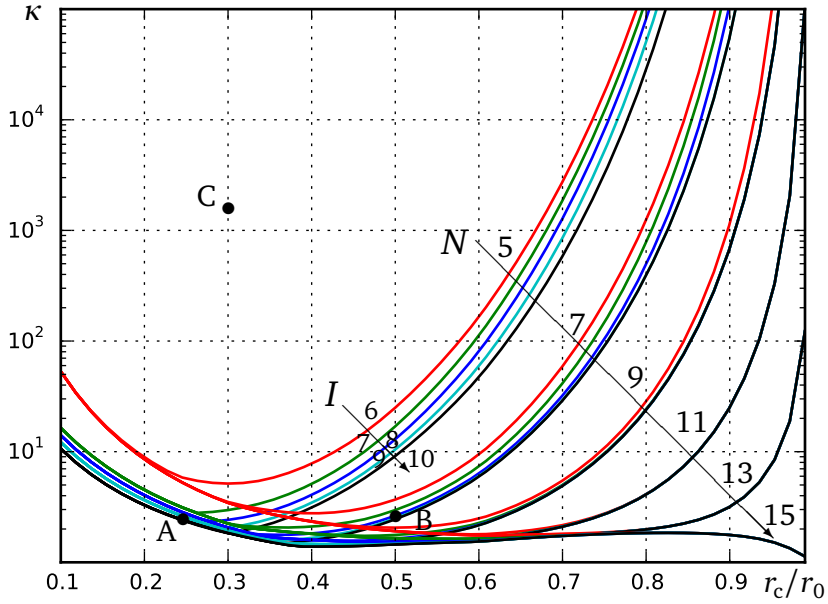

Figure 24: The computed condition number κ as a function of the quotient r_c/r_0 for different numbers of measured multipoles N and number of measurements I. The maximum number of multipoles for the field reconstruction is $K = 15$. The exemplary Setups A-C are marked for $N = 8$.

Fig. (24) shows the condition numbers as a function of the parameters N and I, as well as the size of the measurement coil r_c normalized with respect to the reference radius. The number of reconstructed multipoles is in all cases $K = 15$, while the coil is placed at equiangular positions on the radius $r_0 - r_c$. The condition number takes its minimum of 1, when one central measurement with $r_c = r_0$ is used to measure the 15 multipoles because the matrix [M] is simply the identity matrix. Well-conditioned equation systems also result when $r_c/r_0 \approx 0.4$ and 7-9 multipoles are considered from the measurements. It is easy to see from Fig. (24) that larger coils ($r_c/r_0 > 0.5$) require the measurement

of a larger number of multipole coefficients ($N \geq 8$) to yield a good condition number of $\kappa < 10$. Smaller coils require a larger number of measurements ($I \geq 10$), but less multipole coefficients to yield a well-conditioned equation system.

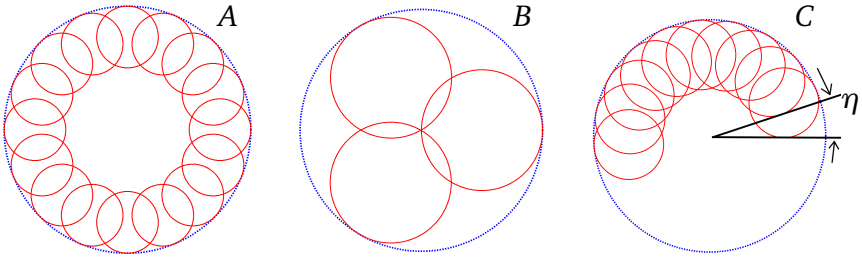

Figure 25: Setups with different coil radii R= r_c/r_0 and number of measurements I. A: I=16, R=0.25; B: I=3, R=0.5; C: I=10, R=0.3, $\eta = \pi/I$.

Different setups in Figures (25) and (26) show the effect of the coil positioning on the condition number of the matrix. These setups are marked in Fig. (24) for $N = 8$ measured harmonics. The better the outer radius of the measurement domain is sampled, the lower will be the condition number of the matrix. As an example, Setup C, covering only half of the measurement domain, yields a condition number of $\kappa = 1859$.

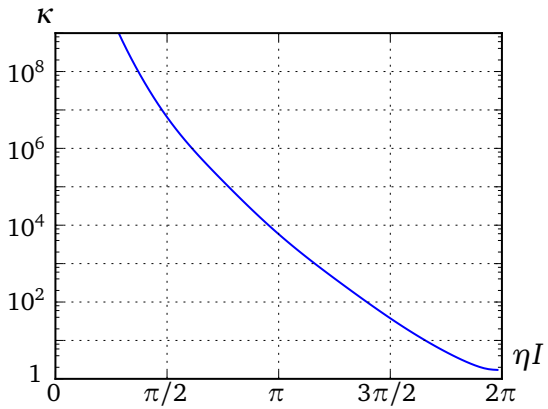

Figure 26: The computed condition number κ of the matrix $[M]$ in Setup C for different angle η.

Fig. (26) shows the condition number subject to the incremental angle η between subsequent measurements. The larger the angle, the better are the measurement positions distributed on the circle. As expected, the condition number becomes better, the more the domain is sampled.

3.6 Effect of the positioning error

The positioning uncertainty on a single measurement, described in Paragraph (2.5.2), affects the combination of measurements. The position of the coil is only known to a certain extent, whereby the unidentified difference introduces an error. Analyzing the error is cumbersome, because of the binomial coefficient and the infinite sum in the corresponding formula, as presented in Eq. (106). An analytic approach with an estimation is presented, however the simulations yield a better comprehension.

Analysis of the error-propagation

The position z_i is altered by a relatively small value Δz. The entries of the matrix for one position z_i, from Eq. (115), are raised by the error term $w_{n,k}^{(\mathrm{err})}$:

$$w_{n,k}^{(i)} + w_{n,k}^{(\mathrm{err})} = \binom{k-1}{k-n}\left(\frac{r_\mathrm{c}}{r_0}\right)^{n-1}\left(\frac{z_i+\Delta z}{r_0}\right)^{k-n} . \tag{117}$$

In order to separate the perturbation, the binomial expansion is applied:

$$w_{n,k}^{(i)} + w_{n,k}^{(\mathrm{err})} = \binom{k-1}{k-n}\left(\frac{r_\mathrm{c}}{r_0}\right)^{n-1}\sum_{\tau=0}^{k-n}\binom{k-n}{\tau}\left(\frac{z_i}{r_0}\right)^{k-n-\tau}\left(\frac{\Delta z}{r_0}\right)^{\tau} . \tag{118}$$

The first item of the sum for $\tau = 0$ yields the unaltered term $(z_i/r_0)^{k-n}$ so that the error term can be separated:

$$w_{n,k}^{(i)} + w_{n,k}^{(\mathrm{err})} = w_{n,k}^{(i)} + \binom{k-1}{k-n}\left(\frac{r_\mathrm{c}}{r_0}\right)^{n-1}\sum_{\tau=1}^{k-n}\binom{k-n}{\tau}\left(\frac{z_i}{r_0}\right)^{k-n-\tau}\left(\frac{\Delta z}{r_0}\right)^{\tau} .$$

These transformations allow to give one equation for the error term:

$$w_{n,k}^{(\mathrm{err})} = \left(\frac{r_\mathrm{c}}{r_0}\right)^{n-1}\binom{k-1}{k-n}\sum_{\tau=1}^{k-n}\binom{k-n}{\tau}\left(\frac{z_i}{r_0}\right)^{k-n-\tau}\left(\frac{\Delta z}{r_0}\right)^{\tau} . \tag{119}$$

Rearranging the items, leads to the final expression:

$$w_{n,k}^{(\mathrm{err})} = \left(\frac{r_\mathrm{c}}{r_0}\right)^{n-1} \left(\frac{z_i}{r_0}\right)^{k-n} \binom{k-1}{k-n} \sum_{\tau=1}^{k-n} \binom{k-n}{\tau} \left(\frac{\Delta z}{z_i}\right)^{\tau} . \tag{120}$$

The term $\Delta z/z_i$ dominates the equation in comparison with the unaltered $w_{n,k}^{(i)}$ and gives the relative error of the positioning to the position itself. The further away the measurement positions are, the less important are positioning errors, as the ratio is very small in this case. In general, $\Delta z/z_i \ll 1$ and the exponentiation by τ makes the value decrease very fast. Therefore, the sum can be approximated by its first item(s), as shown below.

The relative influence of the error term to the correct expression is given by the ratio:

$$\frac{w_{n,k}^{(\mathrm{err})}}{w_{n,k}^{(i)}} = \frac{\left(\frac{r_\mathrm{c}}{r_0}\right)^{n-1} \left(\frac{z_i}{r_0}\right)^{k-n} \binom{k-1}{k-n} \sum_{\tau=1}^{k-n} \binom{k-n}{\tau} \left(\frac{\Delta z}{z_i}\right)^{\tau}}{\left(\frac{r_\mathrm{c}}{r_0}\right)^{n-1} \left(\frac{z_i}{r_0}\right)^{k-n} \binom{k-1}{k-n}} \tag{121}$$

$$= \sum_{\tau=1}^{k-n} \binom{k-n}{\tau} \left(\frac{\Delta z}{z_i}\right)^{\tau} . \tag{122}$$

As the term $\Delta z/z_i$ is small, the sum can be approximated with its first items:

$$\frac{w_{n,k}^{(\mathrm{err})}}{w_{n,k}^{(i)}} \approx (k-n)\,\frac{\Delta z}{z_i} + \binom{k-n}{2} \left(\frac{\Delta z}{z_i}\right)^2 + \binom{k-n}{3} \left(\frac{\Delta z}{z_i}\right)^3 + \ldots \tag{123}$$

The function of the binomial factors is strictly monotonically increasing for a growing value for $k-n$. Thus, the highest possible k in combination with the lowest n gives the maximal relative error $w_{n,k}^{(\mathrm{err})}/w_{n,k}^{(i)}$.

As an example, Fig. (27) shows the error matrix, which contains only the positioning error $w_{n,k}^{(\mathrm{err})}$. The matrix is computed for three positions z_i at 10 mm, 20 mm and 30 mm with a positioning error of 0.1 mm in x- and y-direction for all three positions. All the inner trapezoidal matrices for these positions have their largest value at the top right corner, where k is largest and n smallest. Moreover is the dependency of the position visible: The larger the modulus of the position, the lower is the effect of the error. The upper inner matrix for $z_i = 10$ mm has a maximum of 0.18 of relative error, whereas the central (for

$z_i = 20$ mm) and lower inner matrix have much lower values of 0.1 and 0.06, respectively.

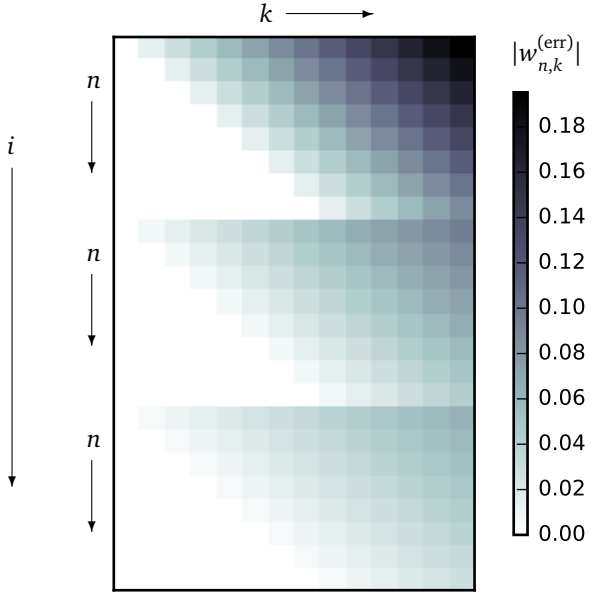

Figure 27: The absolute values of the computed error matrix of the entries $w^{(\mathrm{err})}_{n,k}$.

3.7 Adjustment for quadrupole measurements

The computations do not imply any restrictions for the magnetic field nor the magnet type. With several sets of multipoles another set at a different position can be computed. In the analysis done so far, the first used multipole was the quadrupole component C_2 with $n = 2$. However, the first multipole order can be set to a higher value, what is the subject of this paragraph.

The limits of the variable n are changed to $[3, N]$ so that less information are used from one measurement. To still have more equations than unknowns, the parameters N and I may be changed. The allowed multipoles in a quadrupole are the multipoles C_6 and C_{10}. As a consequence, the values 6 or 10 might be reasonable choices for the parameter N. The limits of the variable k change to $[3, K]$.

These changes lead to slightly altered vectors for C'_n and C_k:

$$\{C'\} = \left(C'_3(z_1),\ C'_4(z_1), \cdots, C'_N(z_1),\ C'_3(z_2), \cdots, C'_N(z_2), \cdots\right)^{\mathrm{T}}, \tag{124}$$

$$\{C\} = \left(C_3,\ C_4, \ldots, C_{\mathrm{K}}\right)^{\mathrm{T}}. \tag{125}$$

The modified matrix $[M]$ has different inner matrices:

$$[W_i] = \begin{pmatrix} w^{(i)}_{3,3} & \cdot & \cdot & \cdot & \cdot & \cdots & w^{(i)}_{3,K} \\ 0 & \cdot & \cdot & \cdot & \cdot & \cdot & \cdots \\ 0 & 0 & \cdot & \cdot & w^{(i)}_{n,k} & \cdot & \cdots \\ \vdots & \vdots & \ddots & \cdot & \cdot & \cdots & \\ 0 & 0 & \cdots & 0 & \cdot & w^{(i)}_{N-1,K-1} & w^{(i)}_{N-1,K} \end{pmatrix}. \tag{126}$$

The rest of the analysis is equivalent, as the equation system is solved in the same way. Moreover is the condition number similar as well as the effect of the positioning error.

It is worth noting that the resulting multipoles start from order $n = 3$ on, the sextupole component. The linear quadrupole component is not part of the solution so that an occurring linearity in the result is expressed by the first components available, the sextupole and octupole. In the analysis of this configuration in the next section, a low precision appears on these multipoles.

4 Error analysis for different setups

The presented technique is applicable to every rotating-coil measurement, where the aperture is larger than the coil diameter. There, measurements can be acquired at a number of positions and can be combined. So far, the method is implicitly presented for the case of a dipole magnet with round aperture. In the following, that case but also other common cases are analyzed. First, a dipole of rectangular aperture with large aspect ratio is studied. Many dipole magnets have such transverse dimensions so that a detailed discussion is useful and needed. Moreover is this problem discussed for many years in the magnetic measurement community. Secondly, a quadrupole with quadratic aperture is analyzed so that the adjustments in the matrix become visible.

In this section, the multipoles are given by a simulation program. The simulated set of field harmonics is used to express the multipoles at the different measurement position. To these *simulated measurements* the errors on the positions and multipoles are added. This completely computational approach allows to run many simulations with different, random errors to estimate the standard deviation of the result. Results of measurements acquired in the measurement laboratory are presented in Chapter (5).

4.1 Dipoles of rectangular aperture with large aspect ratio

The measurement of the field errors in a dipole with a rectangular aperture are difficult, since there is no optimized tool for that purpose. The rotating coil works best for round or quadratic apertures, other measurement devices are usually less precise. With the combination of measurements, the drawback of the inflexibility of the rotating coil has been tackled.

The method is applied to magnets with rectangular aperture such as the calibration dipole magnet [70] of the magnetic measurement section at CERN, which is studied in the following. The magnet has an aperture of 320 mm times 100 mm and a magnetic length of 2500 mm. Even though a tight control of the position is possible, a high uncertainty on the positioning of 0.1 mm to 1 mm is assumed for the following study. As the effect of the positioning error depends on the multipoles, different field homogeneities are assumed for the central part of the magnet and the magnet extremities with the fringe field regions. The assumed noise levels cover the range of what is achievable magnetic measurements using rotating coils.

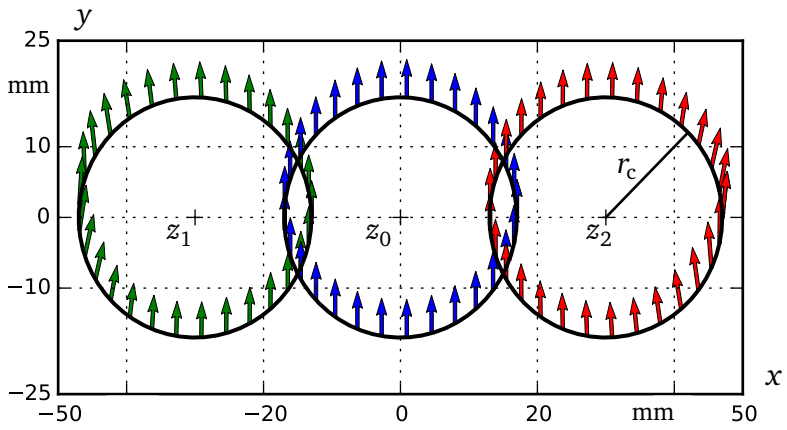

Figure 28: The setup with three measurements in a magnet with large rectangular aperture and the positions z_0, z_1, z_2.

Measurement configuration

The magnet is measured at three longitudinal positions: The two magnet extremities covering the fringe fields up to a point of longitudinal uniformity within the magnet core and the central part of the magnet. Choosing these two cases with the high and low (transverse) field homogeneity will yield an understanding of the error propagation in the post processing of the measurement data. The multipoles in the central part have low values, denoted $c_n^{(\ell)}$ and are given in Table (4), left. The multipoles at the magnet extremities have much higher values, are denoted $c_n^{(h)}$ and given in Table (4), right. The computed values come from a simulation with Opera-3d [71] of the calibration magnet.

The multipoles in the Table (4) are given for the central transverse position at position z_0. The measurement positions are assumed to be $z_1 = -30$ mm, $z_0 = 0$ mm and $z_2 = 30$ mm. The position of the central measurement z_0 equals the position of the reconstructed multipoles. The coil radius r_c is 17 mm.

4.1.1 Error propagation in the field reconstruction

A Python code was written to do the simulations by using the NumPy and SciPy libraries, whereas an older version written in Fortran used the Lapack libraries. The simulations were done with different sources of errors: First, only measurement errors (two levels) and position errors (two levels) are taken into account independently. Finally the two errors sources are combined.

Table 4: Left: The low multipoles $c_n^{(\ell)} = b_n^{(\ell)} + i a_n^{(\ell)}$ at the magnetic center. Right: The high multipoles of the connection side $c_n^{(h)}$. Both at a reference radius of 38 mm. By courtesy of Thomas Zickler, who did the simulations.

n	$b_n^{(\ell)}$	$a_n^{(\ell)}$
1	10 000	0.0
2	-0.0	-0.03
3	-0.35	-0.0
4	-0.03	-0.01
5	-0.07	-0.0
6	-0.01	-0.01
7	-0.05	-0.0
8	-0.0	0.0
9	0.0	0.0
10	0.0	0.0
11	0.01	-0.0
12	-0.0	-0.0
13	-0.0	0.0
14	0.0	0.0
15	0.01	0.0

n	$b_n^{(h)}$	$a_n^{(h)}$
1	10 000	0.0
2	-0.35	1.7
3	64.64	0.01
4	0.17	0.56
5	10.65	0.06
6	0.85	-0.08
7	-1.07	-0.06
8	-0.65	0.35
9	3.32	-0.0
10	-0.02	-0.02
11	-0.14	0.09
12	0.64	0.13
13	0.81	0.03
14	0.17	0.25
15	1.37	0.0

Noise levels

All imposed errors are assumed to be of Gaussian distribution with zero mean. It is assumed that the noise amplitude over the multipole order is similar, with the two values $\sigma_{\mathrm{m}}^{(h)} = 1.0$ and $\sigma_{\mathrm{m}}^{(\ell)} = 0.1$ on the normalized multipoles. These values correspond to an absolute difference of 10^{-4} T and 10^{-5} T, respectively, for a main dipole flux density of 1 T. The positioning error is also assumed to be Gaussian with zero mean and $\sigma_{\mathrm{p}}^{(h)} = 1$ mm and $\sigma_{\mathrm{p}}^{(\ell)} = 0.1$ mm, although higher precisions can be obtained with appropriate alignment stages.

Error norm

As a figure of merit for the field reconstruction, an error norm on the path γ is defined and shown in Fig. (29). The characteristic points are $y \in \{\pm(2/3)\, r_{\mathrm{c}}\}$ and $x \in \{x_1 - (\sqrt{5}/3)r_{\mathrm{c}}, x_2 + (\sqrt{5}/3)r_{\mathrm{c}}\}$, so that the corners of the rectangle lie on the circles. The long sides are sampled 100 times, the short ones 50 times.

The error ξ is defined as the sum over the errors along that path γ divided by the number of samples and normalized to the central field at z_0:

$$\xi := \sum_{i=1}^{300} \frac{|B_{\mathrm{rec}}(\gamma_i) - B_{\mathrm{o}}(\gamma_i)|}{300\,|B_{\mathrm{o}}(z_0)|} \,. \tag{127}$$

This error norm is computed 250 times for the Gaussian input data so that a mean and sample standard deviation can be computed.

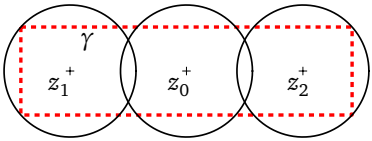

Figure 29: Reconstruction and original field are compared on the dashed path γ.

4.1.2 Results of the combination

A combination without any additional noise gives results that are accurate within machine precision. To analyze the error propagation, in the following the error sources are activated one at a time.

Measurement error only

Each normalized multipole is subject to an additional noise value that comes from a normal distribution with the standard deviation σ_{m}. This value is set to $\sigma_{\mathrm{m}}^{(h)} = 1.0$ and $\sigma_{\mathrm{m}}^{(\ell)} = 0.1$ to study two exemplary cases. To understand the dependency of the multipole values, the high multipoles of the fringe field $c_n^{(h)}$ and the lower ones of the central field $c_n^{(\ell)}$ are used.

Table 5: Mean ± standard deviation of the error sum multiplied by 10000 for 250 computations with different random noise summed up over the path γ for different configurations: $\xi \times 10^4$.

	$\sigma_{\mathrm{m}}^{(\ell)}$	$\sigma_{\mathrm{m}}^{(h)}$
$c_n^{(h)}$	0.254 ± 0.06	2.42 ± 0.57
$c_n^{(l)}$	0.253 ± 0.06	2.47 ± 0.58

Table (5) shows the error ξ, the average of 300 points along the domain boundary defined by the dashed line in Fig. (29). It shows that the error sum grows by a factor 10 for the two different noise levels σ_m. Fig. (31) shows the linear dependency in detail with the growing standard deviation as error bars for the large multipoles $c_n^{(h)}$. For constant noise, the error ξ does not depend on the strength of the multipoles. For the different multipole level, the error does not change significantly, as there is no visible influence for both noise values.

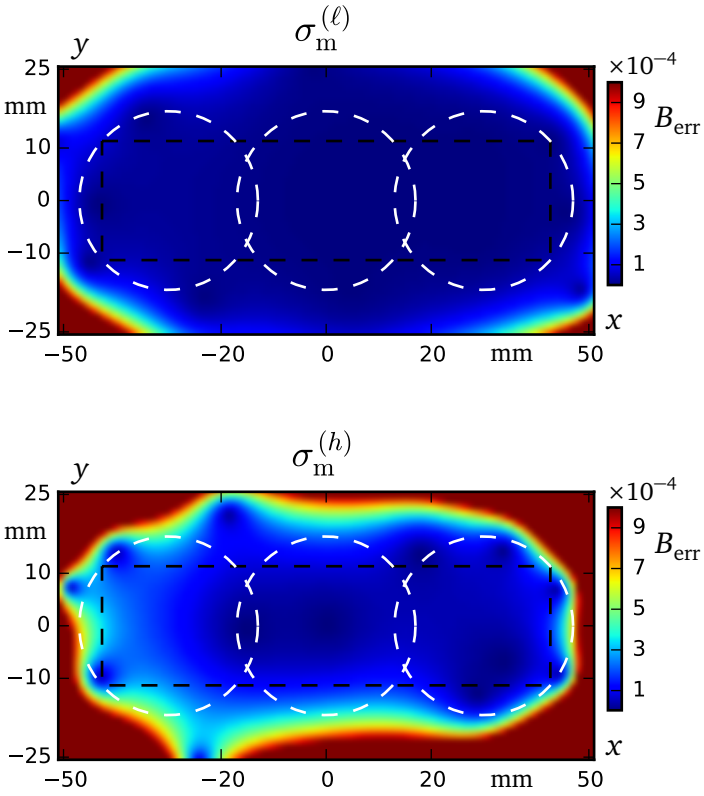

Figure 30: The relative difference of the reconstructed field and the original one to the field in the center $B_\mathrm{err} = |B_\mathrm{rec} - B_\mathrm{o}|/|B_\mathrm{o}(z_0)|$. The graphs are made for the high multipoles $c_n^{(h)}$ with a computed random error. The error sum ξ is 0.27×10^{-4} and 2.51×10^{-4} for $\sigma_\mathrm{m}^{(\ell)}$ and $\sigma_\mathrm{m}^{(h)}$, respectively.

The heat maps in Fig. (30) show the relative difference of the reference field and the reconstructed one to the original field at the central position. The figures are given for the high multipoles $c_n^{(h)}$. The multipole values have either way a minor and invisible influence. As the noise depends on random numbers, the figures change for every run, and the shown ones are chosen to be representative by the author.

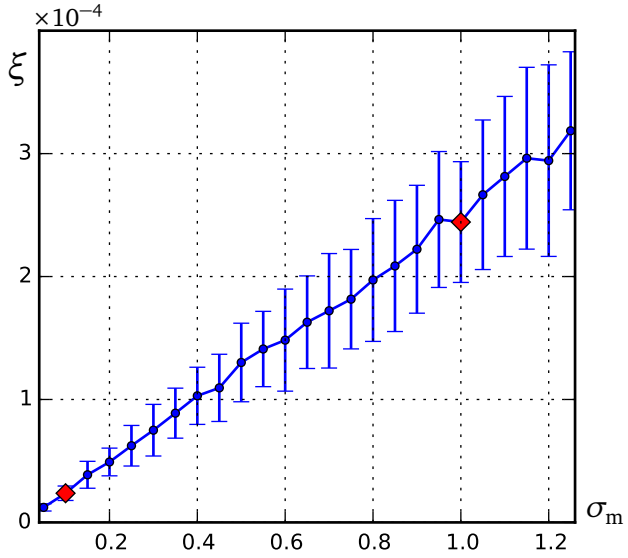

Figure 31: The error ξ as a function of the computed measurement error σ_m for 250 runs. $\sigma_\mathrm{m}^{(\ell)}$ and $\sigma_\mathrm{m}^{(h)}$ are marked with a red rhombus. The graph is shown only for the high multipoles $c_n^{(h)}$, as the low multipoles produce the same results for this scale.

Positioning error only

In this paragraph, the effect of a positioning error is studied by assuming zero noise on the measurements. The positioning error σ_p is set to two exemplary values, which are $\sigma_\mathrm{p}^{(h)} = 1.0$ mm and $\sigma_\mathrm{p}^{(\ell)} = 0.1$ mm. Both values are relatively high and representative for an application in a cryostat or in a difficult measurement environment. Again, both values for the multipoles are used and shown in Table (6).

Table 6: The error sum multiplied by 10000 over the path γ for different configurations: $\xi \times 10^4$.

	$\sigma_{\mathrm{p}}^{(\ell)}$	$\sigma_{\mathrm{p}}^{(h)}$
$c_n^{(h)}$	0.27 ± 0.11	2.79 ± 0.97
$c_n^{(l)}$	0.01 ± 0.01	0.14 ± 0.05

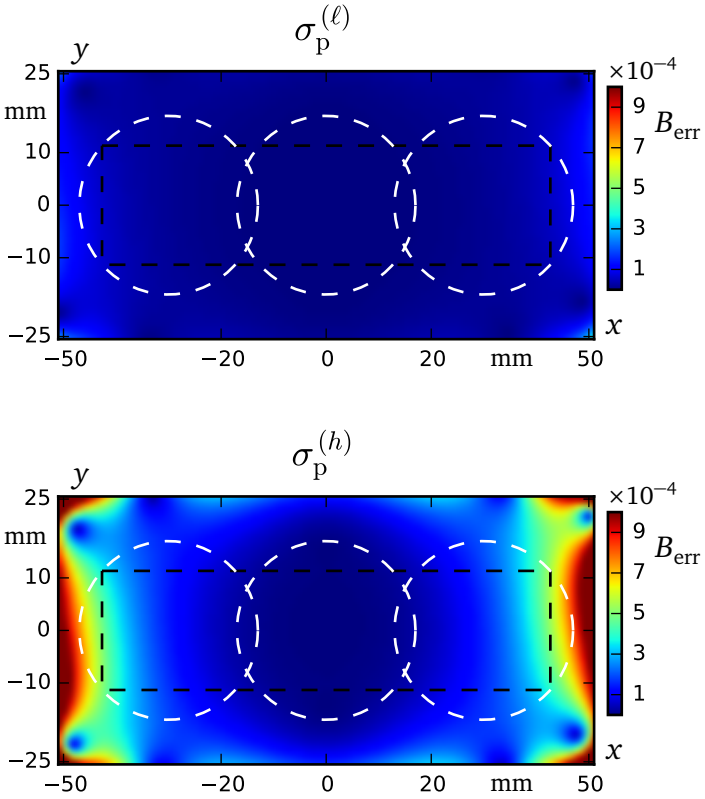

Figure 32: The relative difference of the reconstructed field and the original one to the field in the center $B_{\mathrm{err}} = |B_{\mathrm{rec}} - B_{\mathrm{o}}|/|B_{\mathrm{o}}(z_0)|$ for the high multipoles $c_n^{(h)}$ with computed random error. The positioning error is low $\sigma_{\mathrm{p}}^{(\ell)} = 0.1$ mm and high $\sigma_{\mathrm{p}}^{(h)} = 1.0$ mm.

A significant difference for the two multipole levels is visible: The high multipoles $c_n^{(h)}$ lead to an error sum ξ, which is about 20 times higher than for the low multipoles. This is explained by the dependency on the multipole values in Paragraph (2.5.2): The influence of σ_p grows with the modulus of the multipoles. For both sets of multipoles, the error sum ξ depends linearly on the positioning error σ_p so that the factor 10 is recognizable in the table.

Fig. (32) shows the heat maps of the absolute field difference for a computation using the high multipole values. The influence of the low positioning error $\sigma_\mathrm{p}^{(\ell)} = 0.1$ mm is smaller than 10^{-4} relative to the field in the center and therefore considered to be very small. The high positioning error however, has a larger effect and the field difference can reach, in the area covered by the coils, a maximum of 10×10^{-4} relative to the field in the center. For the simulation with the lower multipoles, the influence is not visible in this scale and the error coming from a bad positioning system is not important.

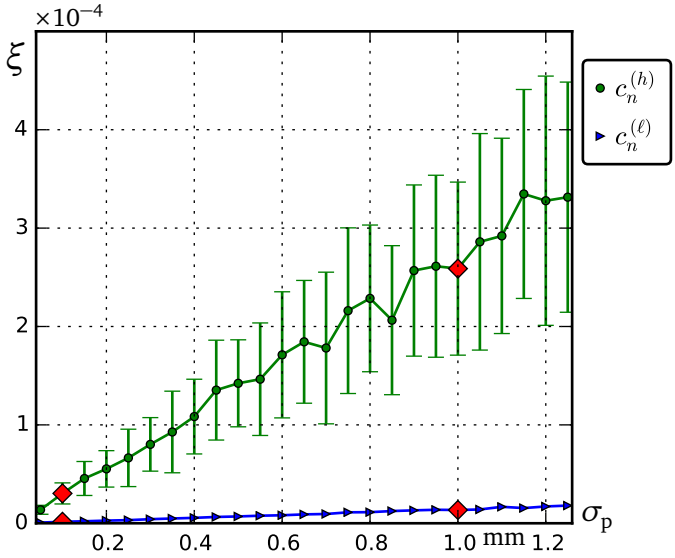

Figure 33: The error sum ξ as a function of the computed positioning error σ_p for 250 runs. The green (upper) graph is made for the high multipole values $c_n^{(h)}$ and the blue one for the low $c_n^{(\ell)}$. The red rhombus mark $\sigma_\mathrm{p}^{(\ell)}$ and $\sigma_\mathrm{p}^{(h)}$.

Both errors combined

Positioning errors and measurement errors were studied separately, however they occur simultaneously in real measurements. In this paragraph the eight possible combinations of the assumed values for the variables c_n, σ_m and σ_p are studied. The Tables (7) shows the error sum ξ for all the eight combinations.

Table 7: The computed error $\xi \times 10^4$ for the low multipoles $c_n^{(\ell)}$ in the left table, and the high multipoles in the right table depending on the different error sources σ_p and σ_m.

$c_n^{(\ell)}$	$\sigma_\mathrm{p}^{(\ell)}$	$\sigma_\mathrm{p}^{(h)}$
$\sigma_\mathrm{m}^{(h)}$	2.49 ± 0.61	2.54 ± 0.65
$\sigma_\mathrm{m}^{(\ell)}$	0.25 ± 0.06	0.29 ± 0.07

$c_n^{(h)}$	$\sigma_\mathrm{p}^{(\ell)}$	$\sigma_\mathrm{p}^{(h)}$
$\sigma_\mathrm{m}^{(h)}$	2.57 ± 0.65	3.94 ± 0.96
$\sigma_\mathrm{m}^{(\ell)}$	0.39 ± 0.1	2.81 ± 1.09

The low multipoles are printed in the left table, where the positioning errors on the top are linked to the measurement errors on the side. The corresponding heat maps in Fig. (34) give the error ξ in the continuous interval in between.

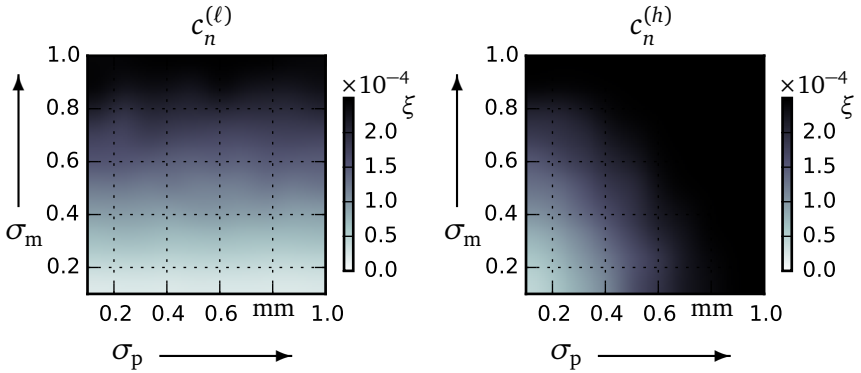

Figure 34: The computed error sum ξ depending on the two error sources for the two sets of multipoles. It expands from 0 (white) to 2.5 (black). On the horizontal axis is the positioning error, on the vertical axis the measurement error. For the high multipoles in the right figure, the positioning error shows an effect.

Depending on the multipoles, the measurement error is dominating the error sum ξ. For the low multipoles, the positioning error has a small effect. Thus,

it is the measurement error, which primarily defines ξ, as the left graph in Fig. (34) shows only very little change by moving right.

For the higher multipoles, in contrast, the effect coming from the positioning error is high enough to have a similar influence as the measurement error. A measurement error of $\sigma_\mathrm{p} = 0.5$ mm has a similar effect as a positioning error $\sigma_\mathrm{m} = 0.5$. There, the combination introduces an error, which is not made by a single measurement.

Improvement of the precision

As explained in Paragraph (2.5.1) and shown in Fig. (16) and (17), the uncertainty of the higher-order multipoles affect the field description. For a single measurement, the noise leads to low precision, especially visible in the noise floor of the higher-order multipoles.

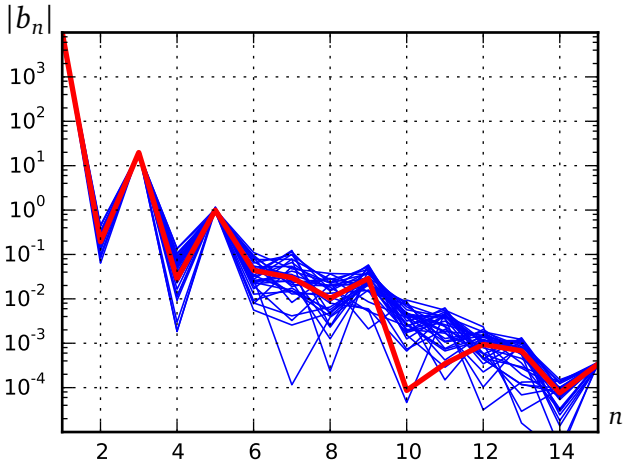

Figure 35: The computed multipoles in red/thick and 30 results of the combination in blue with $\sigma_\mathrm{m} = 0.1$ and $\sigma_\mathrm{p} = 0.1$ mm.

In Fig. (35), the multipoles of 30 combinations, affected by both low error sources $\sigma_\mathrm{m}^{(\ell)}$ and $\sigma_\mathrm{p}^{(\ell)}$, are presented. In comparison to Fig. (16), the noise floor is not visible any more and the multipoles are closer to the original values. Especially, the higher accuracy on the higher-order multipoles makes the field representation valid in a larger domain as seen in the Fig. (30).

The higher precision is shown in Fig. (36), where the sample standard deviation S of the combination and a single measurement are shown. The single measurement in red, affected by a measurement error of $\sigma_{\mathrm{m}}^{(\ell)}$, shows the noise floor for the higher-order field harmonics. Values smaller than 0.1 for the c_{12} for example, can not be distinguished from the measurement noise.

The combination, however, shows a large improvement of the precision by shrinking the standard deviation particularly for the higher-order multipoles. That makes them distinctly visible from the measurement noise. These simulations were done with the low error sources $\sigma_{\mathrm{m}}^{(\ell)}$ and $\sigma_{\mathrm{p}}^{(\ell)}$.

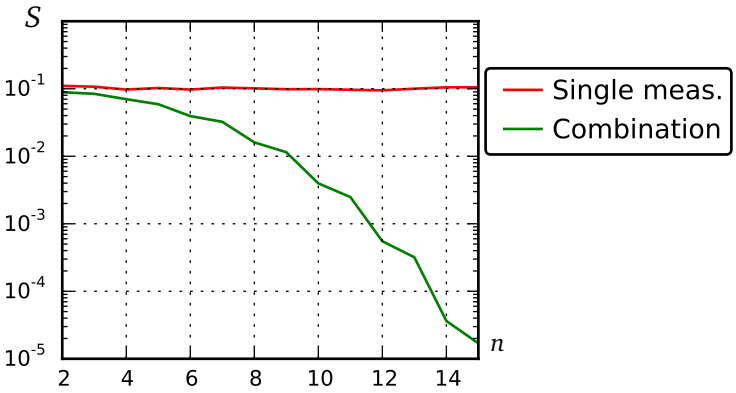

Figure 36: The sample standard deviation S in logarithmic scale for every multipole of 250 computations of the combination in green, and for a single measurement in red.

Conclusion

The combination of the three measurements yields a field reconstruction, which is much more accurate than the field description from a single measurement. The accuracy is not only better in the outer domain, which is not covered by the single measurement, but also within the area covered by the central coil.

The reconstruction is affected by the positioning errors of the single measurements. This error scales with the multipoles present in the magnet and is therefore different for the central part and the fringe fields of a magnet. It has been shown, that the influence from the incorrect positioning is low in the central part with a high field homogeneity. In the fringe fields, the occurring multipoles are larger and the positioning is much more important to the com-

bination. There, a positioning error of 1 mm has to be taken into account for measurement devices that can measure better than 10^{-4} relative to the main field.

Overall, this configuration shows the high functionality of the proposed method when it comes to measurement and positioning errors. The error does not propagate much and the results obtained by the reconstruction have a high precision.

4.2 Quadrupole

Because of the four poles, the aperture of quadrupoles is usually symmetric. An installed beam pipe could limit the access, but in general, the transverse dimensions are the same. Even though, round apertures are also common, a quadratic aperture is chosen for the following analysis.

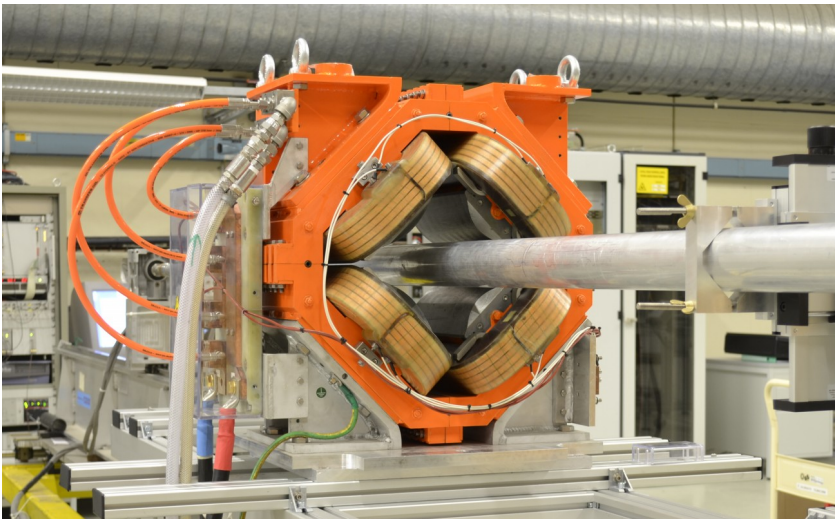

Figure 37: Water-cooled quadrupole for the MedAustron Project [72].

In principle, the combination of measurements works similarly for the quadrupole as for the dipole but with the adjustments of the matrix described in Paragraph (3.7). Using only the precise measurements of the compensated multipoles, the quadrupole and dipole component are avoided. Thus, the multipoles that are reconstructed start from order $n = 3$, the sextupole component.

4.2.1 Measurement configuration

The multipoles are computed on a reference radius $r_0 = 100$ mm using two different configurations. In Setup I, a large coil with a coil radius of $r_c = 50$ mm is used at $I = 4$ positions to measure up to the tenth multipole ($N = 10$). Setup II uses a smaller coil of $r_c = 20$ mm to acquires four multipoles ($N = 6$) at $I = 16$ positions. The measurement positions are in both cases as far out as possible. The assumed aperture limit the positions to the square of a side length of 210 mm. These two configurations compute the multipoles and the field, which are then compared to the original values. The simulated multipoles come from a computation with the ROXIE software package [73] and are listed in Table (8).

Table 8: The multipoles of the simulated quadrupole. The reference frame is not in the magnetic center so that not only the allowed multipoles are present. The reference radius is $r_0 = 100$ mm.

n	b_n	a_n
1	34.0	116.0
2	10000.0	0.0
3	0.01	0.03
4	1.19	0.01
5	0.24	0.84
6	24.0	0.0
7	0.0	0.01
8	0.17	-0.04
9	-0.86	-2.93
10	-50.5	0.0
11	0.0	0.0
12	0.02	0.0
13	0.03	0.11
14	1.4	0.0
15	0.0	0.0

As error sources, the measurement error is set to $\sigma_m = 0.1$ and the positioning error to $\sigma_p = 0.01$ mm $= 10$ μm. That represents a measurement at room temperature with a precise positioning system. Moreover is the measurement equipment assumed to acquire the compensated multipoles with a precision of 10^{-5}, relative to the main field.

Setup I has $I(N-2) = 4 \cdot 8 = 32$ measured information to compute the $K-2 = 13$ multipoles. With a ratio of the radii $r_c/r_0 = 1/2$, this configuration

has a condition number of $\kappa \approx 42$. Setup II has twice as many $16 \cdot 4 = 64$ information for the same number of unknowns. However, the smaller ratio of the radii of 1/5 leads to a condition number of $\kappa \approx 292$.

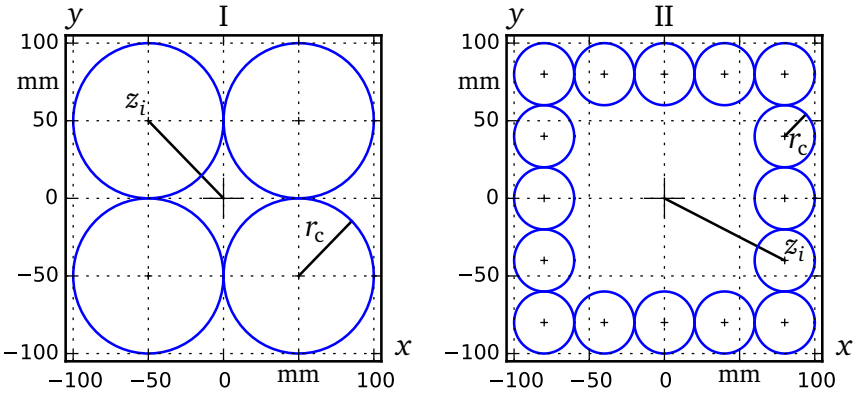

Figure 38: The positions for the two setups and the aperture boundary at $\{x,y\} = \pm 105$ mm. The measurement positions for both setups are placed to sample the domain far outside.

Both configurations have the measurement positions placed along a rectangle. As the reference radius defines a circle, some of the measurement positions are outside the reference radius. Therefore, the domain sampled by the measurements is larger than the domain defined by the reference radius of the reconstructed multipoles.

4.2.2 Results of the combination

With the relative low amplitude of both error sources, a high accuracy on the field can be expected. The Figures (39) and (40) show the relative error of the reconstructed field and the original one normalized to the original field in the center: $B_{\mathrm{err}} = |B_{\mathrm{rec}} - B_{\mathrm{o}}|/|B_{\mathrm{o}}(0)|$. The maximal error shown equals $2.2 \cdot 10^{-4}$ and is much lower than in the previous examples in the former paragraph.

Fig. (39) shows very small errors ($< 10^{-4}$) in the areas that are sampled by the measurement coil. Within the reference radius, but outside the domain covered by a measurement, the error could grow slightly higher to almost $2 \cdot 10^{-4}$. Further inside the reference radius at about $0.75\, r_0$, the error is smaller than 10^{-5}.

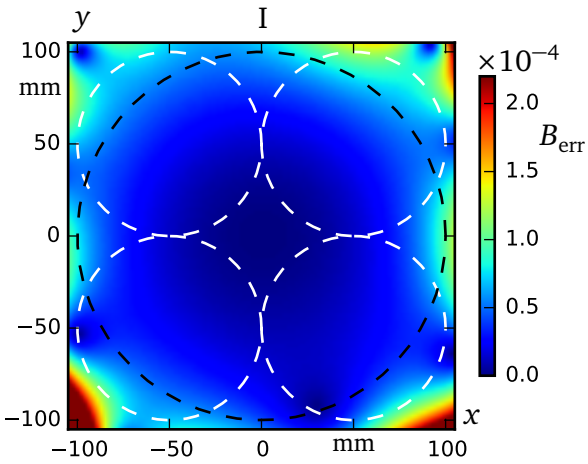

Figure 39: Computations of Setup I with $I = 4$ measurement positions only but with $N = 10$ as the highest multipole order. Shown is the relative error $B_{\text{err}} = |B_{\text{rec}} - B_{\text{o}}|/|B_{\text{o}}(0)|$ of the original field B_{o} and the reconstructed field B_{rec}.

Setup II in Fig. (40) shows a relatively good reconstruction inside the reference radius with an error smaller than 1.5×10^{-4}. The domain sampled by the measurement coil is not free of large errors. The corners of the aperture are covered by a measurement, but have relative high errors.

The comparison of the two figures illustrate the behavior of the two configurations. While Setup I covers a larger area with each measurement, Setup II reconstruct the field by many small contributions. As a consequence have the single measurements a relatively smaller effect on the overall reconstruction, such that the field can differ inside the sampled domain.

Presenting the normal components of the multipoles in Fig. (41), the different behavior of the two configurations is not distinctly visible. As the results are very similar inside the reference radius, the multipoles are also similar. On the allowed multipoles b_6, b_{10} and b_{14} the logarithmic plot shows little differences. For multipoles with smaller values, a difference is apparent. This is especially for the lower orders $n \in \{3,4\}$ the case. That negative effect comes from the absence of the quadrupole component in the matrix inversion. The fit excludes the linear component and is therefore less flexible so that the linear effect is represented by the other multipoles. Besides a possible modification of the matrix, these lower-order multipoles can be extracted from a central measurement. In

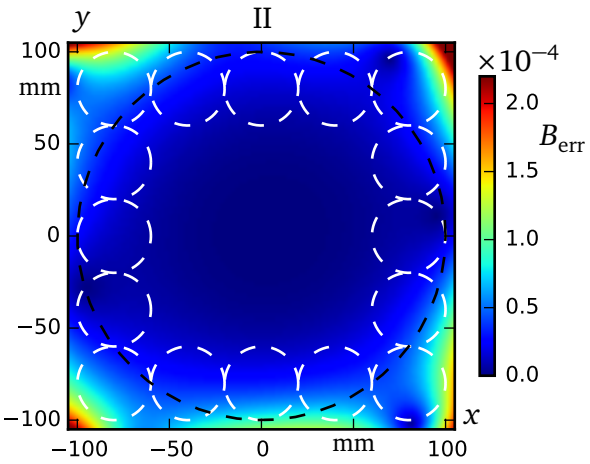

Figure 40: Computations of Setup II with $I = 16$ measurement positions and $N = 6$ as the highest multipole order. Shown is the relative error $B_{\text{err}} = |B_{\text{rec}} - B_{\text{o}}|/|B_{\text{o}}(0)|$ of the original field B_{o} and the reconstructed field B_{rec}.

measurement practice, a central data acquisition is anyway necessary for the alignment and can be used to compare and to correct theses multipoles.

The Fig. (42) shows the sample standard deviation of the results of both configurations. It is computed for 250 runs with different random noise on the multipoles and the position. It shows in both cases an exponential decay over the multipole order n. For the higher-order multipoles the standard deviation is small (< 0.3), whereas the precision is high. The sextupole component C_3 shows a very low precision of 0.33 and 0.7 for Setup I and II, respectively.

4.3 Conclusion

Dipoles and quadrupoles can be measured by combining several measurements. Shown in the Paragraphs (4.1) and (4.2), the method is applied to a dipole and a quadrupole with rectangular aperture. The reconstruction for the dipole uses three measurements on a straight line, whereas the combination leads to a field representation, which is accurate in the sampled domain. The imposed errors for the measured multipoles and the position propagate only to a limited extent, which are in the same range as a single measurement. The precision of the resulting multipoles increases with the multipole order, whereas the improvement is less distinct than in the dipole measurement of the former paragraph.

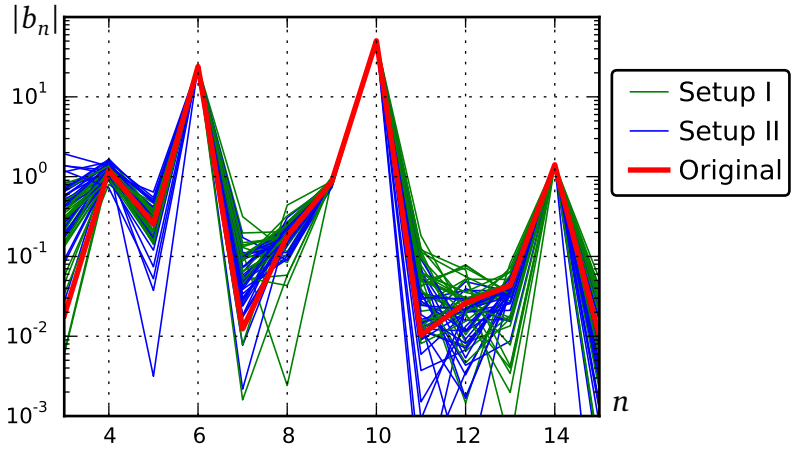

Figure 41: Computation of the normal components of the original field in red and 30 results of the combination in green for Setup I and in blue for Setup II in logarithmic scale.

Using the combination of measurements, increase the precision of the field representation, but also gives an applicable technique to measure magnets of rectangular aperture with large aspect ratio. Doing so, a closed-form formula with the common multipole representation can be computed. This simplifies the work with the magnetic field and also gives a better understanding of the overall multipoles in the accelerator.

The combination of measurements in a quadrupole magnet are more sophisticated. The main field component is not constant as in a dipole, but grows linearly with radial distance to the origin. That makes the fitting more difficult and leads to higher errors in the lower-order multipoles C_3 and C_4. This drawback can be overcome by an additional measurement in the central position, which is in measurement practice needed anyway. Nevertheless yields the method for the studied configurations good results. Regardless of weather a large coil of $r_c/r_0 = 1/2$ or a small coil of $r_c/r_0 = 1/5$ is used, the field reconstruction is accurate in the range of 10^{-4}. Moreover are the meaningful multipoles of order 6, 10 and 14 computed with high precision.

The example of the quadrupole proved the point, that many available rotating coils can be used for the required measurement. The data acquisition and the quality of the reconstruction does not depend on the device that is used. It is much more important to use the coil correctly and set the parameters in the

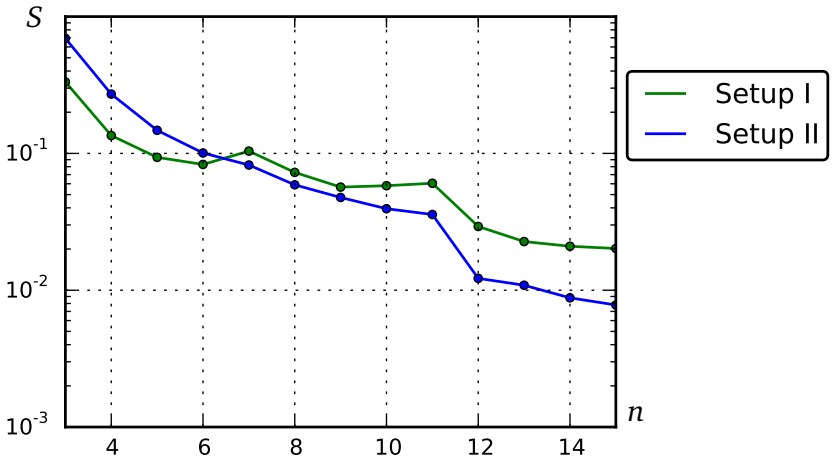

Figure 42: Sample standard deviation of the computed multipoles after 250 runs for both, Setup I and II.

right way to have a good outcome of the combination. To have that flexibility, a measurement laboratory needs different coils that are calibrated correctly and which give accurate results within the measurement uncertainty.

5 Measurement procedure

Analytic calculations and simulations proved the feasibility of the presented method. The error propagation is analyzed and shows for the assumed noise distribution a good functionality. To show that the combination of measurements works not only in theory, measurements in the CERN magnetic measurement laboratory were acquired. The data acquisition was subject to noise, that might be different from the assumed noise distribution in Chapter (4). Moreover occurred practical problems that were difficult to predict or to model.

As seen in the following paragraph, it is very difficult to create a reference. Since all measurement devices come with uncertainties, it is impossible to measure the absolute correct value for a multipole. Due to that, a comparison of two measurements is needed, even though it is difficult to explain the differences of their results. A cross-check with another measurement device is not useful, as the uncertainties on the acquired data are usually much higher. The best approach to overcome or reduce this problem, is a measurement with a larger rotating coil that covers the complete domain. Further practical explanations follow in the next paragraph.

5.1 Dipole with round aperture

As an experimental validation of the proposed method, a round, large-aperture dipole magnet was measured with two rotating coils of different sizes. The aperture of the dipole is 129 mm in diameter and the magnetic length is 250 mm. The radii of the measurement coils are 45 mm and 30 mm, respectively. Their length is 1.197 m so that they cover the complete magnetic field in longitudinal direction. At eight positions the small coil was used to measure eight harmonics from C_2' to C_9'. The precision of the alignment stages for the positioning was better than 0.1 mm. Fig. (1) shows the setup for the small shaft mounted.

The large coil covers almost the entire aperture and is used as a reference. Even though that coil does not yield perfectly acquired multipoles neither, it should represent the field in a larger area with higher accuracy. The small coil acquires the field at eight off-centered positions within the radius of the large coil. Fig. (43) shows the positions and radii.

The domain is highly over-sampled by the small coil. With eight multipole used from the eight measurements, 64 information are acquired. As $K = 15$ multipoles are computed, the equation system is over-determined. Furthermore holds this configuration a well-determined matrix with a condition number of $\kappa = 6.2$.

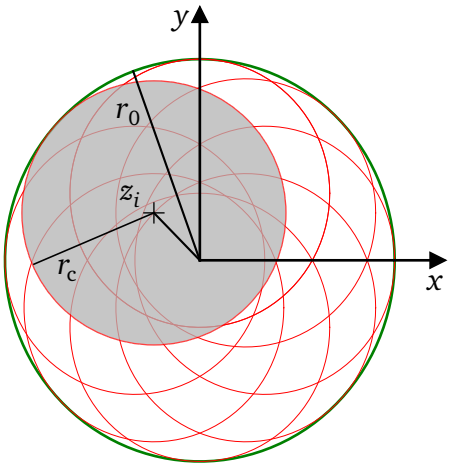

Figure 43: Configuration for the measurement at eight equiangular position with the small coil, marked in red. At the large green circle, the large coil measures the reference multipoles.

5.1.1 Fitting the measurement angle

The measurement bench in the CERN magnetic measurement laboratory, which was used for the data acquisition, does not have a gravitational sensor to measure the initial (starting) angle of the coil.

Figure 44: Overlapping area of two measurements in black. The positions, where the fields is compared, are marked with white crosses.

With the normalization from Paragraph (2.6.3), the phase of the multipoles is shifted such that the skew term of the main component is zero. This common practice makes the use of an gravity sensor [74] needless for a simple measurement, wherefore a workaround is needed to use the multipoles with the presented method. The method, in fact, relies on the angle of the multipoles.

Between two measurements, the shaft and the coil are moved to the next position. The coil is, however, not rotated. Thus, the starting angle of the measurement stays the same for the entire measurement procedure. A rotation of the angle α changes the multipoles as follows:

$$\tilde{C_n}(r_c,z_i) = C_n(r_c,z_i)\,\mathrm{e}^{\mathrm{i}n\alpha}\ . \tag{128}$$

Now, the problem is to find the angle α, which is constant for all measured multipoles.

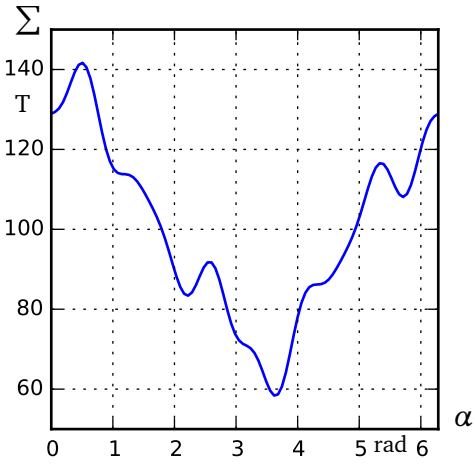

Figure 45: The sum $\sum$ of the difference of the measured magnetic field at the 80 positions for different angles α. The minimum at $\alpha = 3.62$ holds the starting angle of the rotating coil.

Using the overlapping areas, is one possibility to estimate the angle. There, the magnetic field of both sets of measurements have to agree. Fig. (44) shows the overlapping area of two sequential measurements and ten positions, where the magnetic field is compared. Having eight overlapping areas, the field from two sequential measurements can be compared at 80 positions. Doing so by

changing the angle α, the sum of the modulus of the differences yields a distinct minimum.

Fig. (45) shows this error norm over the angle α for this measurement process. The scale of the ordinate depends on the number of points that are compared and the number of overlapping areas. The computed angle can be used to correct the measured multipoles. Applying the rotation, the multipoles are relative to each other in the right direction so that they are usable for the method.

A slightly different method avoids the magnetic field and compares multipoles computed by the feed-down formula. At the same positions, the multipole C_2 for example, can be computed from the multipoles of both sides. Their absolute difference can then be summed up and compared as before. The results are similar, but the underlying technique does not depend on the main field component and is therefore more precise.

5.1.2 Results

The large coil with the coil radius $r_0 = 45$ mm has the internal name R45 and the results of that measurement are linked to that name. R30 is the name of the small shaft, which acquired the data for the combination of measurements. The Figures (46) and (47) show the comparison of the normal and skew multipoles of the single measurement of the R45 (blue) and the combination (red). The bar charts give the multipoles in linear scale, whereas the graphs feature the small differences in logarithmic scale.

The results are quite in agreement, particularly for the normal components b_n. There, the difference is very small and seem to be in the normal range of the uncertainty of a rotating-coil measurement. The skew terms, however, show a larger relative difference on the multipoles a_3 and a_5. The error of 3 units, which corresponds to 3×10^{-4} relative to the main field, is large and has to be discussed.

A possible reason for the error, is the use of different coils. Being subject to different mechanical errors, both coils acquire different data. Even with a good calibration and caution throughout the measurement process, little errors are unavoidable. In this case, the comparison of the two coils show differences that cause the error in the combination. In fact, the error is not in the method but rather in the corrupt input data. Fig. (48) shows the comparison of the two shafts. At the central position, the multipoles are measured and expressed at the large reference radius $r_0 = 45$ mm. Here too, a large difference in the multipoles a_3 and a_5 is visible.

The method depends on the accuracy of the measurement coil to yield accurate multipoles. Only if the measurements of the small coil are good, the results of the combination can be accurate.

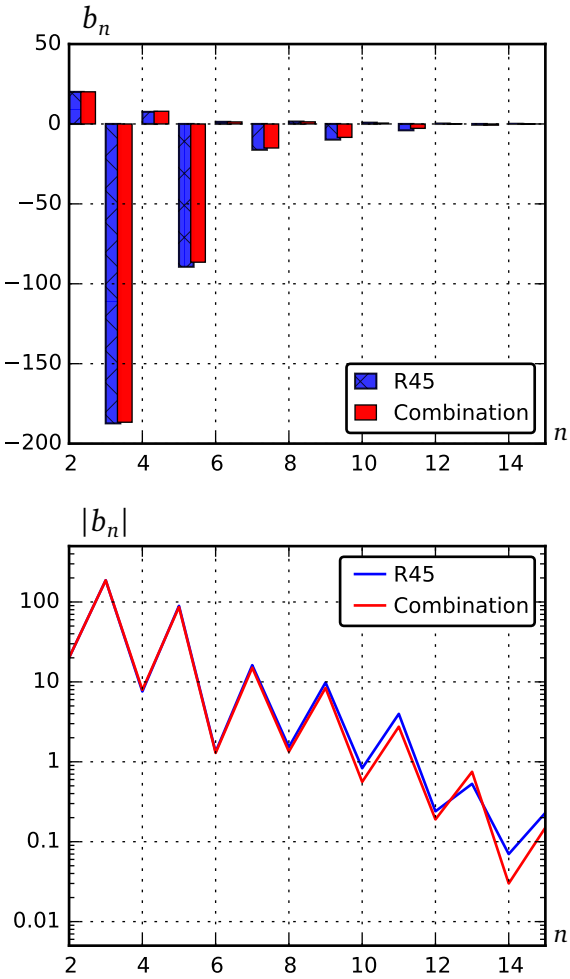

Figure 46: The normal components b_n in linear and logarithmic scale. In blue, with pattern, are the multipoles from the single measurement with the large coil R45. The combination of the eight measurements with the small coil R30 is shown in red.

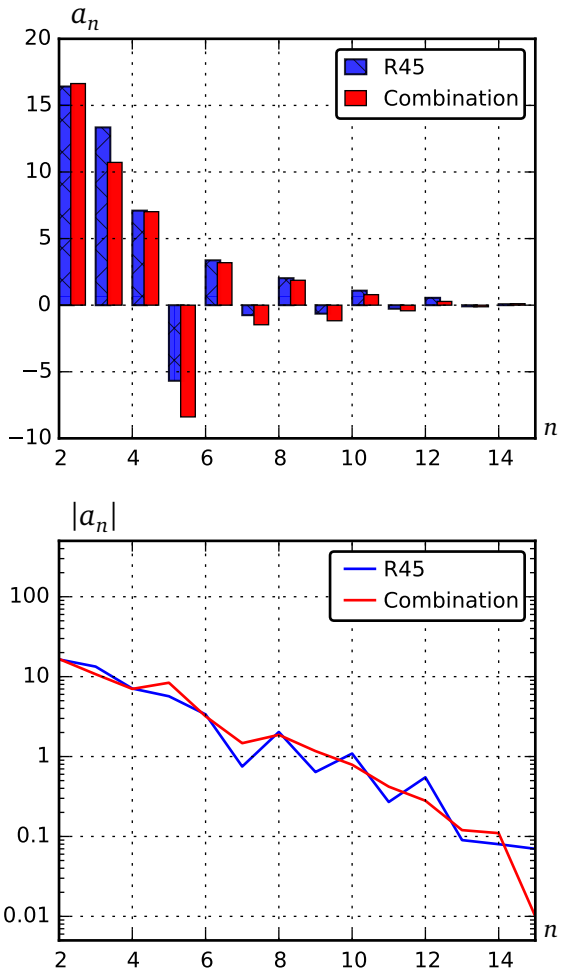

Figure 47: The skew components a_n in linear and logarithmic scale. In blue the R45 measurement, in red the combination. The multipoles a_3 and a_5 show a distinct difference.

Improvement of precision

The precision of the combination is very high, even though the sensitivity of the used coil (R30) is lower than the large reference coil R45. In Table (9), the sample standard deviation is shown for several measurements of the R45 and R30. The repeatability of the combination was tested by using ten different measurements at each position. These measurements were combined one by one without permutations such that one combination based on eight measurements could be compared to one central measurement. The very low (< 0.01) standard deviation is independent of the multipole order and yields a precision higher than for a single measurement. Multipoles at the blind eye of the measurement coil ($n = 11$ for both shafts), can be determined with two orders of magnitude more precisely. This improvement of precision makes the measured data distinguishable from noise. In contrast, the measurement of the b_{12} with the R45 coil gives a value that is four times smaller than its standard deviation. A specification of that quantity is with a single measurement difficult if not impossible.

Table 9: Sample standard deviation S of the normal multipoles b_n at $r_0 = 45$ mm computed on ten measurements with the large (R45, $r_c = 45$ mm) and small (R30, $r_c = 30$ mm) shaft, and the result of the combination from ten measurements at eight positions.

	R45	R45	R30	Combi
n	b_n (units)	$S(b_n)$	$S(b_n)$	$S(b_n)$
2	20.115	0.014	0.014	0.005
3	-186.632	0.013	0.017	0.003
4	7.953	0.007	0.057	0.004
5	-86.501	0.009	0.062	0.005
6	1.293	0.015	0.081	0.005
7	-15.028	0.014	0.232	0.009
8	1.329	0.021	0.102	0.007
9	-8.396	0.033	0.213	0.005
10	0.555	0.136	0.435	0.003
11	-2.748	0.240	2.757	0.005
12	0.195	0.827	7.196	0.004
13	-0.763	0.158	9.167	0.005
14	0.028	0.058	5.179	0.003
15	-0.149	0.073	2.856	0.002

The combination of measurements relies only on the precise data of one measurement. It does not use the multipoles around the blind eye and therefore avoids the noisy data. The use of precise information only, propagates to the resulting multipoles.

5.1.3 Conclusion

The realized measurement procedure gives an insight into the applicability but also into the difficulties of the combination of measurements. The method works and gives plausible results. By using a limited number of multipoles at eight off-centered positions, the multipoles in the reference frame of the magnet are computed. The results are better than a single measurement, because of the high uncertainty on the higher-order multipoles of a measurement at one position. There, the precision is very low and the choice of one value is difficult to make.

The combination of several measurements, however, uses only the precisely measured multipoles and computes the higher-order multipoles in the reference frame from these precise information. Doing so, the uncertainty is low throughout the calculations such that no error is introduced. This improvement of the precision can be seen by the very low sample standard deviation, which is up to 200 times smaller than for a single measurement with a larger coil.

The problem of the unknown encoder angle of a measurement needs a little workaround. Using the overlapping areas of consecutive measurements, allows to fit the unknown angle, which is equal for all the measurements. This can be done by the magnetic field, which has to be identical in the complete overlapping domain. Choosing several points for comparison, yields a distinct minimum for the difference by changing the angle of the measurements. Additionally, it is possible to use the comparison of a certain multipole at this position to avoid the use of the main field component.

In the absence of a good cross-check system, there is no way to prove the accuracy of the method by measurements. The comparison with a different coil introduces a new source of error, which is difficult to estimate. Different coils have different mechanical uncertainties and give different results. For the combination, that means that a systematic error leads to a wrong computation. The results strongly depend on the quality of the measurement coil.

The data acquisition takes at least I times longer than for a single measurement. Additionally, every position has to be set up before the measurement is started. This time is, however, still short compared to the time to set up of the measurement bench and the acquisition system. Nevertheless could an automatized system help to simplify the measurement procedure.

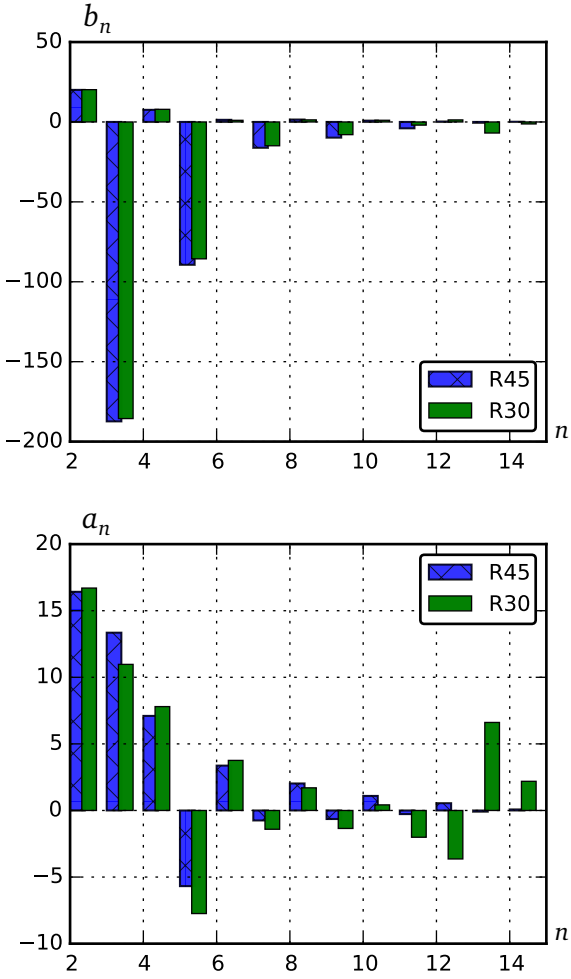

Figure 48: Comparison of the measured multipoles of the two coils R45 and R30. The measurement position is in the center of the magnet and both sets of multipoles are expressed at the reference radius $r_0 = 45$ mm.

6 Adapted coil design

The method of combining multipole measurements is presented in the former chapters with a certain choice of parameters. The configuration had a limit N that is the maximal multipole order. Up to this order, all multipoles were used starting from the first compensated harmonic which is the quadrupole component C_2 in a dipole measurement and the sextupole component C_3 in a quadrupole measurement.

As stated before, the combination yields the link between a measured multipole and the multipoles to reconstruct. For the choice, which multipoles are used, there are no restrictions. In this section, another configuration is presented that needs a different measurement setup. Nominally, it needs an adapted compensation scheme that is presented in the following.

6.1 Sensitivity for two tangential coils

Two or more coils on one rotating shaft are very common, where several layouts are discussed in the Paragraph (2.4.2). In this paragraph, the configuration of two tangential coils on one shaft is detailed. The sensitivity factors for the tangential coil are used such that the resulting flux can be computed. Fig. (49) shows the two coils rotated by 180°.

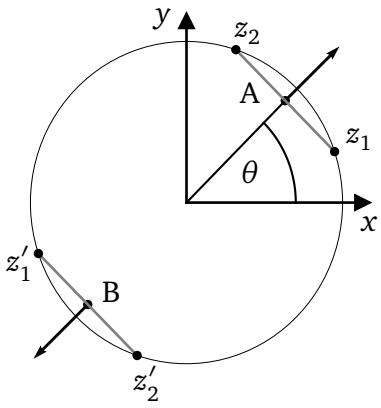

Figure 49: The angle θ and the positions z_1, z_2, z_1', z_2' for a shaft with two tangential coils.

The sensitivity factors of Coil A are given by Eq. (21):

$$K_n^{(\mathrm{A})} = \frac{2\mathrm{i}N_\mathrm{t}L}{n} r_\mathrm{c}^n \sin\frac{n\delta}{2} \,. \tag{129}$$

For Coil B, the positions z_1' and z_2' are mirror-symmetric such that the sensitivity factor for that coil is:

$$K_n^{(\mathrm{B})} = \frac{2\mathrm{i}N_\mathrm{t}L}{n} (-r_\mathrm{c})^n \sin\frac{n\delta}{2} \tag{130}$$

$$= (-1)^n K_n^{(\mathrm{A})} \,. \tag{131}$$

Connecting the two coil in series, adds up their intercepted fluxes. According to Eq. (16), the resulting flux is:

$$\Phi_\mathrm{m}^{(\mathrm{A+B})} = \Phi_\mathrm{m}^{(\mathrm{A})} + \Phi_\mathrm{m}^{(\mathrm{B})} \tag{132}$$

$$= -\mathrm{Re}\left\{\sum_{n=1}^{\infty} \frac{C_n}{r_0^{n-1}} K_n^{(\mathrm{A})} \mathrm{e}^{\mathrm{i}n\theta}\right\} - \mathrm{Re}\left\{\sum_{n=1}^{\infty} \frac{C_n}{r_0^{n-1}} K_n^{(\mathrm{B})} \mathrm{e}^{\mathrm{i}n\theta}\right\} \tag{133}$$

$$= -\mathrm{Re}\left\{\sum_{n=1}^{\infty} \frac{C_n}{r_0^{n-1}} \left(K_n^{(\mathrm{A})} + K_n^{(\mathrm{B})}\right) \mathrm{e}^{\mathrm{i}n\theta}\right\} \tag{134}$$

$$= -\mathrm{Re}\left\{\sum_{n=1}^{\infty} \frac{C_n}{r_0^{n-1}} \left(K_n^{(\mathrm{A})} + (-1)^n K_n^{(\mathrm{A})} \mathrm{e}^{\mathrm{i}n\theta}\right)\right\} \tag{135}$$

$$= -\mathrm{Re}\left\{\sum_{n=1}^{\infty} \frac{C_n}{r_0^{n-1}} K_n^{(\mathrm{A})} \left(1 + (-1)^n\right) \mathrm{e}^{\mathrm{i}n\theta}\right\} \,. \tag{136}$$

The factor $(1 + (-1)^n)$ is zero for the odd n and two for the even n. Therefore, the sum of the fluxes reads as:

$$\Phi_\mathrm{m}^{(\mathrm{A+B})} = -\mathrm{Re}\left\{\sum_{n=2,4,6}^{\infty} \frac{2C_n}{r_0^{n-1}} K_n^{(\mathrm{A})} \mathrm{e}^{\mathrm{i}n\theta}\right\} \,. \tag{137}$$

Inserting the sensitivity factor $K_n^{(\mathrm{A})}$ of Eq. (129), the flux is:

$$\Phi_{\mathrm{m}}^{(\mathrm{A+B})} = -\mathrm{Re}\left\{ 4\mathrm{i}\, N_{\mathrm{t}} L r_0 \sum_{n=2,4,6}^{\infty} \frac{C_n}{n} \left(\frac{r_{\mathrm{c}}}{r_0}\right)^n \sin\frac{n\delta}{2}\, \mathrm{e}^{\mathrm{i}n\theta} \right\} . \tag{138}$$

The flux $\Phi_{\mathrm{m}}^{(\mathrm{A+B})}$ is twice as large than for a single tangential coil and consist of the odd multipole components only. In a dipole magnet, this configuration compensates the main field component and has therefore the highest precision on the higher-order multipoles.

That no odd multipoles are measured with this scheme, makes the use in a dipole counter-intuitive. A dipole has the odd components as allowed multipoles, which are usually more significant. However, with the combination of measurements, the measurement positions are largely displaced of the magnetic center such that both, odd and even, multipoles occur. The odd multipoles in the central position are then computed from the measured field harmonics.

6.2 Handling even multipoles only

The method links a measured multipole to all the higher orders in the reference frame. Using Eq. (106) for the even multipoles, leads to an equation system, that is similar to the one in Paragraph (3.2.1). With the same $w_{2n,k}^{(i)}$ as in Eq. (108), the system reads as:

$$\begin{aligned}
C_2'(r_{\mathrm{c}},z_1) = \quad & w_{2,2}^{(1)} C_2(r_0,z_0) + w_{2,3}^{(1)} C_3(r_0,z_0) + w_{2,4}^{(1)} C_4(r_0,z_0) + \ldots + w_{2,K}^{(1)} C_K(r_0,z_0) \\
C_4'(r_{\mathrm{c}},z_1) = \quad & C_4(r_0,z_0) + w_{4,5}^{(1)} C_5(r_0,z_0) + \ldots + w_{4,K}^{(1)} C_K(r_0,z_0) \\
C_6'(r_{\mathrm{c}},z_1) = \quad & C_6(r_0,z_0) + w_{6,7}^{(1)} C_7(r_0,z_0) + \ldots + w_{6,K}^{(1)} C_K(r_0,z_0) \\
\vdots \quad & \qquad\qquad\qquad\

The right side still includes all the reconstructed multipoles, so that a the entire set of multipoles can be computed. The left side, however, includes the even multipoles only. The corresponding matrix changes accordingly:

$$[W_i] = \begin{pmatrix} w_{2,2}^{(i)} & w_{2,3}^{(i)} & w_{2,4}^{(i)} & \cdot & \cdot & \cdots & \cdot & \cdots & w_{2,K}^{(i)} \\ 0 & 0 & w_{4,4}^{(i)} & w_{4,5}^{(i)} & \cdot & \cdots & \cdot & \cdots & w_{4,K}^{(i)} \\ 0 & 0 & 0 & 0 & w_{6,6}^{(i)} & \cdots & \cdot & \cdots & w_{6,K}^{(i)} \\ \cdot & \cdot & \cdot & \cdot & \cdot & \cdots & w_{2n,k}^{(i)} & \cdots & \cdot \\ \vdots & \vdots & \cdot & \cdot & \cdot & \cdots & \cdot & \cdots & \vdots \\ 0 & 0 & \cdots & 0 & \cdot & \cdots & 0 & w_{N,K-1}^{(i)} & w_{N,K}^{(i)} \end{pmatrix}. \quad (140)$$

The vector for the measured multipoles changes as well:

$$\{C'\} = \left(C_2'(z_1),\ C_4'(z_1),\ C_6'(z_1), \cdots, C_N'(z_1),\ C_2'(z_2), \cdots, C_N'(z_2), \cdots \right)^{\mathrm{T}}, \quad (141)$$

$$\{C\} = \left(C_2,\ C_3, \ldots, C_{\mathrm{K}} \right)^{\mathrm{T}}. \quad (142)$$

With these adjustments, the method can be used as for the other examples. The limit N for the maximal order of the multipoles from measurements has to be even. The number of known quantities in the equation system is: $I \times N/2$. As the limit N is similar to the former configurations, the acquired information per position is lower.

A coil built for this configuration should be small with a small coil radius. The opening angle should be large, so that the sensitivity on the six to eight first multipoles is high.

As an extreme example, a measurement of the quadrupole component only ($N = 2$), can be sufficient to reconstruct the field. There, the number of measurement positions I has to be high to acquire enough information.

6.3 Simulation of the dipole measurement

In Paragraph (5.1), the measurement of the dipole with a round aperture is presented. These multipoles are used in a simulation to create the field for the following analysis. The values of the multipoles can be found in the Figures (46) and (47). As the shown multipoles are normalized, the dipole component is $c_1 = 10000$.

Table (9) shows the normal components with a higher resolution. The differences of the original field to the reconstructed one are discussed, the exact multipole values are of minor importance. It is, however, worth noting that the sextupole component has a very high absolute value of $b_3 \approx -187$.

In both cases, the measurement coil of this section is used: The flux is the sum of two tangential coils, whereby only the even multipoles are acquired. The measurement coil is assumed to be very small with a coil radius of $r_c = 5$ mm with respect to the reference radius of $r_0 = 45$ mm.

6.3.1 Measuring at 16 positions

Acquiring only the even multipoles, reduces the number of information per position. Therefore, the number of measurement positions must be high. For the used setting in this paragraph, $I = 16$ positions are chosen by equiangular distance. Moreover is the radial distance for all measurements $r_0 - r_c$. The highest multipole used from the measurement is $N = 6$ so that the multipoles c_2, c_4 and c_6 are chosen. This configuration results in $I \times N/2 = 48$ information as known quantities in the equation system. The multipoles of order 2 to $K = 15$ are computed so that the equation system is adequately over-determined.

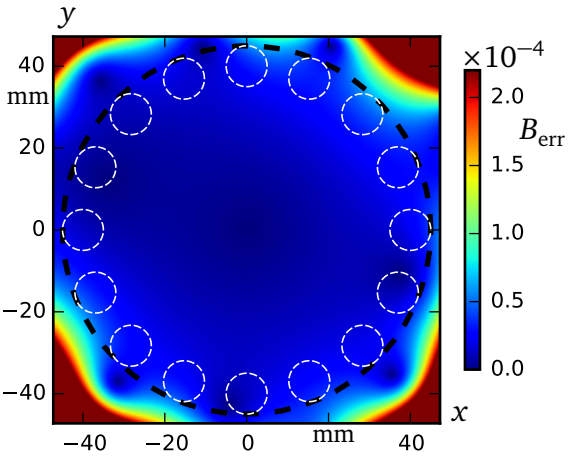

Figure 50: Computation of the relative error $B_{err} = |B_{rec} - B_o|/|B_o(0)|$ of the original field B_o and the reconstructed field B_{rec} with $\sigma_m = 0.1$ and $\sigma_p = 0.01$ mm.

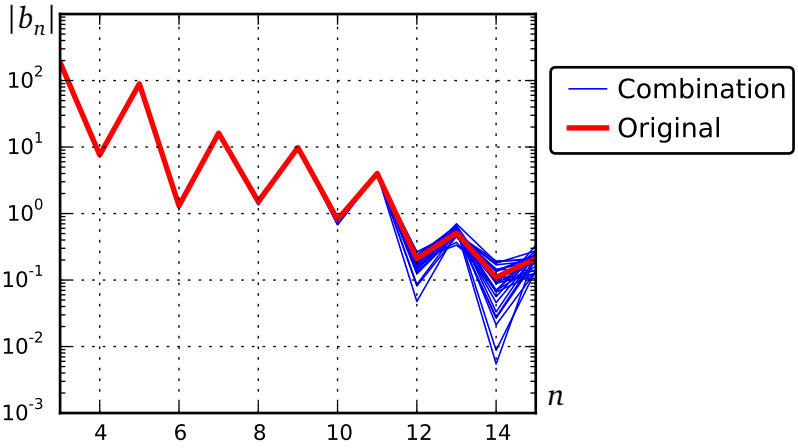

Figure 51: The computation of 30 sets of reconstructed multipoles in blue and the original multipoles in red/thick.

The assumed levels for the error sources are low such that a precise measurement system is presumed. $\sigma_\mathrm{m} = 0.1$ is set for the measurement noise and $\sigma_\mathrm{p} = 0.01$ mm defines the position uncertainty.

Results

The reconstruction yields accurate and precise results. The use of the even multipoles only, does not have any problematic effect on the method. Fig. (50) shows the error distribution as a heat map. The relative error of the field reconstruction shows the same behavior as for the former setups: Inside the reference radius, the reconstruction is good ($B_\mathrm{err} \leq 10^{-4}$), outside it grows with radial distance.

The comparison of the multipoles is shown in Fig. (51). The multipoles are reconstructed with a high precision. Although the odd multipoles are not directly measured, the combination of measurements yields precise results for these multipoles. An uncertainty is visible for the multipole orders larger than 11. There, the relative difference is larger, as the multipole values are small (< 1).

This setup is useful and could find application in magnets with a small aperture. The absence of a central coil allows a compact design so that a very small coil could be manufactured for that purpose.

6.3.2 Exclusive use of the quadrupole component

In this paragraph, the highest multipole that is used from the measurement, is set to $N = 2$. That means that only the quadrupole component is acquired at the measurement positions. Using the coil presented in this section, the highest possible opening angle should be set. Fig. (6) showed the dependence of the opening angle on the sensitivity factor in a tangential coil. For a much larger angle of $\delta = 90°$, Fig. (52) shows the factor for the first ten multipoles. The factor of the quadrupole coefficient K_2 has the highest factor of 1.0 such that this multipole is measured very precisely. Some other multipoles, however, are measured with a much lower sensitivity. The sensitivity factor K_4, for example, is zero. Thus, the blind eye of such a coil is of low order. These low sensitivities do not matter, if the quadrupole component is measured exclusively. There, the sensitivity is highest and the acquired information most precise.

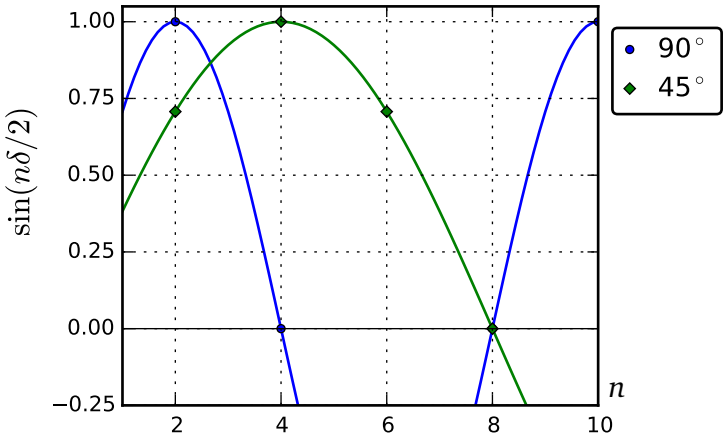

Figure 52: The term $\sin(n\delta/2)$ that defines the sensitivity of the tangential coil over the multipole order n for large opening angles δ.

Acquiring one information per measurement position only, requires a high number for the positions I. In the following computations, a configuration with $I = 48$ measurement position is used. The number of known quantities is therefore $I \times N/2 = 48$, same as in the example in the previous paragraph.

The simulated multipoles are also the same and can be found in the Figures (46) and (47). The error sources are again $\sigma_m = 0.1$ and $\sigma_p = 0.01$ mm.

Results

The results of the combination of measurements in that configuration, are similar to the previous results. Fig. (53) shows the relative error distribution with the known behavior: Inside the reference radius, the error is small, outside it grows with radial distance.

The comparison of the multipoles in logarithmic scale, shows again a difference for the multipoles with a small value. From order 12 on, the multipoles are smaller than 1.0 and the different results of the reconstruction are visible. As the logarithmic scale makes the errors on the lower orders difficult to see, the sample standard deviation is computed for the multipoles in the Fig. (55).

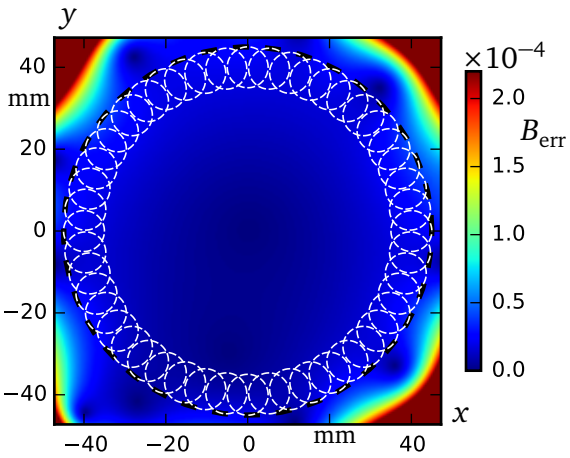

Figure 53: Computation of the relative error $B_{\text{err}} = |B_{\text{rec}} - B_{\text{o}}|/|B_{\text{o}}(0)|$ of the original field B_{o} and the reconstructed field B_{rec} with $\sigma_{\text{m}} = 0.1$ and $\sigma_{\text{p}} = 0.01$ mm.

The presented method yields good results for the tested configuration. A coil with very specific sensitivity factors is therefore useful. Such a coil is not applicable for a single measurements, as the sensitivity is too low for the multipole of order $n = 4$. With the combination of many measurements however, the entire set of multipoles can be computed to an adequate accuracy.

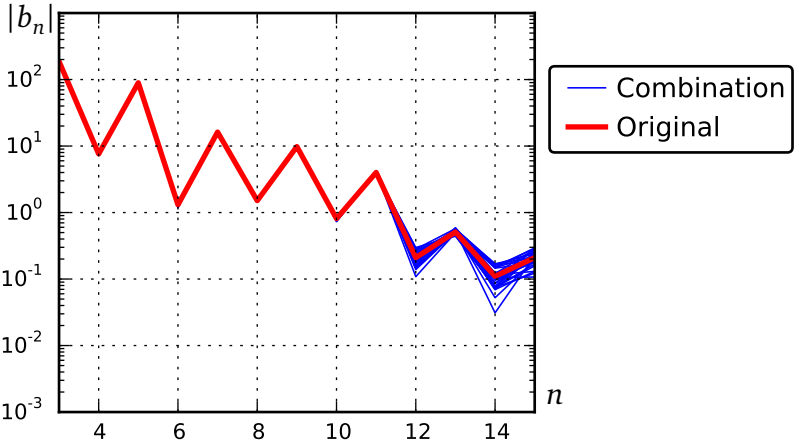

Figure 54: The computation of 30 sets of reconstructed multipoles in blue and the original multipoles in red/thick.

6.3.3 Conclusion

Using only even multipoles with a special coil, gives good results. The reconstruction computes the results with a high accuracy, as seen in the Figures (50) and (53). The precision of the results is shown in Fig. (55) as the sample standard deviation. It is computed for each multipole after 250 runs.

The upper, blue curve is computed for the setup with 16 measurement positions and three acquired multipoles. The imposed noise level of $\sigma_m = 0.1$ causes a level of about 0.07 on the computed multipoles. That is a small improvement of the precision compared to a single measurement. Moreover is the effect of the blind eye not present on the higher-order multipoles.

The green curve is computed for the 48 measurements of the quadrupole component. It shows a very similar curve with an almost equal slope. The values are, from the sextupole component on, about 0.3 smaller than for the other configuration. The quadrupole component of the results is for both configurations reconstructed with a lower precision.

The condition number is for both matrices $\kappa = 3.5$. As seen in Fig. (56), this good value for the condition number comes from the small ratio $r_c/r_0 = 5/45 = 1/9 \approx 0.11$. With a small number for N, a good condition number needs many measurement positions I, as it is the case for both configurations.

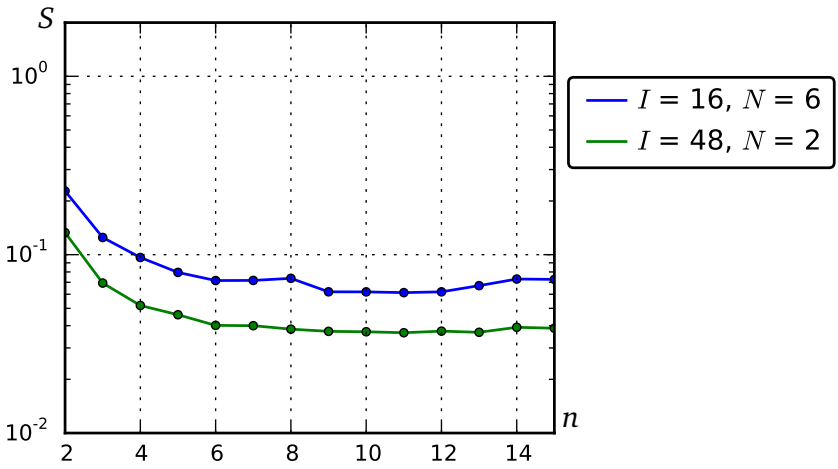

Figure 55: The sample standard deviation S in logarithmic scale for 250 computations with random noise for both configurations.

An increase of the coil radius needs more acquired multipoles, which is limited for the considered configurations.

The setup of a coil that acquires only the quadrupole component, yields adequate results. A small and compact structure with an opening angle of $\delta = 90°$, has to sample the domain by many measurements. With an automatized system, this can be done time-efficient and with low costs so that this coil scheme is practicable.

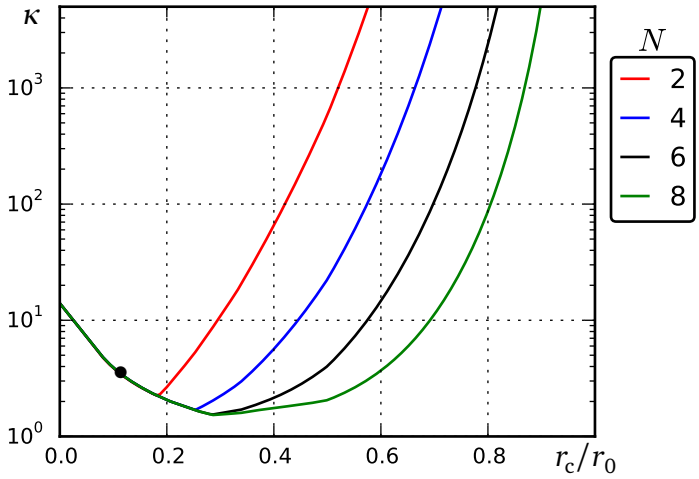

Figure 56: The condition number κ for a matrix with even multipoles n over the ratio of the coil radius to the reference radius r_c/r_0. The number of measurement positions is set to $I = 16$, the number of used multipoles $N \in 2,4,6,8$. The bullet indicates the condition number for the used configurations.

7 Summary and Outlook

The limitations of a basic rotating-coil measurement were a problem in the domain of magnetic field measurements for accelerator magnets. The powerful and most widely used measurement device was limited to magnets with an aperture that suited the radial dimensions of the shaft with its coils. This drawback makes measurement laboratories manufacture a larger set of different rotating coils, measure on a small reference radius or change for a different measurement technology with less precision. On the other hand, the rotating coil is the most precise tool to measure both weak as well as strong fields, as a result making it the preferred choice of measurement engineers.

These points raised the idea of putting together several measurements in different position. In doing so, it combined high precision with the flexibility to measure magnets with larger aperture than the coil radius. The irregularly distributed measurement error on the acquired multipoles ruled out approaches that relied on the magnetic field itself. That is because of the bad precision on the main field component as well as on the multipoles of order $n > 9$.

A combination that relies only on the precisely measured multipoles however, is the technique that gives a measurement laboratory a new versatility. Such a method is presented in this work with proven quality. After having analyzed the different sources of error and their appearance in the multipoles, the computations were then adapted to the precision of the measurement data.

Making use of the high precision of the lower-order multipoles, a reconstruction of the entire set of multipoles could be done with high precision. In comparison, the reconstructed higher-order multipoles have a better precision than the ones from a single measurement. By using a tangential coil with a blind eye, the higher-order multipoles are partially not acquired, so that the improvement in this case is remarkable.

The errors on the multipoles scale as the multipoles with the order. Using field information outside the reference radius of the reconstruction, as in the case of the rectangular dipole in Paragraph (4.1), increases the precision on the higher-order multipoles by a large factor. Acquiring data inside the reference radius, however, shows a smaller improvement of the precision. This is explained by the large influence the higher-order multipoles have outside the reference radius as they strongly affect the field description. Therefore, the least square solution yields a precise value for these multipoles.

The gain in precision is less distinct in cases of multipoles expressed on a large reference radius. The examples of the quadrupole measurement in Paragraph (4.2) and the special coil design in Chapter (6) demonstrate this. Scaling

the reconstructed multipoles to a radius that equals the coil size, makes the relative error on the multipoles much smaller. Therefore, a combination is much more precise than a single measurement with the same coil. However, a larger coil that covers the entire aperture can compete with the precision on multipoles elsewhere the blind eye.

In addition to the simulations, the method was also tested in the measurement laboratory. A dipole with a large, round aperture was measured with two coils of different diameters. The smaller coil acquired the multipoles only inside the domain that was covered by the other coil. The results were compared with a good agreement and improvement of the precision. Practical problems came up and were studied during the measurement process.

The method was applied to different configurations and showed a high functionality for all of them. In addition to obtaining the correct results for perfect input data, the error-propagation throughout the computations remains low resulting in improved precision. This was an especially important outcome for the higher-order multipoles. Furthermore is the versatility of a rotating coil increased by the ability to combine measurements. The presented method with an automatized system with precise positioning stages is a large benefit to every measurement laboratory.

Outlook

The magnetic measurement section at CERN has begun designing a measurement bench with a precise positioning system. The system will move the rotating coil to its predefined positions, automatized and with low effort for the measurement engineer. One or two coils will be designed, whereas the presented coil of Chapter (6) will be one of the choices.

The opening angle will probably be smaller ($\approx 45°$) than the presented design with an angle of 90° in Paragraph (6.3.2). The sensitivity is still larger than 70 % of the maximal sensitivity for the multipole orders 2, 4, and 6, as seen in Fig. (52). Acquiring three multipoles relaxes the restrictions on the reference radius by yielding a well-conditioned matrix for a wider range of the ratio between the coil radius and the reference radius, see Fig. (56).

The method can be further improved by adapting the sensitivity factors of the coil to a greater extent. This could be done by a weighted least square method [75] with the weights proportional to the sensitivity factors.

One also could weight the lower-order multipoles of a central measurement stronger and compute only the higher-order multipoles by displaced measurements. This results in a more complicated matrix, but leads to the correct

results. In particular for quadrupoles and sextupoles, where the main field component is of higher order, this configuration could be more robust.

The computation of the magnetic multipoles by inversion of a matrix can be adapted to other measurement devices. Data acquisition with the stretched wire system with subsequent matrix computation is part of actual research [63] and can make use of the analysis of this work.

References

[1] ATLAS Collaboration, *Observation of a new particle in the search for the standard model Higgs boson with the ATLAS detector at the LHC*, Elsevier Physics Letters B, Vol. 716, 17.09.2012, DOI: 10.1016/j.physletb.2012.08.020.

[2] CMS Collaboration, *Observation of a new boson at a mass of 125 GeV with the CMS experiment at the LHC*, Elsevier Physics Letters B, Vol. 716, 17.09.2012, DOI: 10.1016/j.physletb.2012.08.021.

[3] P. Higgs, *Broken symmetries and the masses of gauge bosons*, Phys. Rev. Lett. 13, 1964, DOI: 10.1103/PhysRevLett.13.508.

[4] O. Brüning, *LHC design report*, physics.acc-ph, arXiv:1206.2913, 07.09.2012.

[5] H. Owen, *Current and future accelerator technologies for charged particle therapy*, Elsevier NIMAE, Vol. 809, 11.02.2016, pages 96-104, DOI: 10.1016/j.nima.2015.08.038.

[6] O. Barbalat, *Applications of particle accelerators*, Proc. CERN Accelerator School, Jyväskylä, Finland, 7-18.09.1992, pages 841-852.

[7] A. Zlobin, *Status of 11 T 2-in-1 Nb_3Sn dipole development for LHC*, Proc. IPAC International particle accelerator conference, Dresden, Germany, 2014.

[8] K. Wille, *The physics of particle accelerators: an introduction*, Oxford University Press, Oxford, Great Britain, 2001, pages 44-57.

[9] J. Rossbach, P. Schmüser, *Basic course on accelerator optics*, Proc. CERN Accelerator School, Jyväskylä, Finland, 7-18.09.1992, pages 17-34.

[10] S. Jezequel, *Prospects for the high-luminosity LHC*, Elsevier Nuclear Physics B, Vol. 245, 12.2013, pages 145-148, DOI: 10.1016/j.nuclphysbps.2013.10.027.

[11] C. Wyss, *The LHC magnet program: from accelerator physics requirements to production in industry*, EPAC European particle accelerator conference, Vienna, Austria, 26-30.06.2000.

[12] S. Russenschuck, *Field computation for accelerator magnets*, Wiley-vch, Weinheim, Germany, 2010.

[13] K. Henrichsen, *Field measurement methods*, Proc. CERN Accelerator School, Anacapri, Italy, 11-17.04.1997, pages 127-135.

[14] S. Sanfilippo, *Hall probes: physics and application to magnetometry*, Proc. CERN Accelerator School, Bruges, Belgium, 16-25.06.2009, pages 423-463.

[15] L. Bottura, *Field measurements*, Proc. CERN Accelerator School, Erice, Italy, 8-17.03.2002, pages 118-148.

[16] L. Walckiers, *Harmonic coil measurement method*, Proc. CERN Accelerator School, Bruges, Belgium, 16-25.06.2009, pages 357-286.

[17] L. Walckiers, *Magnetic measurement with coils and wires*, physics.acc-ph, arXiv:1104.3784v1, 30.03.2011.

[18] D. Jackson, *Classical electrodynamics*, 3rd edition, Wiley, New York, USA, 1999, pages 174-178.

[19] E. Wilson, *Transverse motion*, Proc. CERN Accelerator School, Brunnen, Switzerland, 02-09.07.2003, pages 17-41.

[20] L. Bottura, *Field measurement methods*, CERN Accelerator School, Bruges, Belgium, 16-25.06.2009, `https://cas.web.cern.ch/cas/Belgium-2009/Lectures/PDFs/Bottura-1.pdf`.

[21] E. Wilson, *An introduction to particle accelerators*, Oxford University Press, Oxford, Great Britain, 2001, pages 94-102, DOI: 10.1093/acprof:oso/9780198508298.003.0007.

[22] A. Jain, *Measurements of field quality using harmonic coils*, US particle accelerator school, Houston, USA, 22-26.01.2001, `http://www.bnl.gov/magnets/Staff/Gupta/scmag-course/HarmonicCoil_Slides.pdf`.

[23] A. K. Jain, *Basic theory of magnets*, Proc. CERN Accelerator School, Anacapri, Italy, 11-17.04.1997, pages 1-21.

[24] M. Buzio, *Fabrication and calibration of search coils*, Proc. CERN Accelerator School, Bruges, Belgium, 16-25.06.2009, pages 387-422.

[25] L. Michelotti, *Combining multipole data*, US particle accelerator conference, Washington DC, USA, 16.03.1987, `http://accelconf.web.cern.ch/accelconf/p87/PDF/PAC1987_1645.PDF`.

[26] P. Spiller, *A new high-intensity synchrotron SIS100 with strong bunch compression for GSI*, Proc. US particle accelerator conference, Chicago, US, 2001, http://lss.fnal.gov/archive/proceedings/PAPERS/RPPH024.PDF.

[27] P. Moon, *Field theory handbook*, 2nd edition, Springer, Berlin, Heidelberg, 1988.

[28] F. Peña, G. Franchetti, *Elliptic and circular representation of the magnetic field in SIS 100*, Technical Report ACC-note-2008-0001, GSI Helmholtzzentrum für Schwerionenforschung, 2008.

[29] P. Schnizer, *Theory and application of plane elliptic multipoles for static magnetic fields*, Elsevier NIMA, Vol. 607, pages 505-516, 21.08.2009, DOI: 10.1016/j.nima.2009.06.007.

[30] S. Russenschuck, O. Boine-Frankenheim, *Establishing C3, the coherence between accelerator physics requirements, magnet manufacture, and magnetic measurements*, IMEKO International measurement conference, Benevento, Italy, 15-17.09.2014.

[31] W. G. Davies, *The theory of the measurement of magnetic multipole fields with rotating coil magnetometers*, Elsevier NIMA, Vol. 311, pages 399-436, 15.01.1992.

[32] L. Fiscarelli, *The new digital integrator*, IMMW17 International magnetic measurement workshop, Barcelona, Spain, 18-23.09.2011, http://immw17.cells.es/presentations/Tue02-IMMW17-LFiscarelli.pdf.

[33] F. Zimmermann, *LHC: The machine*, SLAC summer institute, Menlo Park, USA, 23.07-3.08.2012, https://www-conf.slac.stanford.edu/ssi/2012/Presentations/Zimmermann.pdf.

[34] W. Oelert, *The Elena project at CERN*, physics.acc-ph, arXiv:1501.05728, 23.01.2015.

[35] V. Ziemann, *Sorting the LHC dipoles using simulated annealing*, EPAC European particle accelerator conference, 27.06-01.07.1994, http://cern.ch/AccelConf/e94/PDF/EPAC1994_1054.PDF.

[36] P. Schmüser, *Magnet measurements of superconducting magnets and analysis of systematic errors*, Proc. CERN Accelerator School, Montreux, Switzerland, 16-20.03.1992, pages 240-267.

[37] A. Temnykh, *Vibrating wire field-measuring technique*, Proc. particle accelerator conference, Vancouver, Canada, 12-16.05.1997, http://accelconf.web.cern.ch/accelconf/pac97/papers/pdf/4C010.PDF.

[38] A. Jain, *Overview of magnetic measurement techniques*, US particle accelerator school, Santa Barbara, USA, 23-27.06.2003, https://www.bnl.gov/magnets/Staff/Gupta/scmag-course/uspas03/AJ03/AJ_FieldMeasurementOverview.pdf.

[39] G. Karpov, *Precise NMR measurement and stabilization system of magnetic field of superconducting 7 T wave length shifter*, Elsevier NIMA, Vol. 467-468, 21.07.2001, pages 198-201.

[40] W. Scandale, *Geometry and alignment requirements for the LHC main dipole*, EPAC European particle accelerator conference, Vienna, Austria, 26-30.06.2000.

[41] B. Holzer, *Lattice design in high-energy particle accelerators*, Proc. CERN Accelerator School, Trondheim, Norway, 18-29.08.2013, pages 61-101.

[42] B. Holzer, *Introduction to transverse beam dynamics*, Proc. CERN Accelerator School, Erice, Italy, 24.04-04.05.2013, pages 21-41.

[43] Y. Papaphilippou, *Principles of charged particle beam optics*, US particle accelerator school, Ithaca, USA, 20.06-01.07.2005, https://yannis.web.cern.ch/yannis/teaching/principles.pdf.

[44] SixTrack - 6D Tracking Code, sixtrack.web.cern.ch, CERN.

[45] Mad - Methodical accelerator design, mad.web.cern.ch, CERN.

[46] B. Auchmann, *A note on Faraday paradoxes*, IEEE Transactions on magnetics, Vol. 50-2, 02.2014, pages 1025-1028, DOI: 10.1109/TMAG.2013.2285402.

[47] R. Feynman, *The Feynman lectures on physics*, Vol. 2, chap 14, Addison Wesley, Boston, USA, 1964.

[48] L. Fiscarelli, *Improvements on rotating coil systems at CERN*, IMEKO International measurement conference, Benevento, Italy, 15-17.09.2014.

[49] J. Billan, *Twin rotating coils for cold magnetic measurements of 15 m long LHC dipoles*, International conference on magnetic technology, Ponte Vedra Beach, USA, 26.09-2.10.2000, http://cds.cern.ch/record/411162/files/lhc-project-report-361.pdf.

[50] O. Dunkel, *A rotating coil array in mono-bloc printed circuit technology for small scale harmonic measurements*, IMMW17 International magnetic measurement workshop, Barcelona, Spain, 18-23.09.2011, http://immw17.cells.es/presentations/Tue01-IMMW17-ODunkel.pdf.

[51] J. DiMarco, *Application of pcb and fdm technologies to magnetic measurement probe system development*, Batavia, USA, 01.10.2012, http://lss.fnal.gov/archive/2012/conf/fermilab-conf-12-570-td.pdf.

[52] J. Tanabe, *Iron dominated electromagnets: design, fabrication, assembly and measurements*, World Scientific, Singapore, 03.2005, page 217.

[53] A. Rijllart, *Magnetic measurement systems for the LHC dipole assembly companies*, EPAC European particle accelerator conference, Lucerne, Switzerland, 5-9.07.2004, http://accelconf.web.cern.ch/accelconf/e04/PAPERS/WEPKF019.PDF.

[54] J. DiMarco, *Influence of mechanical vibrations on the field quality measurements of LHC interaction region quadrupole magnets*, IEEE Trans. on Appl. Supercond. 10, 1458, 2000, DOI: 10.1109/77.828515.

[55] R. Beth, *Complex representation and computation of two-dimensional magnetic fields*, Journal of applied physics 37, 2568, Brookhaven, USA, 20.01.1966, DOI: 10.1063/1.1782086.

[56] R. Beth, *An integral formula for two-dimensional fields*, Journal of applied physics 38, 4689, Brookhaven, USA, 10.07.1967, DOI: 10.1063/1.1709204.

[57] D. Einfeld, *Effect of magnetic multipoles on the ALBA dynamics*, EPAC European particle accelerator conference, Genoa, Italy, 23-27.06.2008, http://accelconf.web.cern.ch/AccelConf/e08/papers/thpc068.pdf.

[58] K. Jänich, *Funktionentheorie: Eine Einführung*, Springer, Berlin, Heidelberg, 2011, pages 94-100.

[59] A. Verdier, *Feed-down effect in dipole alignment*, Proc. IEEE particle accelerator conference, Chicago, USA, 18-22.06.2001, pages 1693-1695.

[60] A. Bogacz, *Magnetic multipoles, magnet design*, US particle accelerator school, Fort Collins, USA, 10-21.06.2013, http://casa.jlab.org/publications/viewgraphs/USPAS2013/L_5_MagneticMultipoles_Rev2.pdf.

[61] J. Marcos, *Determination of magnetic multipoles using a hall probe*, Proc. IPAC International particle accelerator conference, Dresden, Germany, 15-20.06.2014.

[62] G. Le Bec, *Stretched wire measurement of multipole magnets at the ESRF*, IMMW17 International magnetic measurement workshop, Barcelona, Spain, 18-23.09.2011, http://immw17.cells.es/presentations/Thu01-IMMW17-LeBec.pdf.

[63] G. Le Bec, *Stretched wire measurement of multipole accelerator magnets*, American physical society, Phys. Rev. ST Accel. Beams 15, 022401, 08.02.2012, DOI: 10.1103/PhysRevSTAB.15.022401.

[64] P. Schnizer, *Measured and calculated field properties of the SIS 100 magnets described using elliptical and toroidal multipoles*, PAC Particle accelerator conference, Vancouver, Canada, 04-08.05.2009.

[65] O. Köster, L. Fiscarelli, S. Russenschuck, *A procedure for combining rotating-coil measurements of large-aperture accelerator magnets*, Elsevier NIMA, Vol. 818, 11.05.2016, pages 20-25, DOI: 10.1016/j.nima.2016.02.019.

[66] LAPACK, *Linear Algebra PACKage*, http://www.netlib.org/lapack/, V. 3.5.

[67] SciPy, *Package for scientific computing with Python*, scipy.org, V. 0.14.

[68] NumPy, *Package for scientific computing with Python*, numpy.org, V. 1.8.2.

[69] W. Gander, *Scientific computing, an introduction using Maple and MATLAB*, Springer, Berlin, Heidelberg, 2014, pages 29-31.

[70] M. Buzio, *Manufacturing and calibration of search coils*, CERN Accelerator School, Bruges, Belgium, 16-25.06.2009, http://cern.ch/cas/Belgium-2009/Lectures/PDFs/Buzio-1.pdf.

[71] Vector Fields, Opera 3d-Tosca. http://operafea.com.

[72] A. Fabich, *MedAustron - the Austrian ion therapy and research center*, CERN Accelerator School, Senec, Slovakia, 01.06.2012, http://cas.web.cern.ch/cas/Slovakia-2012/Lectures/Fabich.pdf.

[73] ROXIE, http://www.cern.ch/roxie/, V. 10.1.

[74] J. DiMarco, *An encapsulated rotating-coil test system at Fermilab*, IMMW17 International magnetic measurement workshop, Barcelona, Spain, 18-23.09.2011, http://immw17.cells.es/presentations/Tue04-IMMW17-JDiMarco.pdf.

[75] L. Wasserman, *All of nonparametric statistics*, Springer, Berlin, Heidelberg, 2006, pages 61-81.

[76] Wolfgang-Gentner-Stipendien, Bundesministerium für Bildung und Forschung, http://wolfgang-gentner-stipendien.web.cern.ch.

List of Symbols

A_n	Skew component of the complex multipole	
a_n	Normalized skew component of the complex multipole	
B_n	Normal component of the complex multipole	
b_n	Normalized normal component of the complex multipole	
$\vec{B}$	Magnetic flux density	
B_c	Complex magnetic flux density	
B_x	x-component of the magnetic flux density	
B_y	y-component of the magnetic flux density	
B_r	Radial component of the magnetic flux density	
B_φ	Axial component of the magnetic flux density	
B_o	Simulated field	
B_rec	Recovered field of the combination	
C'_n	Measured multipoles on the small shaft	
C_k	Reconstructed multipoles	
c_n	Normalized multipoles	
$c_n^{(\ell)}$	Normalized multipoles of low values	
$c_n^{(h)}$	Normalized multipoles of high values (in the fringe field)	
$\vec{E}$	Electric field	
F_L	Lorentz force	
I	Number of measurement positions	
i	Enumerator for the measurement position	$i \in [1,I]$
K	Number of reconstructed multipoles on the ref. radius r_0	
k	Multipole order of field reconstruction on the ref. radius	$k \in [2,K]$
K_n	Sensitivity factor	
K_n^tan	Sensitivity factor of the tangential coil	
K_n^rad	Sensitivity factor of the radial coil	
L	Coil length	
ℓ_m	Magnetic length	
$[M]$	Matrix that connects the multipoles	
N_t	Number of turns	
N	Highest multipole order acquired by the small coil	
n	Multipole order of measurement with small coil	$n \in [2,N]$
$\vec{n}$	Surface normal	
q	Electrical charge	

r_0	Reference radius	
r_c	Measurement radius of the small coil	
r_i	Inner radius of the radial coil	
r_D	Radius of the dipole coil	
S	Sample standard deviation	
s	Coordinate that follows the ideal particle trajectory	
t	Time	
U_i	Induced voltage	
$\vec{v}$	Velocity	
$[W_i]$	Inner trapezoidal matrix of $[M]$	
$w_{n,k}^{(i)}$	Entries of the matrix $[W_i]$	
$w_{n,k}^{(\mathrm{err})}$	Entries of the error matrix due to positioning errors	
z	Complex coordinate	$x + \mathrm{i}\,y$
z_0	Origin of the reference system in the complex plane	
z_i	Positions of the measurements in the complex plane	
Δz	Complex error in the position	
α	Starting angle of the angular encoder of the rotating coil	
γ	Path of the error sum ξ	
γ_i	Position on path γ	
δ	Opening angle of the tangential coil	
η	Angle of two subsequent measurement positions	
θ, $\tilde{\theta}$	Angles to define coil position	
κ	Condition number of the matrix $[M]$	
λ	Ratio of position error to coil radius	$\Delta z / r_\mathrm{c}$
$\lambda^{(\ell)}$	Low precision of the position	
$\lambda^{(h)}$	High precision of the position	
ξ	Error sum of the field derivation	
$\sum$	Sum of the differences of the magn. field depending on the angle α	
σ_p	Standard deviation of the position uncertainty	
σ_m	Standard deviation of the measurement uncertainty	
τ	Angle of the complex multipole	
Φ_m	Magnetic flux	

List of Abbreviations

CERN	Conseil Europeen pour la Recherche Nucleaire
ELENA	Extra Low Energy Antiproton
FAIR	Facility for Antiproton and Ion Research
GSI	Gesellschaft für Schwerionenforschung
LHC	Large Hardron Collider
NMR	Nuclear Magnetic Resonance
PCB	Printed Circuit Board

List of Figures

List of Tables

Danksagung

Für die Unterstützung während meiner Promotion und beim Schreiben dieser Arbeit bedanke ich mich bei folgenden Menschen und Institutionen:

- Dr. Stephan Russenschuck für seine Betreuung in den letzten vier Jahren, die mir erlaubt hat ein tiefgreifendes Wissen über Magnete, Magnetfeldmessung und numerische Berechnung zu erlangen
- Prof. Oliver Boine-Frankenheim für die Annahme und Betreuung als Doktorand, die Unterstützung bei meinen Aufenthalten am TEMF und das Vertrauen in eine selbstständige Arbeitsweise
- Prof. Henke, Dr. Filtz und Dr. Bruns für deren Unterricht in theoretischer Elektrotechnik und im Finden von analytischen sowie numerischen Lösungen
- Prof. Schuhmann für seine richtungsweisende Anmerkung: "Sie wollen 15 Werte berechnen und haben ca. 60 Informationen. Das muss doch einfacher gehen!"
- Dr. Lucio Fiscarelli für seine geduldigen Erklärungen und die gute Zusammenarbeit
- Kollegen und Freunden am CERN und am TEMF
- Dem Gentner-Program [76], das meine Arbeit am CERN und die vielen Reisen zum TEMF finanziert hat
- Robert Huth für seine Vorbildsfunktion an Einsatz und Entschlossenheit
- Familie und Freunden

Wissenschaflicher Werdegang

2005	Abitur am Albert-Einstein-Gymnasium, Berlin
2005 - 2012	Studium der Elektrotechnik, Technischen Universität Berlin Schwerpunkte: Theoretische Elektrotechnik, Robotics, Elektromagnetische Verträglichkeit
2012	Teilnahme JUAS, Teilchenbeschleunigerschule in Genf
2012	Technischer Student am CERN für 7 Monate
2012	Diplomarbeit "Potentialtheoretische Aspekte der Magnetfeldmessung"
2013	Erhalt Gentner-Stipendium
2013 - 2016	Doktorand an der Technischen Universität Darmstadt
2013 -	Arbeit am CERN in der Gruppe für Magnetfeldmessung

Veröffentlichungen

2016 O. Köster, L. Fiscarelli, S. Russenschuck,
A procedure for combining rotating-coil measurements of large-aperture accelerator magnets, Elsevier Nuclear Instruments and Methods in Physics Research A

2016 P. Arpaia, M. Buzio, O. Köster, S. Russenschuck, G. Severino,
Rotating-coil calibration in a reference quadrupole, considering roll-angle misalignment and higher-order harmonics, Elsevier Measurements

2014 P. Arpaia, M. Buzio, O. Köster, S. Russenschuck, G. Severino,
Calibrating the sensing-coil radius by feed-down from a harmonic reference, IMEKO, Italy.

Vorträge

2015 ICAP, Shanghai, China
A "multipole factory" for measuring magnetic fields in large-aperture accelerator magnets

2015 KWT
Analytically combining rotating-coil measurements of large-aperture accelerator magnets